Contribution à la classification automatique de tissus corporels par intégration des connaissances médicales qualitatives

Han Kang

LAMIH
LABORATOIRE
D'AUTOMATIQUE
DE MECANIQUE ET
D'INFORMATIQUE
INDUSTRIELLES
ET HUMAINES

Université de Valenciennes et du Hainaut-Cambrésis

N° d'ordre : 09/07

Université de Valenciennes

et du Hainaut-Cambrésis

Doctorat d'université

Automatique et Informatique des Systèmes Industriels et Humains

Han KANG

Contribution To Automatic Corporal Tissue Classification By Integrating Qualitative Medical Knowledge: Application To The Analysis Of Musculo Skeletal Diseases And Disabilities From MRI Sequences

Soutenue le 30 janvier 2009

Composition du jury :

Pr. Irina Perfilieva	Rapporteur	Université de Ostrava – Rép. Tchèque
Pr. Michèle Rombaut	Rapporteur	Université de Grenoble
Pr. Yassine Ruichek	Examinateur	Université de Belfort-Montbéliard
Pr. Georges Poumarat	Examinateur	Université de Clermont-Ferrand
Pr. Abdelmalik Taleb-Ahmed	Directeur	Université de Valenciennes
Pr. Xianyi Zeng	Directeur	ENSAIT de Roubaix
Dr. Antonio Pinti	Co-Directeur	Université de Valenciennes

LAMIH
LABORATOIRE
D'AUTOMATIQUE
DE MÉCANIQUE ET
D'INFORMATIQUE
INDUSTRIELLES
ET HUMAINES

**Université de Valenciennes
et du Hainaut-Cambrésis**

N° d'ordre : 09/07

Université de Valenciennes

et du Hainaut-Cambrésis

Doctorat d'université

Automatique et Informatique des Systèmes Industriels et Humains

Han KANG

Contribution To Automatic Corporal Tissue Classification By Integrating Qualitative Medical Knowledge: Application To The Analysis Of Musculo Skeletal Diseases And Disabilities From MRI Sequences

Soutenue le 30 janvier 2009

Composition du jury :

Pr. Irina Perfilieva	Rapporteur	Université de Ostrava – Rép. Tchèque
Pr. Michèle Rombaut	Rapporteur	Université de Grenoble
Pr. Yassine Ruichek	Examinateur	Université de Belfort-Montbéliard
Pr. Georges Poumarat	Examinateur	Université de Clermont-Ferrand
Pr. Abdelmalik Taleb-Ahmed	Directeur	Université de Valenciennes
Pr. Xianyi Zeng	Directeur	ENSAIT de Roubaix
Dr. Antonio Pinti	Co-Directeur	Université de Valenciennes

Acknowledgements

I would like to thank my director Mr. Abdelmalik TALEB-AHMED, Professor of Université de Valenciennes et du Hainaut-Cambrésis, for his proposition of this research subject and his acceptance of my candidature for working on this subject, as well as his excellent guidance.

I am grateful to Mr. Antonio PINTI, Lecturer of Université de Valenciennes et du Hainaut-Cambrésis, who co-directed this work, for his persistent support and his help to establish the necessary relations for this work.

I am also thankful to Mr. Xianyi ZENG, Professor of Ecole Nationale Supérieure des Arts et Industries Textiles, co-director of this work, for his numerous academic advice for this work, and for his sharing with me his knowledge and his method of doing research.

I appreciate Mme. Irina PERFILIEVA, Professor of University of Ostrava, Czech Republic, and Mme. Michèle ROMBAUT, Professor of Université Joseph Fourier, for their acceptance to be the reporter of this work and their effort to review this work. I appreciate at the same time Mr. Yassine RUICHEK, Professor of Université de Technologie de Belfort-Montbéliard, and Mr. Georges POUMARAT, Professor of Université de Clermont-Ferrand, for having accepted to examine this work.

I want to thank for the support and help of all the professors, researchers, and PhD candidates during the preparation of my PhD dissertation in the laboratory LAMIH.

Although I did not mention in the first place, I would like to express the most gratitude to my parents, and grandparents, for their endless support and love.

Notations and Acronyms

u_{ij}	Fuzzy adhesion
v_i	Cluster center
$\lVert * \rVert$	Euclidean distance
U	Clustering matrix
ε	Value for convergence
N_k	Set of neighbors in a window centered on the interesting pixel
N_R	Cardinality
$\Phi(x)$	Nonlinear mapping function
$K(x,y)$	Inner product between $\Phi(x)$ and $\Phi(y)$
CT	Computerized Tomography
EM	Expectation Maximization
FCM	Fuzzy C-Means
FCMS	FCM with spatial constraints
GMM	Gaussian Mixture Model
GMM_S	GMM with spatial constraints
IMFFCM	Improved Multiple Features FCM
KFCM	Kernelized FCM
KFCMS	KFCM with spatial constraints
MFFCM	Multiple Features FCM
MRF	Markov Ramdom Field
MRI	Magnetic Resonance Imaging
NGFCM	Novel Generalized FCM

List of Figures

List of Tables

Table of Contents

Introduction Générale

Dans le diagnostic médical utilisant des images IRM, les techniques de segmentation d'images jouent un rôle important. Il vise à partitionner une image médicale dans un certain nombre de régions qui sont homogènes à l'égard de certaines caractéristiques telles que le niveau de gris et la texture. L'algorithme Fuzzy c-means (FCM) avec terme de pénalité a été largement appliqué dans l'analyse des images IRM. Cependant, il y a certains inconvénients de cette méthode:

- Dérivation complexe de la fonction objective de FCM peut entrainer des résultats inexacts.

- Dans la définition du terme de pénalité de la fonction objective de FCM, la taille de la fenêtre d'observation n'est pas optimisée.

- Le coefficient du terme de pénalité de la fonction objective de la FCM n'est pas déterminé automatiquement pour obtenir le meilleur résultat. Il devrait être optimisé automatiquement afin que les avantages de la FCM et le terme de pénalité peuvent être pris en compte dans la fonction objective.

- Dans la fonction objective de la FCM, chaque pixel est généralement décrit seulement par le niveau de gris et d'autres informations importantes telles que les relations avec les pixels voisins et la texture ne sont pas prises en compte.

Dans le cadre de ma thèse, deux principales contributions ont été proposées en vue d'améliorer la qualité de la segmentation par la méthode FCM.

La première contribution est que nous proposons un algorithme permettant de définir la taille de la fenêtre d'observation de manière dynamique pour extraire l'information spatiale. Et nous utilisons un vecteur de dimension 10 pour décrire chaque pixel. Ce vecteur comprend le niveau de gris et l'information spatiale locale et globale sur les pixels voisins dans la fenêtre d'observation. Cela peut réduire de manière efficace les difficultés liées à la sélection du

coefficient du terme de pénalité et les dérivations complexes

Pourtant, la segmentation avec les niveaux de gris et la texture conduit souvent à des résultats peu satisfaisants, parce que ces caractéristiques générales ne peuvent pas prendre en compte les connaissances spécialisées. Par conséquent, il est nécessaire d'intégrer des connaissances a priori sur l'analyse des images médicales pour obtenir de meilleurs résultats de la classification des tissus.

Pour cette raison, notre seconde contribution est le développement d'un système intelligent pour la classification des tissus. D'abord, un système spécifique de classification des tissus de la cuisse est développé. Dans ce système, la connaissance concernant la structure géométrique des tissus est intégrée afin de contrôler l'application de l'algorithme FCM au cours de la procédure de segmentation pour obtenir la classification des tissus de cuisse. Quatre étapes ont été proposées pour séparer correctement les cinq classes dans l'image de cuisse: fond, l'os spongieux, l'os cortical, tissu adipeux, et muscle.

Toutefois, ce système n'est pas généralisable car il est fortement lié à la connaissance spécifique de cuisse et l'intégration de cette connaissance s'effectue par une procédure manuelle. Pour la segmentation des images d'autres organes, nous devons intégrer de nouvelles connaissances et construire de nouveaux modèles. Ainsi, nous développons un système général pour la classification automatique des tissus corporels. Les caractéristiques communes concernant les positions géométriques des tissus sont extraites afin de construire des règles d'inférence. Ces règles sont ensuite appliquées aux résultats de la méthode FCM afin d'améliorer la qualité de segmentation des images médicales et d'associer chaque classe obtenue à un tissu spécifique. De cette façon, nous avons construit un système généralisé qui ne se limite pas à une application spécifique, mais permet de formaliser toutes formes de la connaissance humaine sur l'observation des images médicales et les intégrer automatiquement dans la procédure d'analyse d'image.

General Introduction

In the diagnosis using MRI images, image segmentation techniques play a key role. It aims at partitioning a medical image into a number of non-overlapped and constituent regions which are homogeneous with respect to some characteristics such as grey level and texture. Fuzzy c-means (FCM) clustering algorithm with penalty term has been widely applied in the analysis of MRI images. However, there are some drawbacks in this method:

- Additional complex derivations are often involved in FCM objective function which leads to inaccurate results.

- In the definition of penalty term of the FCM objective function, the size of the observation window is not optimized.

- The importance coefficient of the penalty term is never systematically defined. It should be optimized so that both the advantages of FCM and the penalty term can be taken into account in the objective function.

- In the objective function of FCM, each pixel is described by the related grey level only and other important information such as relations with neighboring pixels and texture are not taken into account.

In my PhD work, two main contributions have been proposed in order to improve FCM-based image segmentation quality.

The first contribution is that we developed a new algorithm for defining an adaptive size of the observation window. And we generated a multi-dimensional vector to describe each pixel which enables to integrate both local and global spatial information on neighboring pixels in the observation window. So the uncertainty and the complexity of FCM algorithm with penalty term can be reduced.

Nevertheless, in the analysis of medical images, segmentation with context independent features such as grey level and texture often leads to unsatisfactory results because these general features can not take into account the specialized background knowledge, which is important when doctors study them manually using their own vision. Therefore, it is necessary to incorporate our a priori knowledge on medical image analysis for obtaining better results of tissue classification.

Therefore, our second contribution is the development of a intelligent system for tissue classification. First, a specific tissue classification system of thigh has been developed. In this system, a priori knowledge concerning the tissue geometric structure of thigh is used to control the application of the FCM algorithm during the segmentation procedure for tissue classification of thigh. Four steps have been proposed for correctly separating the five classes of the thigh image: background, spongy bone, cortical bone, adipose tissue and muscle.

However, the proposed method depends too much on the specific knowledge of the thigh structure and background knowledge incorporation is a manual procedure. For segmenting images of other organs, we need to incorporate new background knowledge and construct new models. Therefore, it is necessary to develop a more generalized system permitting to formalize all kinds of human knowledge on medical image observation and automatically incorporate them into the image analysis procedure.

Next, we developed a generalized intelligent system for tissue classification. We extracted the common tissue features among different parts of human body and constructed the corresponding models for these features. In this way, we built a more generalized system which is not limited to a specific application but permits to formalize all kinds of human knowledge on medical image observation and automatically incorporate them into the image analysis procedure.

1 State of arts on medical analysis

Magnetic Resonance Imaging (MRI) allows us to explore the living organs in a non-invasive way, and it has advantages over Computerized Tomography (CT) and ultrasound image because it does not involve ionizing radiation ([1]). The analysis of MRI images can be used in the quantification of human body composition ([2]), such as the quantification of muscle/fat ratio ([3]), and the assessment for the variation of body fat content ([2]). All this work has important medical significance in human nutrition and muscle physiology, in the study of pathologic consequences of obesity, and in the study of diseases of muscle ([4]).

In the diagnosis using MRI, image segmentation techniques play a key role ([5]). It aims at partitioning an image into a number of non-overlapped and constituent regions which are homogeneous with respect to some characteristics such as grey level or texture ([6]). There are mainly two categories of image segmentation methods for medical image analysis: contour-based methods and region-based methods. The former contains the active contour models ([7-10]), etc. The later includes Expectation Maximization method ([11,12]) and Fuzzy C-Means method ([13]), etc. Contour-based methods partition an image based on discontinuities among sub-regions, while region-based methods carry out the same work based on the homogeneity of a desired feature within a sub-region, such as grey level, color, and texture.

However, these segmentation methods often lead to unsatisfactory segmentation results. This is because the general features that they used, such as grey level and texture, can not take into consideration the specialized background knowledge, which is crucial when doctors study them manually using their own vision and experience. Therefore, it is necessary to incorporate our a priori knowledge on medical image analysis in order to guide or control the segmentation procedure for obtaining better results of tissue classification. Various tissue classification systems have been developed, such as the system for brain ([14-16]), for bone ([17]) and for chest ([18]).

In this chapter, we will briefly introduce some existing image segmentation methods for medical image analysis as background. Then we will present some existing systems for tissue classification, and shows their limits in order to justify our system for tissue classification.

1.1 Medical image segmentation methods

1.1.1 Active contour

Active contours are connectivity-preserving relaxation ([19-21]) methods, applicable to the image segmentation problems. Active contours have been used for image segmentation and boundary tracking since the first model proposed by Kass et al. ([22]). The basic idea is to start with initial contours and iteratively modify them by shrink/expansion operations according to the constraints of image. There are two categories of active contour models: parametric models ([23]) and geometrical models ([24]).

In the field of medical image analysis, active contour has already been applied for the boundary detection of left ventricle ([25, 26]), the vessel ([27]), the tumor of brain ([28]), the anatomical structures of normal brain ([29]), such as corpus callosum, caudate nucleus and hippocampus, etc. Figure 1.1 shows the boundary detection of corpus callosum of a normal brain ([29]).

(a)   (b)

Figure 1.1 Boundary detection of corpus callosum of a normal brain.
(a) original image. (b) the red line is the boundary detection of corpus callosum.

Next, we will introduce the details of active contour models.

1.1.1.1 Parametric active contour model

In the literature, the first work on active contours within the objects segmentation framework was introduced by ([23]). This model locates the image intensity variation by deforming of a closed planar curve towards an object boundary. The evolution of the parametric planar curve $C(s)$, in which s is an arc-length parameter with $s \in [0,1]$, is obtained by minimizing an energy function defined in the observed the image I. This energy is defined as follows:

$$E(C) = E_{int} + E_{ext} \tag{1.1}$$

with

$$E_{int} = \alpha \int |C'(s)|^2 \, ds + \beta \int |C''(s)|^2 \, ds \tag{1.2}$$

$$E_{ext} = \lambda \int g_I \left(\nabla |I(C(s))| \right) |C'(s)| ds \tag{1.3}$$

The two terms of the Eq.(1.2) describe the physical constraints on the geometry of the parametric planar curve. Indeed, the first term makes the active contour behave as a membrane and the second term as a thin section. These two terms forms the expression of the internal energy. Two internal parameters α and β control the tension of the contour and the rigidity of the contour respectively. The term of the Eq.(1.3), namely external energy, conducts the curve towards the borders of the objects by means of a edge–map contour function, defined by:

$$g_I \left(|\nabla I(s)| \right) = \frac{1}{1 + |\nabla G_{\sigma_g} * I(C(s))|^p}, p = 1 \, or \, 2 \tag{1.4}$$

where

G_{σ_g} is the Gaussian kernel with variance σ_g^2 controlling the stretch of the edge boundary.

As this method only considers the local information along the contour, it can give good results only if the initial contour is close enough to the real edge. However, estimating a suitable position for the initial contour without a priori knowledge is difficult. Moreover, it can not detect several

boundaries simultaneously because the entire contour keeps the same topology during the evolution and then it can not be split into multiple boundaries or be merged from several initial contours.

By means of the method of the gradient descent, we obtain ([30]):

$$\frac{\partial C(s,t)}{\partial t} = F\vec{N} \tag{1.5}$$

This equation describes the active contour evolution with time and space (Figure 1.2) allowing an implicit formulation within the level-set methods framework (overall curves of the levels).

Initial curve:
$C(x,y,t = t_0)$

Curve evolving at t_1:
$C(x,y,t = t_1)$

Curve evolving at t_1+1:
$C(x,y,t = t_1+1)$
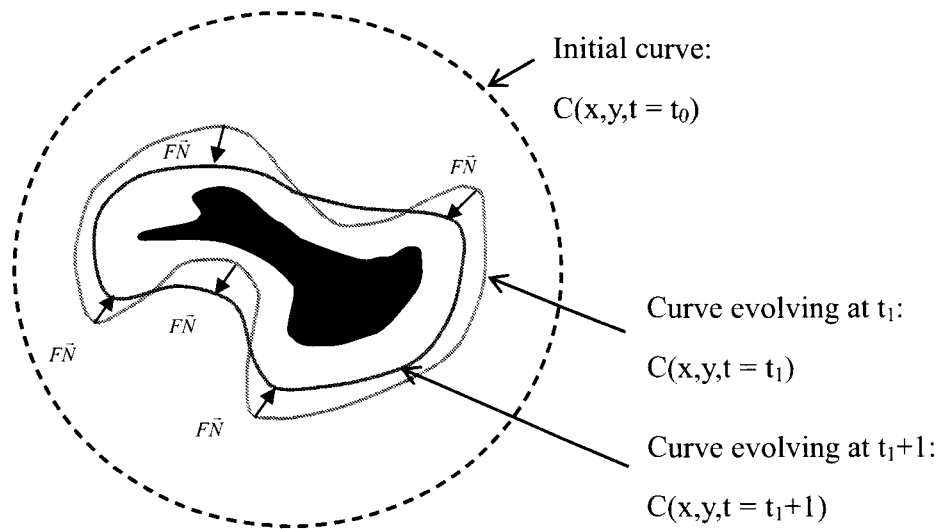
Figure 1.2 Deformation of the curve under the action of a normal force F.

To present the geometrical active contour, we concentrate on curve evolution theory which provides an implicit formulation of the active contour in a level set framework ([31,32]). To introduce the concept of the level set framework we focus on the boundary value problem of a closed contour C deforming with a speed F along its normal direction:

$$\begin{cases} |\nabla T| F = 1 \\ T = 0 \ \textit{on the front} \end{cases} \tag{1.6}$$

Denote $T(C) = \{s = (x,y) \mid C(s,t) = t\}$ as the front position of the curve contour which deforms

to reach the objects boundaries. The propagation of $\gamma(t)$ results from solving the stationary Partial

Differential Equation given by Eq.(1.6). Within the level-set framework, the propagation front is

defined as $\gamma(t) = \{s = (x,y) \mid \phi(C(s,t),t) = 0\}$. It is noted that the new face is related to a noted

function $\phi()$ which will make the front evolve to object boundaries in time. This front evolution

is defined by the following equation:

$$\frac{\partial \phi}{\partial t} + \nabla \phi \cdot \overline{N} = 0 \qquad (1.7)$$

where $\overline{N} = \frac{\nabla \phi}{|\nabla \phi|}$ is a unit vector toward the normal curve direction (Figure 1.3). Figure 1.4 shows

the representation of curve evolution for ϕ.
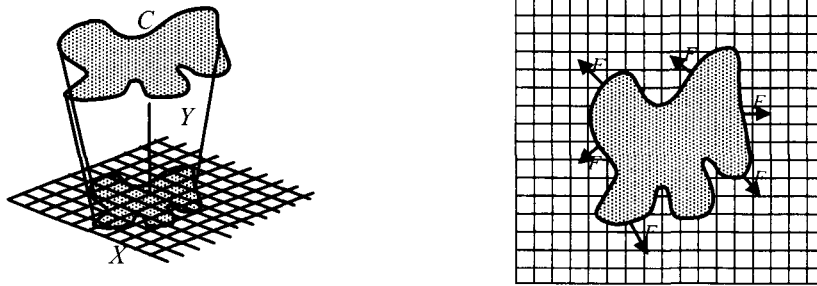
Figure 1.3 Stationary model.
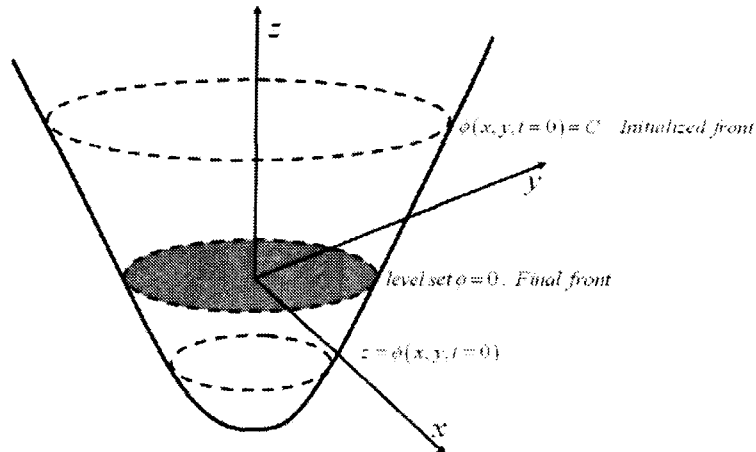
Figure 1.4 Representation of curve evolution for ϕ.

The front $\gamma(t) = \{s = (x,y) \mid \phi(C(s,t),t) = 0\}$ implicitly corresponds to the initial value problem.

In their papers ([31, 32]), Osher *and* Sethian focused on motion under mean curvature flow where

the speed term is expressed by:

$$F = div\left(\frac{\nabla\phi}{|\nabla\phi|}\right) \tag{1.8}$$

To be complete, we should not forget to quote the geometrical active contours introduced by ([33]). The authors proposed the active contour energy formulated as:

$$E(C) = E_{int} + E_{ext} \tag{1.9}$$

with

$$E_{int} = \alpha \int |C'(s)|^2 \, ds \tag{1.10}$$

$$E_{ext} = \lambda \int g_I \left(\nabla |I(C(s))|\right) ds \tag{1.11}$$

Firstly, the term $\beta = 0$ avoids obtaining the high order derivative terms while preserving a smooth aspect of curve shape in the energy function expression.

Secondly, Euclidean metric is integrated for the total energy minimization problem by the following equation:

$$Min \int g_I \left(\nabla |I(C(s))|\right) |C'(s)| \, ds \tag{1.12}$$

This metric takes into account both gradient information and object shape information. It is also an additional constraint within the energy minimization problem to restrict the required solutions by Eq.(1.9).

On the other hand, this model presents some disadvantages, such as

– High sensitivity to different noises.

– The precision and the quality of the objects detection strongly depend on the nature of the $g_I(\cdot)$ function.

1.1.1.2 Geometrical active contour model

It was in the work of Caselles ([24]) that the geometrical active contour model was firstly introduced in level-set frameworks. The following model is proposed:

$$\begin{cases} \frac{\partial \phi}{\partial t} = g_I\left(\left|\nabla I\right|\right) div\left(\frac{\nabla \phi}{|\nabla \phi|}\right)\left|\nabla \phi\right| + v g_I\left(\left|\nabla I\right|\right)\left|\nabla \phi\right| \\ \phi_0 = \phi\left(C\left(s, t = 0\right), t = 0\right) = \pm dist\left(s, C\left(s, t = 0\right)\right) \end{cases}$$
(1.13)

where *dist* is the signed distance to initialized contour ϕ_0.

The constant v is added to increase the evolution speed in order to attract the curve toward the object boundary.

The term $g_I\left(\left|\nabla I\right|\right)$ is identical to that defined in Eq.(1.4). The term $g_I\left(\left|\nabla I\right|\right)$ provides also a criterion of stopping for the speed function given by Eq.(1.8).

In real cases, $g_I\left(\left|\nabla I\right|\right)$ is close to zero in the zones where the gradient of the image is raised, and is close to 1 in homogeneous areas.

In ideal cases, $g_I\left(\left|\nabla I\right|\right)$ is between 0 and 1. It is equal to 0 on the objects boundaries and 1 in a homogeneous area (in or apart from an object).

Taking again the Eq.(1.13), we can write:

$$\frac{\partial \phi}{\partial t} = g_I\left(\left|\nabla I\right|\right) div\left(\frac{\nabla \phi}{|\nabla \phi|}\right)\left|\nabla \phi\right| + v g_I\left(\left|\nabla I\right|\right)\left|\nabla \phi\right|$$
(1.14)

– The first term of Eq.(1.14) reduces the speed when active contour moves towards the zone where the object boundaries locate in.

– The Second term stops front propagation when active contour curve is near the edge boundaries.

When contour is located exactly on the object boundaries, the first and the second term are compensated. These two terms primarily depend on the edge map function in Eq.(1.4) and the

quality of this edge map determines the performance of the segmentation.

However, for low contrasted images, the gradient information is far from significant in Eq.(1.4). Moreover, the high gradients do not necessarily indicate the presence of real boundaries ([34]).

1.1.2   Expectation Maximization (EM) algorithm

In this section, we will first introduce the mixture probability density model ([35,36]) and Gaussian mixture probability density model ([37,38]). Next, we will introduce the standard EM algorithm ([12,39-42]). Then, we will introduce the EM algorithm for mixture probability density model ([43,44]) and Gaussian mixture probability density model ([45]), respectively.

In the domain of medical image analysis, the EM algorithm has been applied for visual enhancement of ultrasound images ([46]), and MRI image segmentation ([47]). Figure 1.5 shows the segmentation result of MRI image of the mouse heart ([47]).

(a)   (b)

Figure 1.5 Segmentation of mouse heart.

(a) original image. (b) segmentation result.

1.1.2.1   Mixture probability density model

The principle of mixture probability density model ([37]) is to decompose the probability density $f(x)$ into c components $f(\bullet \mid \Theta_k)$. These c components correspond to c classes. So we estimate

the parameters $\Theta_k (k = 1,...c)$ from a sample χ . χ is a set of n observed value x_i of a p-dimension vector:

$$\chi = \{x_1,...x_n\} \tag{1.15}$$

and the proportions π_k between different components represent the a priori probabilities of different classes:

$$\pi_k \in \{0,1\} \quad and \quad \sum_{k=1}^{c} \pi_k = 1 \tag{1.16}$$

Also, we denote $\Theta = [\pi_1,...\pi_c,\Theta_1,...\Theta_c]^T$ as the vector of parameters to be estimated. The probability density $f(x)$ is approximated by $f(x \mid \Theta)$ with parameters Θ :

$$f(x \mid \Theta) = \sum_{k=1}^{c} \pi_k f(x \mid \Theta_k) \tag{1.17}$$

1.1.2.2 Gaussian mixture probability density model

In Gaussian mixture probability density model ([38]), Θ_k is replaced by the mean μ_k and covariance matrix Σ_k of the kth class. The multi-dimension probability density is:

$$f(x \mid \Theta_k) = \frac{1}{(2\pi)^{p/2}\sqrt{|\Sigma_k|}} e^{-\frac{1}{2}(x-\mu_k)^T \Sigma_k^{-1}(x-\mu_k)} \tag{1.18}$$

where $|\Sigma_k|$ is the determinant of the $p \times p$ dimension covariance matrix.

Figure 1.6 illustrates one mixture of three Gaussian distributions (on the left), and the corresponding histogram (on the right). The solid line (on the left) shows three Gaussian distributions, and the dotted line (on the left) delineates the mixture of these three distributions.
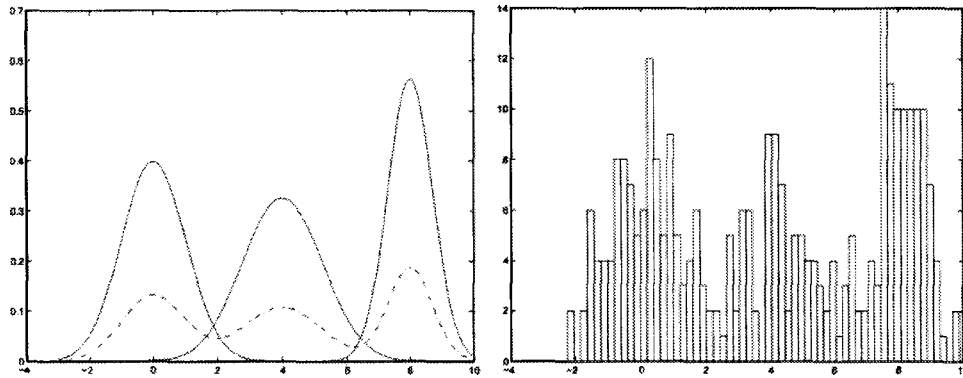
Figure 1.6 (Left) One mixture of three Gaussian distributions (dotted line) and their densities (solid line); (Right) The histogram of the mixture.

1.1.2.3 Standard EM algorithm

The algorithm of Expectation Maximization (EM) ([12,39-42]) is used in statistics for finding the maximum likelihood estimates of parameters in probabilistic models, where the model depends on unobserved latent variables. EM alternates between performing an Expectation (E) step, which computes an expectation of the likelihood by including the latent variables as if they were observed, and a Maximization (M) step, which computes the Maximum Likelihood (ML) estimates of the parameters by maximizing the expected likelihood found on the E step. The parameters found on the M step are then used to start another E step, and the process is repeated until certain criterion for convergence is met.

The probability of data related to parameter model Θ is:

$$L(\Theta) = P(X \mid \Theta) \tag{1.19}$$

If the data of set $\chi = \{x_1, ..., x_n\}$ is the sample which is independent of the random vector X, the probability is:

$$L(\Theta) = \prod_{i=1}^{n} f(x_i \mid \Theta) \tag{1.20}$$

14

In the case of mixture model, the above equation is changed to:

$$L(\Theta) = \prod_{i=1}^{n} \sum_{k=1}^{c} \pi_k f(x_i \mid \Theta_k)$$

(1.21)

The logarithm of the above equation is:

$$\log L(\Theta) = \sum_{i=1}^{n} \log \sum_{k=1}^{c} \pi_k f(x_i \mid \Theta_k)$$

(1.22)

In the estimation by maximization of probability, it is equivalent to obtain the roots of equation:

$$\frac{\partial \log L(\Theta)}{\partial \Theta} = 0$$

(1.23)

However, the random vector X is only a partial observation of considered phenomenon. As Eq.(1.22) is difficult to maximized directly, a random variable Z corresponding to the hidden incomplete data is introduced. Thus, the principle of maximization of probability can be used in a simple way. The algorithm EM is to facilitate the optimization procedure by estimating the absent data.

Denote $Y = (X, Z)$ as the complete data. Instead of maximizing $L(\Theta)$, we maximize iteratively the conditional expectation of the total probability:

$$L(\Theta \mid Y) = P(X, Z \mid \Theta)$$

(1.24)

Standard EM algorithm

Input: $\theta^{(0)}$, initial value of parameters; χ, a set of observations; ε, the convergence threshold of the algorithm.

Output: the optimal Θ^{*}

t=0;

Initialization of the model: $\hat{\Theta}^{(0)} = \theta^{(0)}$

Repeat

  (**E-step**) Calculation of the conditional expectation of the complete probability:

$$Q(\Theta \mid \hat{\Theta}^{(t)}) = E\left[L_c(\Theta) \mid X, \hat{\Theta}^{(t)}\right]$$

  (**M-Step**) Maximization of $Q(\Theta \mid \hat{\Theta}^{(t)})$:

$$\hat{\Theta}^{(t+1)} = \arg\max_{\Theta} Q(\Theta \mid \hat{\Theta}^{(t)})$$

  t=t+1;

Until $\left\| Q(\Theta \mid \hat{\Theta}^{(t+1)}) - Q(\Theta \mid \hat{\Theta}^{(t)}) \right\| < \varepsilon$

1.1.2.4 EM for the mixture probability density model

The algorithm EM is always used in classification with the mixture probability density model ([43,44]). For maximizing Eq.(1.22), it is easy to do if we know the belonging of each point to a specific class. We introduce a supplementary random vector Z corresponding to the belonging vector of one point x_i to the class C_k. Generally, the samples $z_i = (z_{i,1}, ..., z_{i,c})$ of Z are considered to be independent. For the element x_i:

$$z_{ik} = \begin{cases} 1 & \text{if } x_i \text{ belongs to class } C_k \\ 0 & \text{otherwise} \end{cases} \tag{1.25}$$

Under this condition, the equation is written as:

$$\log L(\Theta \mid Y) = \log(P(x, Z \mid \Theta))$$

$$= \log(\prod_{i=1}^{n} f(x_i, z_i \mid \Theta)) \tag{1.26}$$

$$= \log(\prod_{i=1}^{n} \prod_{k=1}^{c} (\pi_k f(x_i \mid \Theta_k))^{z_{ik}})$$

$$\log L(\Theta \mid Y) = \sum_{i=1}^{n} \sum_{k=1}^{c} z_{ik} \log(\pi_k f(x_i \mid \Theta_k)) \tag{1.27}$$

EM for the mixture probability density model

Input: c, the number of mixture components; $\theta^{(0)} = \left[\pi_1^{(0)}, \dots \pi_c^{(0)}, \theta_1^{(0)}, \dots \theta_c^{(0)} \right]$, the initial value of parameters of model; χ, the set of observations; ε, the convergence threshold of the algorithm.

Output: the optimal Θ^*

t=0;

Initialization of the model: $\hat{\Theta}^{(0)} = \theta^{(0)}$

Repeat

(E-step) calculation of a posteriori probability $\hat{z}_{ik}^{(t)}$:

$$\hat{z}_{ik}^{(t)} = \frac{\hat{\pi}_k^{(t)} f(x_i \mid \hat{\Theta}_k^{(t)})}{\sum_{l=1}^{c} \hat{\pi}_l^{(t)} f(x_i \mid \hat{\Theta}_l^{(t)})}$$

(M-step) maximization of $Q(\Theta \mid \hat{\Theta}^{(t)})$:

$$\hat{\Theta}^{(t+1)} = \arg\max_{\Theta} Q(\Theta \mid \hat{\Theta}^{(t)})$$

t=t+1;

Until $\left\| Q(\Theta \mid \hat{\Theta}^{(t+1)}) - Q(\Theta \mid \hat{\Theta}^{(t)})) \right\| < \varepsilon$

1.1.2.5 EM for the Gaussian mixture probability density model

The algorithm EM for the Gaussian mixture probability density model ([45]) is shown as follows. Figure 1.7 shows one example of applying EM to evaluate the parameters of a sample coming from the 8-component two-dimensional Gaussian Mixture Model.

This algorithm is usually used for estimation when learning data is incomplete. However, it is rather sensitive to initial values, and the convergence speed may be very slow.
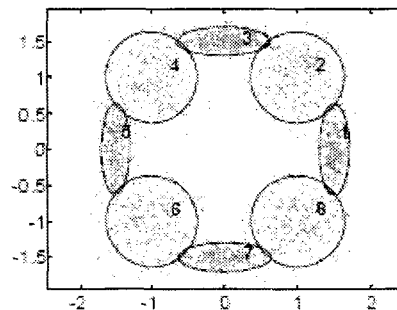
Figure 1.7 One example of applying EM to evaluate the parameters of a sample coming from the 8-component two-dimensional Gaussian Mixture Model.

EM for the Gaussian mixture probability density model

Input: c, the number of mixture components; χ , the set of observations; $\theta^{(0)} = \left[\pi_1^{(0)},...,\pi_c^{(0)},\mu_1^{(0)},\Sigma_1^{(0)},...,\mu_c^{(0)},\Sigma_c^{(0)} \right]$, the initial value of parameters of model; ε , the convergence threshold of the algorithm.

Output: the optimal Θ^*

t=0;

Initialization of the model: $\hat{\Theta}^{(0)} = \theta^{(0)}$

Repeat

(E-step) calculation of a posteriori probability $\hat{z}_{ik}^{(t)}$:

$$\hat{z}_{ik}^{(t)} = \frac{\hat{\pi}_k^{(t)} f(x_i \mid \hat{\Theta}_k^{(t)})}{\sum_{l=1}^{c} \hat{\pi}_l^{(t)} f(x_i \mid \hat{\Theta}_l^{(t)})}$$

(M-step) estimation of π_k, μ_k, Σ_k , maximization of $Q(\Theta \mid \hat{\Theta}^{(t)})$

Estimation of the a posteriori probability $\hat{\pi}_k$ of the kth class:

$$\hat{\pi}_k^{(t+1)} = \frac{\sum_{i=1}^{n} \hat{z}_{ik}^{(t)}}{n}$$

Estimation of the mean $\hat{\mu}_k$ of the kth class:

$$\hat{\mu}_k^{(t+1)} = \frac{\sum_{i=1}^{n} \hat{z}_{ik}^{(t)} x_i}{\sum_{i=1}^{n} \hat{z}_{ik}^{(t)}}$$

Estimation of the covariance matrix $\hat{\Sigma}_k$ of the kth class:

$$\hat{\Sigma}_k^{(t+1)} = \frac{\sum_{i=1}^{n} \hat{z}_{ik}^{(t)} (x_i - \hat{\mu}_k^{(t+1)})(x_i - \hat{\mu}_k^{(t+1)})^T}{\sum_{i=1}^{n} \hat{z}_{ik}^{(t)}}$$

t=t+1;

Until $\left\| Q(\Theta \mid \hat{\Theta}^{(t+1)}) - Q(\Theta \mid \hat{\Theta}^{(t)}) \right\| < \varepsilon$

1.1.2.6 An EM algorithm using the Gaussian mixture model with spatial constraint

In ([48]), an algorithm using the Gaussian Mixture Model with spatial constraint is proposed in order to take into account the density distribution of data for image segmentation. Thanks to the spatial constraint, this method is robust to noise. The objective function is:

$$
\begin{aligned}
J &= -\sum_{k=1}^{n} \log f(x_k \mid \Theta) - \frac{\alpha}{N_R} \sum_{k=1}^{n} \sum_{r \in N_k} \log f(x_r \mid \Theta) \\
&= -\sum_{k=1}^{n} \log \sum_{i=1}^{c} \pi_i f(x_k \mid \Theta_i) - \frac{\alpha}{N_R} \sum_{k=1}^{n} \sum_{r \in N_k} \log \sum_{i=1}^{c} \pi_i f(x_r \mid \Theta_i)
\end{aligned}
\tag{1.28}
$$

with

$$
\pi_i = \frac{\sum_{k=1}^{n} \left(z_{ik} + \frac{\alpha}{N_R} \sum_{r \in N_k} z_{ir} \right)}{\sum_{j=1}^{c} \sum_{k=1}^{n} \left(z_{jk} + \frac{\alpha}{N_R} \sum_{r \in N_k} z_{jr} \right)}
\tag{1.29}
$$

$$
\mu_i = \frac{\sum_{k=1}^{n} \left(z_{ik} x_k + \frac{\alpha}{N_R} \sum_{r \in N_k} z_{ir} x_r \right)}{\sum_{k=1}^{n} \left(z_{ik} + \frac{\alpha}{N_R} \sum_{r \in N_k} z_{ir} \right)}
\tag{1.30}
$$

$$
\Sigma_i = \frac{\sum_{k=1}^{n} \left[z_{ik} (x_k - \mu_i)(x_k - \mu_i)^T + \frac{\alpha}{N_R} \sum_{r \in N_K} z_{ir} (x_r - \mu_i)(x_r - \mu_i)^T \right]}{\sum_{k=1}^{n} \left(z_{ik} + \frac{\alpha}{N_R} \sum_{r \in N_k} z_{ir} \right)}
\tag{1.31}
$$

N_R : the cardinality. In Eq.(1.29)-Eq.(1.31), when, $\frac{1}{N_R} \sum_{r \in N_k} z_{ir}$ is considered to be:

– The mean of a group of variants, this method is called GMM_S_1.

– The median of a group of variants, this method is called GMM_S_2.

GMM_S_1 and GMM_S_2 are implemented in the same way as the EM for the Gaussian mixture probability density model is implemented (see section 1.1.2.5).

1.1.3   Fuzzy C-Means (FCM) algorithm

Fuzzy C-Means (FCM) is a popular clustering algorithm which is frequently applied to medical image segmentation. However, it is sensitive to noises. Many improvements have been proposed to deal with this defect. Most of them generate a penalty term describing spatial information of neighboring pixels and add it to the standard FCM objective function ([6,13,49-54]). The modified FCM objective functions can then become more spatially smooth for extracting complete objects from images ([55]). Figure 1.8 shows the segmentation for a MRI image of brain by KFCMS ([49]).

(a)   (b)
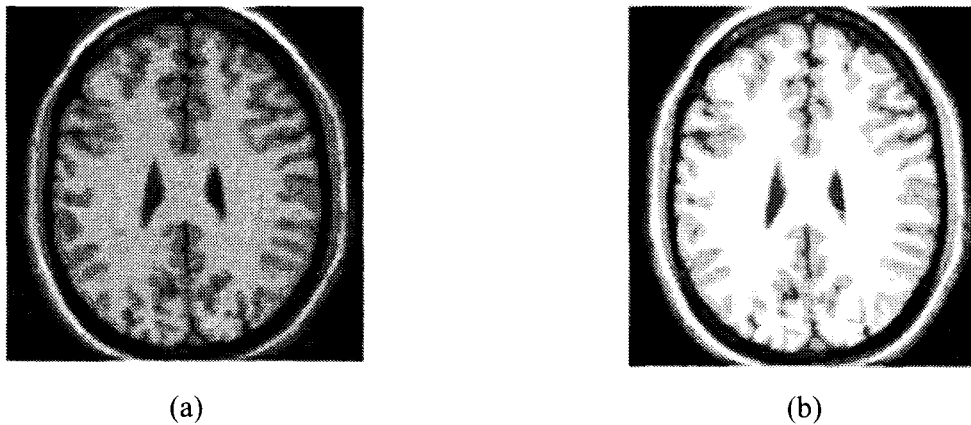
Figure 1.8 Segmentation for a MRI image of brain by KFCMS.
(a) original image. (b) segmentation by KFCMS.

In this section, we will first introduce the classical FCM algorithm. Then, we will introduce the FCM algorithm using Kernel with spatial constraints ([49]) and the FCM algorithm using Markov Random Field via Bayesian theory with spatial constraint ([56]).

1.1.3.1   Classical FCM algorithm

Let $X = (x_1, x_2, ...x_n)$ represent one set of n elements which will be classified into c clusters or classes. x_i denotes one element characterized by a multidimensional feature vector. The FCM method ([57-59]) is an iterative optimization which minimizes the objective function defined

below:

$$J = \sum_{j=1}^{n} \sum_{i=1}^{c} u_{ij}^{m} \left\| x_{j} - v_{i} \right\|^{2}$$

(1.32)

where

u_{ij} represents the adhesion of the element x_{j} to the ith cluster.

v_{i} is the center of the ith cluster.

$\left\| * \right\|$ is the Euclidean distance.

m is a constant controlling the fuzzy degree in the clustering process, and m=2 is usually used to facilitate the calculation.

$U = \left\{ u_{ij} \right\}$ represents one clustering matrix whose components meet:

$$u_{ik} \in \left[0,1 \right] \text{ with } \sum_{i=1}^{c} u_{ik} = 1 \text{ for any } k \text{ and } 0 < \sum_{k=1}^{n} u_{ik} < n \text{ for any } i$$

(1.33)

The objective function of FCM is minimized when high adhesion degrees are assigned to elements close to related cluster centers, and low adhesion degrees to elements far from related cluster centers.

The adhesion function represents the level of belonging of one element to a specific cluster. In the FCM method, it only depends on the distance between one element and each cluster center. The adhesion function and the cluster center are updated using Eq.(1.34) and Eq.(1.35).

$$u_{ij} = \frac{1}{\sum_{k=1}^{c} \left(\frac{\left\| x_{j} - v_{i} \right\|}{\left\| x_{j} - v_{k} \right\|} \right)^{\frac{2}{m-1}}}$$

(1.34)

$$v_{i} = \frac{\sum_{j=1}^{n} u_{ij}^{m} x_{j}}{\sum_{j=1}^{n} u_{ij}^{m}}$$

(1.35)

When $\left\| U^{(t+1)} - U^{(t)} \right\| < \varepsilon$ (two neighboring iterations give very close results), stop the algorithm.

Classical FCM

Input: c, the number of cluster; m, the coefficient controlling the fuzzy degree; ε, the value for convergence; u_{ij}^0, initial memberships.

Output: the partition matrix U

t=0;

Repeat

> Update cluster centers $v_i^{(t)}$ by Eq.(1.35)
>
> Update membership degrees $u_{ij}^{(t)}$ using Eq.(1.34)
>
> t=t+1;

Until $\left\| u_{ij}^{(t+1)} - u_{ij}^{(t)} \right\| < \varepsilon$

Figure 1.9 illustrates the classification by FCM. There are four classes to be segmented (C_1, C_2, C_3, C_4 in Figure 1.9). The square in each sub-region is the cluster center of the corresponding class (V_1, V_2, V_3, V_4 in Figure 1.9).

Different from the hard partition methods ([58]) which force each element to belong to one class exclusively, FCM permits each element to have different belongingness to each class. So it can maintain much more information of original image when we use it for image segmentation. Nevertheless, it is more sensitive to noises related to the other grey level-based methods. Many methods have been proposed to cope with this problem. Most of them generate a penalty term describing spatial information of neighboring pixels and add it to the standard FCM objective function ([6,13,49-54]). The modified FCM objective functions can then become more spatially smooth for extracting complete objects from images ([55]). Next, we will introduce the FCM algorithm using Kernel with spatial constraints ([49]) and the FCM algorithm using Markov

---

Random Field via Bayesian theory with spatial constraint ([56]).
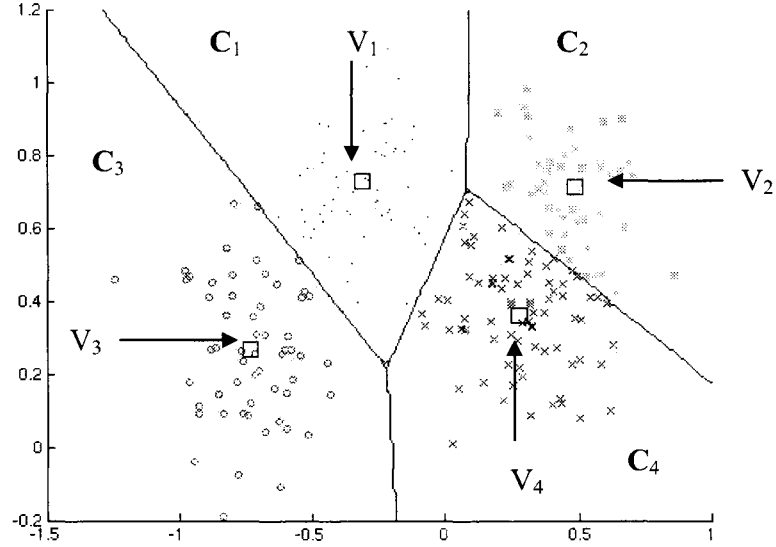
Figure 1.9 One example of FCM.

(C_1, C_2, C_3, C_4 are the four classes, and V_1, V_2, V_3, V_4 are the four corresponding initial cluster centers).

1.1.3.2   A FCM algorithm based on kernel with spatial constraints

In ([50]), an approach was proposed to increase the robustness of FCM to noises by directly modifying the objective function of FCM as follows:

$$J = \sum_{i=1}^{c} \sum_{k=1}^{n} u_{ik}^{m} \left\| x_k - v_i \right\|^2 + \frac{\alpha}{N} \sum_{i=1}^{c} \sum_{k=1}^{n} u_{ik}^{m} \sum_{r \in N_k} \left\| x_r - v_i \right\|^2 \qquad (1.36)$$

where

u_{ik} represents the adhesion of the element x_k to the ith cluster.

v_i is the center of the ith cluster.

$\|*\|$ is the Euclidean distance.

m is a constant controlling the fuzzy degree in the clustering process, and m=2 is usually used

to facilitate the calculation.

$U = \{u_{ij}\}$ represents one clustering matrix whose components meet:

$$u_{ik} \in [0,1] \text{ with } \sum_{i=1}^{c} u_{ik} = 1 \text{ for any } k \text{ and } 0 < \sum_{k=1}^{n} u_{ik} < n \text{ for any } i \tag{1.37}$$

α is the importance coefficient of the penalty term (the second term in Eq.(1.36)).

N_k stands for the set of neighbors falling into a window around x_k, and

N_R is the cardinality.

In fact, the penalty term formulates a spatial constraint and aims at keeping continuity on neighboring pixel values around x_k. Similar with the standard FCM algorithm, this method minimize the objective function under the constraints of U as stated in Eq.(1.37). A necessary condition on u_{ik} and v_i for Eq.(1.36) to be at a local minimum is:

$$u_{ik} = \frac{\left(\|x_k - v_i\|^2 + \frac{\alpha}{N_R} \sum_{r \in N_k} \|x_r - v_i\|^2 \right)^{-\frac{1}{(m-1)}}}{\sum_{j=1}^{c} \left(\|x_k - v_j\|^2 + \frac{\alpha}{N_R} \sum_{r \in N_k} \|x_r - v_j\|^2 \right)^{-\frac{1}{(m-1)}}} \tag{1.38}$$

$$v_i = \frac{\sum_{k=1}^{n} u_{ik}^m \left(x_k + \frac{\alpha}{N_R} \sum_{r \in N_k} x_r \right)}{(1+\alpha) \sum_{k=1}^{n} u_{ik}^m} \tag{1.39}$$

A shortcoming of Eq.(1.38) and Eq.(1.39) is that computing the neighborhood terms will take much more time than the standard FCM.

In ([49]), the authors tried to modify Eq. (1.36) in order to decrease the computational complexity. They used $\|\bar{x}_k - v_i\|^2$ to replace $(1/N_R) \sum_{r \in N_k} \|x_r - v_i\|^2$ to save the clustering time, $\bar{x}_k$ can be the

mean or the median of the neighboring pixels within a window centered on x_k, and it can be computed in advance. Thus, the simplified objective function can be rewritten as:

$$J = \sum_{i=1}^{c}\sum_{k=1}^{n} u_{ik}^{m}\left\|x_k - v_i\right\|^2 + \alpha\sum_{i=1}^{c}\sum_{k=1}^{n} u_{ik}^{m}\left\|\bar{x}_k - v_i\right\|^2 \qquad (1.40)$$

Similarly, we have:

$$u_{ik} = \frac{\left(\left\|x_k - v_i\right\|^2 + \alpha\left\|\bar{x}_k - v_i\right\|^2\right)^{-\frac{1}{(m-1)}}}{\sum_{j=1}^{c}\left(\left\|x_k - v_j\right\|^2 + \alpha\left\|\bar{x}_k - v_j\right\|^2\right)^{-\frac{1}{(m-1)}}} \qquad (1.41)$$

$$v_i = \frac{\sum_{k=1}^{n} u_{ik}^{m}\left(x_k + \alpha\bar{x}_k\right)}{(1+\alpha)\sum_{k=1}^{n} u_{ik}^{m}} \qquad (1.42)$$

For the convenience of notation,

– When $\bar{x}_k$ represents the mean of the neighboring pixels within a window centered on x_k, the algorithm using Eq.(1.41) and Eq.(1.42) is named as FCM_S$_1$.

– When $\bar{x}_k$ is median of the pixels in this window, the algorithm is named as FCM_S$_2$.

FCM_S$_1$ and FCM_S$_2$

Input: c, the number of cluster; m, the coefficient controlling the fuzzy degree; ε, the convergence threshold; u_{ij}^0, the initial membership degrees.

Output: the partition matrix U

t=0;

Repeat

Calculate the means and medians $\overline{x}_k$ (mean for FCM_S$_1$ and median for FCM_S$_2$)

Update the membership degrees $u_{ij}^{(t)}$ using Eq.(1.41)

Update the cluster centers $v_i^{(t)}$ using Eq.(1.42)

t=t+1;

Until $\left\| v^{(t+1)} - v^{(t)} \right\| < \varepsilon$

Next, in ([49]), the authors replaced the Euclidean distance in the standard FCM algorithm by a kernel-induced distance ([60-63]) and add a penalty term to represent spatial contextual information. This kernel-induced distance is a robust non-Euclidean distance measure in the original data space to derive new objective functions and performs clustering under non-Euclidean data structure. This kernel method is presented as follows.

Let $\Phi: x \in X \subseteq R^d \mapsto \Phi(x) \in F \subseteq R^H$ $(d \ll H)$ be a nonlinear transformation into a higher (possibly infinite) dimensional feature space F. In order to explain how to use the kernel methods, we recall a simple example given in ([64]). If $x = [x_1, x_2]^T$ and $\Phi(x) = \left[x_1^2, \sqrt{2}x_1x_2, x_2^2 \right]^T$, where x$_i$ is the ith component of the vector x. Then the inner product between $\Phi(x)$ and $\Phi(y)$ in the feature space F is:

$$\Phi(x)^T \Phi(y) = \left[(x_1)^2, \sqrt{2}x_1x_2, (x_2)^2 \right]^T \left[(y_1)^2, \sqrt{2}y_1y_2, (y_2)^2 \right] = (x^T y)^2 = K(x, y) \qquad (1.43)$$

Thus, in order to compute the inner products in F, we can use the kernel representation $K(x, y)$, without explicitly giving the corresponding transformation or mapping function Φ. It is a direct consequence from ([60]), i.e., every linear algorithm that only uses inner products can be easily extended to a nonlinear version only through the kernels satisfying the Mercer's condition ([60]). Typical Radial Basis Function (RBF) and polynomial kernels are given as follows:

$$K(x, y) = \exp\left(\frac{-(\sum_{i=1}^{d} |x_i - y_i|^a)^b}{\sigma^2} \right) \qquad (1.44)$$

where d is the dimension of the vector x, $a \geq 0, 1 \leq b \leq 2$.

Obviously, $K(x, x) = 1$ is held for all x and the above RBF kernels, and a polynomial of p degree:

$$K(x, y) = (x^T y + 1)^p \qquad (1.45)$$

We now construct the kernelized version of the FCM algorithm and modify its objective function with the mapping Φ as follows:

$$J^\Phi = \sum_{i=1}^{c} \sum_{k=1}^{n} u_{ik}^m \| \Phi(x_k) - \Phi(v_i) \|^2 \qquad (1.46)$$

Now through the kernel substitution, we have:

$$\begin{aligned}
\| \Phi(x_k) - \Phi(v_i) \|^2 &= \left(\Phi(x_k) - \Phi(v_i) \right)^T \left(\Phi(x_k) - \Phi(v_i) \right) \\
&= \Phi(x_k)^T \Phi(x_k) - \Phi(v_i)^T \Phi(x_k) \\
&\quad - \Phi(x_k)^T \Phi(v_i) + \Phi(v_i)^T \Phi(v_i) \\
&= K(x_k, x_k) + K(v_i, v_i) - 2K(x_k, v_i)
\end{aligned} \qquad (1.47)$$

In this way, a new non-Euclidean distance measure in original data space is obtained. Obviously, different kernels will induce different measures in the original space, leading to a new family of clustering algorithms. In particular, if the kernel function $K(x, y)$ is taken as the RBF in Eq.(1.44),

Eq.(1.47) can be simplified to $2(1 - K(x_k, v_i))$. Furthermore, for sake of convenience, we only consider the Gaussian RBF (GRBF) kernel with a=2 and b=1 in Eq.(1.44). Then, Eq.(1.46) can be rewritten as:

$$J^{\Phi} = 2\sum_{i=1}^{c}\sum_{k=1}^{n} u_{ik}^{m}(1 - K(x_k, v_i)) \tag{1.48}$$

with

$$u_{ik} = \frac{\left(1 - K(x_k, v_i)\right)^{\frac{1}{-(m-1)}}}{\sum_{j=1}^{c}\left(1 - K(x_k, v_j)\right)^{\frac{1}{-(m-1)}}} \tag{1.49}$$

$$v_i = \frac{\sum_{k=1}^{n} u_{ik}^{m} K(x_k, v_i) x_k}{\sum_{k=1}^{n} u_{ik}^{m} K(x_k, v_i)} \tag{1.50}$$

Similarly, a kernelized modification in Eq.(1.40) is:

$$J_m = \sum_{i=1}^{c}\sum_{k=1}^{n} u_{ik}^{m}(1 - K(x_k, v_i)) + \alpha\sum_{i=1}^{c}\sum_{k=1}^{n} u_{ik}^{m}(1 - K(\overline{x}_k, v_i)) \tag{1.51}$$

with

$$u_{ik} = \frac{\left((1 - K(x_k, v_i)) + \alpha(1 - K(\overline{x}_k, v_i))\right)^{\frac{1}{-(m-1)}}}{\sum_{j=1}^{c}\left((1 - K(x_k, v_j)) + \alpha(1 - K(\overline{x}_k, v_j))\right)^{\frac{1}{-(m-1)}}} \tag{1.52}$$

$$v_i = \frac{\sum_{k=1}^{n} u_{ik}^{m}(K(x_k, v_i)x_k + \alpha K(\overline{x}_k, v_i)\overline{x}_k)}{\sum_{k=1}^{n} u_{ik}^{m}(K(x_k, v_i) + \alpha K(\overline{x}_k, v_i))} \tag{1.53}$$

For the convenience of notation,

– When $\overline{x}_k$ is mean of neighboring pixels within a window centered on x_k, the algorithm using Eq.(1.52) and Eq.(1.53) is named as KFCM_S$_1$,

– When $\overline{x}_k$ is median, the algorithm is named as KFCM_S$_2$.

KFCM_S_1 and KFCM_S_2 are implemented in the same way as FCM_S_1 and FCM_S_2 are implemented.

1.1.3.3 A FCM algorithm based on Markov Random Field via Bayesian theory with spatial constraint

Much of work has been done in Markov Random Field (MRF) modeling and its application in image segmentation ([65-68]). The main advantage of the MRF model is that it provides a general and natural model for the interaction between spatially related random variables. A novel generalized FCM (NGFCM) algorithm with spatial constraints based on MRF for image segmentation is proposed in ([56]). In this algorithm, a model for the membership functions which incorporates local correlation is given by MRF defined through a Gibbs function in order to improve the robustness of FCM to noises. The spatial information is incorporated into the FCM objective function by Bayesian theory. The new objective function includes a penalty term based on MRF. The penalty term tends to favor identical membership values for two neighboring pixels. Therefore, the proposed algorithm has both the advantages of the FCM and MRF and is robust to noise. We will first introduce the MRF theory and Gibbs distribution, then the NGFCM algorithm.

Let $Y = \{Y_1, ... Y_n\}$ be a family of random variables defined on the set of sites $S = \{1, 2, ... n\}$, in which each random variable Y_i takes a value y_i in the set of labels $L = \{1, 2, ... n\}$. The family Y is called a random field ([66]). The joint event $(Y_1 = y_1, ..., Y_n = y_n)$ is abbreviated as Y=y where $y = \{y_1, ..., y_n\}$ is a configuration of Y, corresponding to a realization of this random field.

In an MRF, the sites in S are related to one another via a neighborhood system, which is defined as $M = \{M_i, i \in S\}$, where M_i is the set of neighboring sites of i, $i \in M_i$ and $i \in M_j \Leftrightarrow j \in M_i$. A random field Y is called a MRF on S with respect to a neighborhood system M if and only if:

$$P(y) > 0, \text{ for all } y$$
$$P(y_i \mid y_{S-\{i\}}) = P(y_i \mid y_{M_i})$$
(1.54)

A MRF can be characterized by a Gibbs distribution ([65]). Thus, we have:

$$P(y) = Z^{-1} \exp(-Q(y))$$
(1.55)

where

Z is a normalized constant called the partition function and Q(x) is an energy function of the form:

$$Q(y) = \sum_{c \in C} R_c(y)$$
(1.56)

which is the sum of clique potentials $R_c(y)$ over all possible cliques C. A clique c is defined as a subset of sites in S in which every pair of distinct sites are neighbors. The value of $R_c(y)$ depends on the local configuration of clique c.

Intuitively speaking, in most cases it is desirable to assign the same cluster label to spatially adjacent pixels. The Bayesian framework provides a natural approach to implement these ideas. The following is the formulation, a likelihood term which is exclusively based on the data captures the pixel intensity information, while a prior biasing term that uses a MRF captures the spatial location information ([69]).

Inspired by the above ideas, a prior distribution of the membership functions that incorporates local correlation is given by MRF defined through a Gibbs function ([65]):

$$p(U) = Z^{-1} \exp(-Q(U))$$
(1.57)

where

U is the clustering matrix in standard FCM, and

$$Q(U) = \frac{\alpha}{2} \sum_{k=1}^{n} R_{M_k}(U)$$
(1.58)

Z is a normalized constant, while α is often called regularization parameter. The function

$R_{M_k}(U)$ denotes the clique potential function of the membership function $\{u_{ik}\}$ in FCM within the neighborhood M_k of the kth pixel and can be computed as follows:

$$R_{M_k}(U) = \sum_{l \in M_k} \sum_{i=1}^{c} (u_{ik} - u_{il})^2 \tag{1.59}$$

Then, the prior distribution of the parameter set U can be rewritten as:

$$p(U) \propto \exp\left\{-\frac{\alpha}{2} \sum_{i=1}^{c} \sum_{k=1}^{n} \sum_{l \in M_k} (u_{ik} - u_{il})^2\right\} \tag{1.60}$$

Given the prior distribution, a posteriori distribution of the membership functions can be expressed by:

$$p(U \mid X, V) \propto p(X \mid U, V) p(U) \tag{1.61}$$

where X is a dataset, and $V = [v_1, v_2, ..., v_c]$ is the vector of cluster centroids. The first term on the right-hand side of Eq.(1.83) is a likelihood probability. It is modeled as:

$$p(X \mid U, V) \propto \exp\left\{-\sum_{i=1}^{c} \sum_{k=1}^{n} u_{ik}^m \|x_k - v_i\|^2\right\} \tag{1.62}$$

In the Bayesian framework, the fuzzy membership functions are computed by:

$$U^* = \underset{U}{\mathrm{argmax}}\, p(U \mid X, V) \tag{1.63}$$

Applying a logarithmic transformation to Eq.(1.61) we can obtain:

$$\log p(U \mid X, V) \propto \log p(X \mid U, V) + \log p(U) \tag{1.64}$$

Then

$$\log p(U \mid X, V) \propto -\sum_{i=1}^{c} \sum_{k=1}^{n} u_{ik}^m \|x_k - v_i\|^2 - \frac{\alpha}{2} \sum_{i=1}^{c} \sum_{k=1}^{n} \sum_{l \in M_k} (u_{ik} - u_{il})^2 \tag{1.65}$$

Therefore, the Maximum A Posteriori (MAP) estimation is equivalent to the minimization of the following objective function:

$$J = \sum_{i=1}^{c} \sum_{k=1}^{n} u_{ik}^m \|x_k - v_i\|^2 + \frac{\alpha}{2} \sum_{i=1}^{c} \sum_{k=1}^{n} \sum_{l \in M_k} (u_{ik} - u_{il})^2 \tag{1.66}$$

The first term of Eq.(1.66) is minimized when high membership values are assigned to pixels whose grey levels are close to the centroids of the corresponding classes, and low membership values are assigned to pixels whose grey levels are far from the centroids. The penalty term of Eq.(1.66) is minimized when the membership values of each pixel are close to those of its neighboring pixels. That is to say, the penalty term of Eq.(1.66) is minimized when the same cluster label is assigned to spatially adjacent pixels. Therefore, the proposed method has both the advantages of the FCM and the MRF.

In this method, m=2. So the adhesion function u_{ik} and the cluster center v_i are updated using Eq.(1.67) and Eq.(1.68), where $|M_k|$ is the cardinality of the set M_k. NGFCM is implemented in the same way as the FCM is implemented.

$$u_{ik} = \frac{\left(\left\| x_k - v_i \right\|^2 + \alpha \left| M_k \right| \right)^{-1}}{\sum_{j=1}^{c} \left(\left\| x_k - v_j \right\|^2 + \alpha \left| M_k \right| \right)^{-1}} \left(1 + \sum_{j=1}^{c} \frac{\alpha \sum_{l \in M_k} (u_{il} - u_{jl})}{\left\| x_k - v_i \right\|^2 + \alpha \left| M_k \right|} \right)$$
(1.67)

$$v_i = \frac{\sum_{k=1}^{n} u_{ik}^2 x_k}{\sum_{k=1}^{n} u_{ik}^2}$$
(1.68)

In this section, we have introduced medical image segmentation methods. Next, we will introduce three automatic tissue classification systems.

1.2 Automatic tissue classification systems

Medical image analysis has great significance in various applications, such as the quantification of human body composition. The first step of medical image analysis is the image segmentation. In most of the existing work [70-74]), the tissues are classified manually by the experts. However, this work is too repetitive and laborious. In contrast, various tissue classification systems have

been recently developed. These systems have been developed for special applications, such as the classification system of brain tissues, the analysis system for bone composition, and the diagnosis system for chest image. We emphasize the "specification" of these systems in three aspects: hypothesis of entry, the rules, and the results. Next, we will introduce these three systems to show their limitations and justify our tissue classification system.

1.2.1 The classification system of brain tissues

Different systems of brain tissue classification have been proposed in the literature. We just focus on several typical systems presented in ([14-16]).

In ([14]), the authors proposed a knowledge-based approach for automatic classification and tissue labeling of 2D MRI images of human brain. The system consists of two components: a clustering algorithm and an expert system. MRI images are initially segmented by the unsupervised fuzzy c-means algorithm ([75,76]), then the expert system uses model-based recognition techniques to locate a landmark tissue. Qualitative models of brain tissues are defined and matched with their instances from images. If a significant deformation is detected in a tissue, the slice is classified to be abnormal. Otherwise, the expert system locates the next landmark tissue according to known expected tissue. This process is repeated until either a classification decision is reached that the slice is abnormal or all tissues of the slice are labeled.

The sequential stages of classification and tissue labeling are summarized as follows.

– Separate skull tissues from tissues of interest, namely, the white matter, grey matter, cerebro-spinal fluid (CSF), and abnormal tissues.

– Locate white matter. The shape of white matter is usually significantly deformed by large abnormal tissues.

– Use white matter to locate CSF, if white matter is note significantly deformed. A symmetric measure of CSF indicates whether it contains an abnormal tissue.

– Locate grey matter, if both white matter and CSF are believed to be normal. If there are deformations less significant in white matter, a final analysis is done at this stage with knowledge of white matter and CSF.

Each slice of interest for this study consists of three feature images: T1-weighted (T1), Proton Density (PD), and T2-weighted (T2). Figure 1.10 shows the feature images of different slices of interest. In this study, there are two sources of knowledge: (a) anatomical structure of tissues; (b) distribution of class centers in feature space. The features are different image intensities. Both kinds of knowledge are acquired from image anatomy ([77]) and experimental observation.

(a)   (b)   (c)
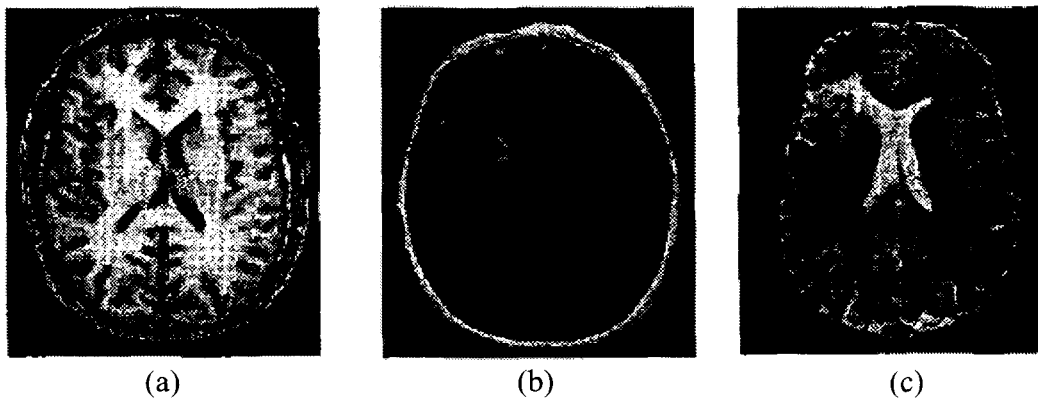
Figure 1.10 Feature images of different slices.
(a). T1-weighted. (b) Proton Density. (c) T2-weighted.

Since slices are processed without a priori knowledge of their being normal or abnormal, ten classes are chosen for each slice. This may lead to over-segmentation of tissues in normal slices, but reduces the chance that tumors are clustered into classes that contain normal tissues. The unsupervised FCM clustering algorithm takes a slice consisting of three images as input and clusters them into ten classes, each class has a cluster center <T1, PD, T2>. Figure 1.11 shows the ten class centers of two slices in the T1, PD, and T2 space. Six characters are used to represent, from left to right,

– Classes of air (A),

– Skull tissues (B),

– White matter (W),

– Grey matter (G),

– Tumor (T),

– and CSF (C), respectively.
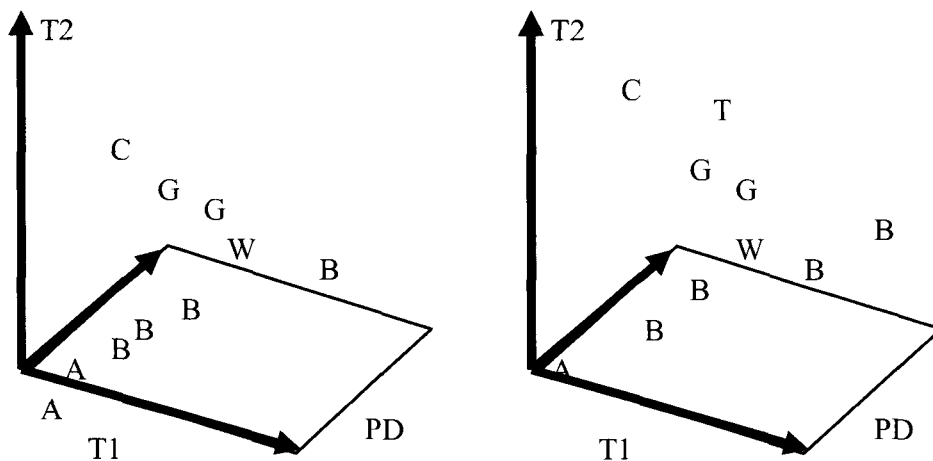
Figure 1.11 Class centers in T1, PD, and T2 spaces.

The class centers in feature space can be better illustrated by projecting them into T1 and T2 space. Figure 1.12 is obtained by projecting the two plots in Figure 1.11 into T1 and T2 space, respectively. The knowledge obtained from the class center distribution is used in locating the landmark tissues. It consists of the following, as illustrated by the T2 spectrum (Figure 1.13).

– Air always appears in the lowest one or two segmented classes.

– Tumor always appears as the highest or the second highest T2 class. It may be in a class of its own or in the class of CSF.

– CSF takes the highest T2 class in the absence of tumors, and the highest or second highest T2 class in the presence of tumors.

– Skull tissues (fat, skin, and bone) are scattered into three to four classes. Two to three classes of

the smallest T2 values, next to air, are skull tissues.

– White matter is clustered into one to two classes. It is smaller in T2 than grey matter and sometimes smaller than one to two skull classes.

– Grey matter is clustered into one to three classes which are higher in T2 than white matter and skull tissues.
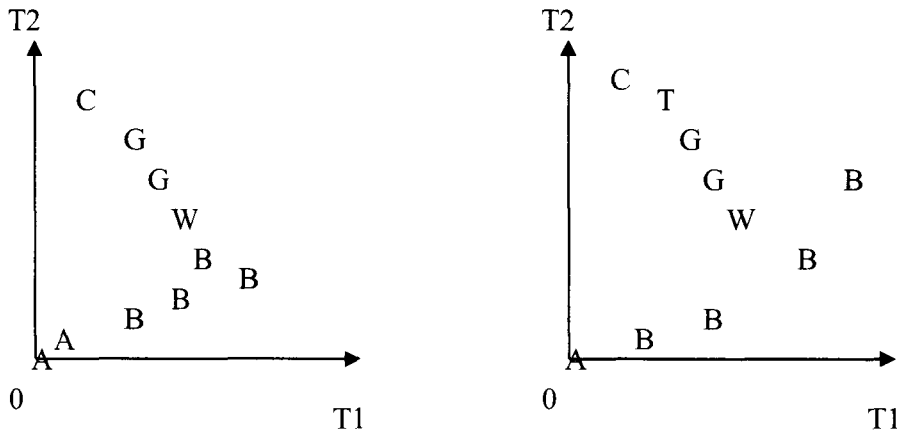
Figure 1.12 Corresponding class centers in T1, T2 space.
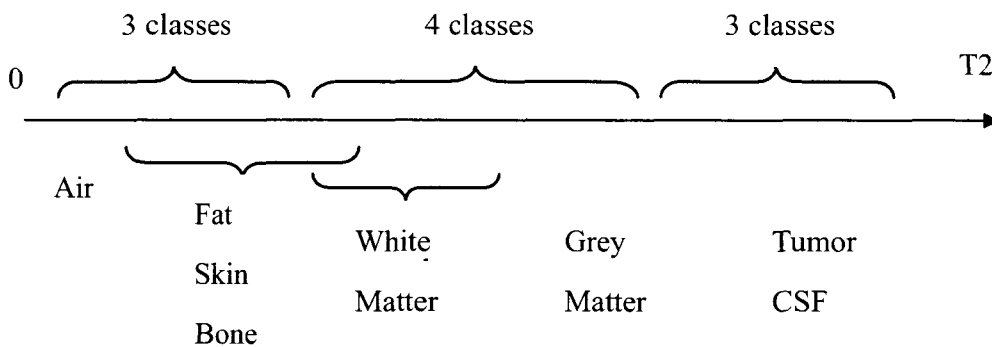
Figure 1.13 Class center distribution in the T2 spectrum.

Figure 1.14 shows the classification on abnormal slices.

Although this system shows good performance of classification, it has obvious disadvantages:

– First, the sequence of classification for each tissue is fixed by human, but not machine. So this system is lack of intelligence.

– Second, the choice of number of class (ten classes) for segmenting the image is not determined

systematically, but by the authors of ([14]). And the authors do not give any reason why they choose ten classes.
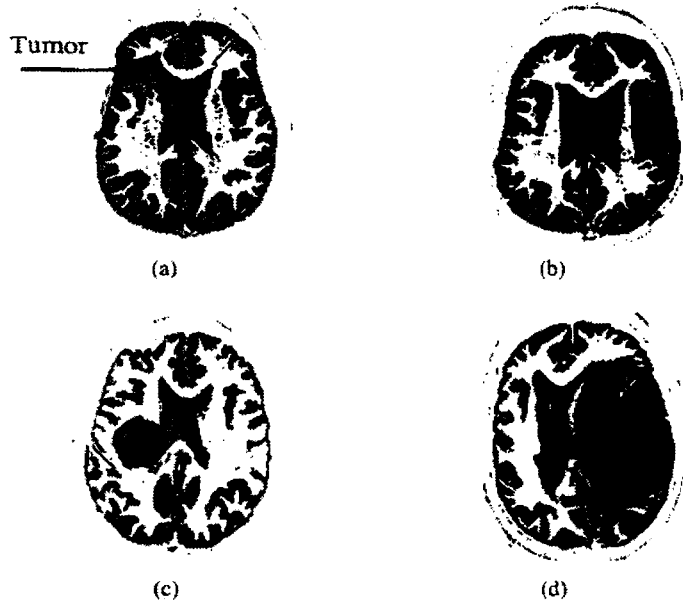
Figure 1.14 Tissue labeling of abnormal slices.

(a). complete labeling. (b). CSF and tumor not labeled. (c). CSF and tumor not labeled. (d). only white matter labeled

1.2.2 The analysis system for bone composition

Characteristics of microscopic structures in bone cross sections can be used to infer the biological age of the bone ([78,79]). The ability to do this accurately and reliably is useful in histological studies of bones, such as in determination of age at death. More importantly, reliable analysis of bone cross sections will play a vital role in understanding of bone growth and bone diseases such as osteoporosis, as developments at the microscopic level of the bone can be observed.

The important features in the bone cross section are the Harvesian canals, osteons, osteon fragments, and lamellar bone. These features are identified in Figure 1.15. The Harvesian canals, which are quite easily identified in the image, are the black areas, and they correspond to blood vessels in the bone. Osteons regions refer to the grey regions surrounding the canals. Different intensity levels of the osteon regions indicate the levels of bone mineralization, where the lighter

regions are more mineralized. The osteon fragments are the osteon regions that do not surround any canals. The brightest parts in the image that do not constitute the other regions are called the lamellar bone regions.
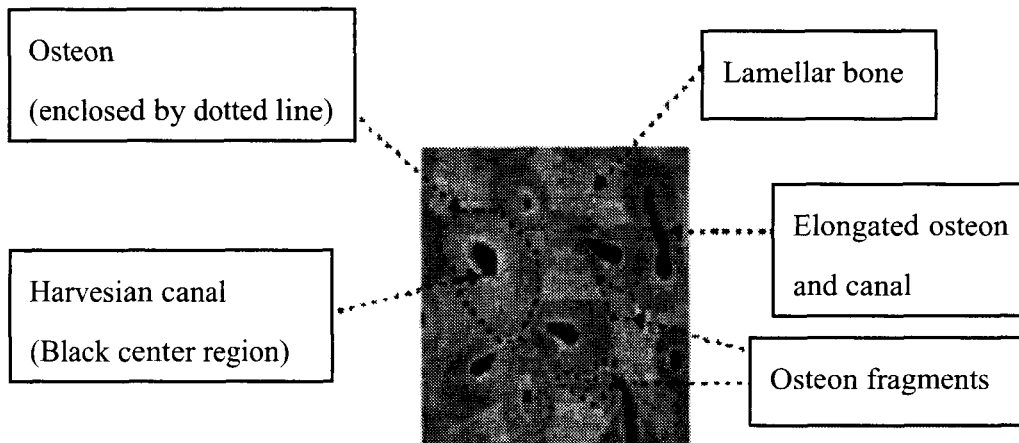
Figure 1.15 Magnified microradiograph of bone with features identified.

Traditionally the bone analysis is carried out by manual processes. In ([80]), an automatic system for bone image processing is developed. The input to the system is a magnified microradiographic bone image. And the output of the system are a segmented image and quantitative measurements of the features extracted from the image. There are four main steps involved in the processing of a bone cross section image:

− Preprocessing − adaptive neighborhood smoothing

− Clustering − k-means clustering

− Relabeling of regions

− Quantitative analysis of segmented images

Figure 1.16 shows the segmentation result using this system. The regions in the bone cross section have been identified quite successfully, with the canals, osteons and lamellar assigned to different clusters. There are, however, noticeable segmentation errors, particularly in some processed images, bright patches (due to imaging artifacts) surrounding canals have been misclassified as lamellar regions. Figure 1.17 shows a magnified section of a segmented image containing an osteon. These inaccuracies in segmentation area consequence of the simplicity of the clustering

method as it relies only on pixel grey level for segmentation.

(a)   (b)
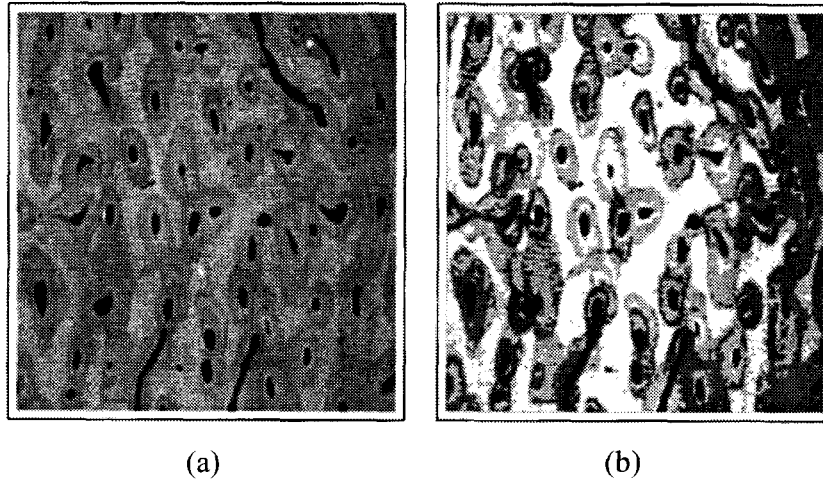
Figure 1.16 An example result of processing a bone image using the system.
(a) Original image. (b) Segmented image.
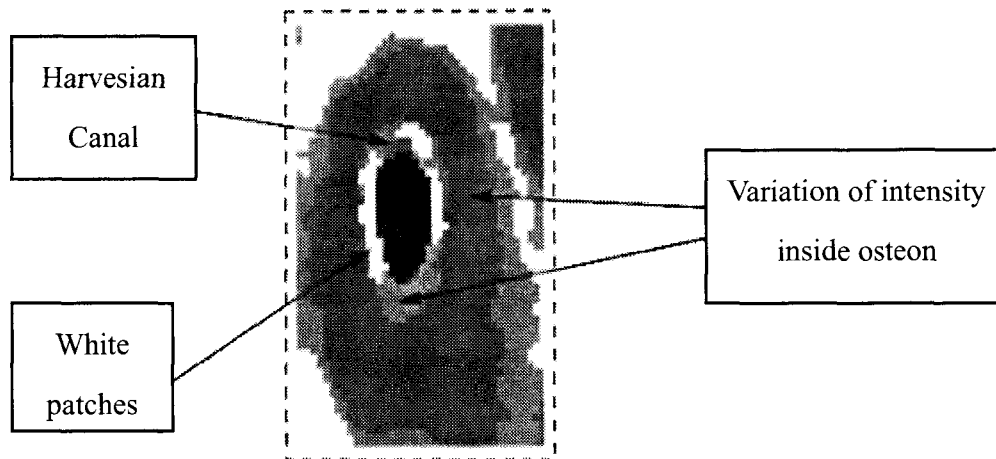
Figure 1.17 A magnified section of a segmented image containing an osteon.

To improve the system performance in terms of accurate bone image segmentation and quantification, a new system that makes appropriate use of the available knowledge of bone structures is developed ([17]). Figure 1.18 shows the basic framework of the processing algorithm implemented.

In the step of region merging, the a priori knowledge about the microradiographic bone images is

used to merge the extracted regions:

– Pixels within a specific osteon region should have the same or similar intensity level.

– Different osteon regions can contain pixels of different intensities where lighter osteon regions will correspond to more mineralized osteons, or osteon fragments that do not surround any canals.

– The shape of an osteon should be relatively regular, expanding from the shape of the canal contained inside.

– The region immediately surrounding a canal must be an osteon region.

– An osteon region is usually surrounded by lamellar pixels, unless it is touching another osteon.
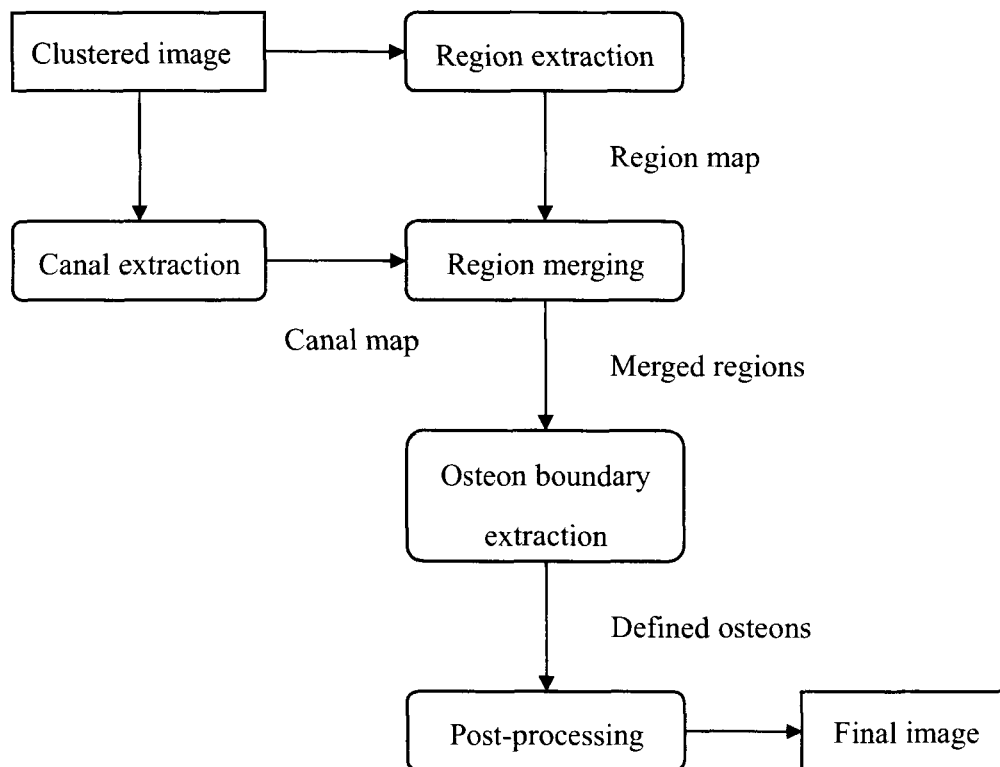
Figure 1.18 System diagram.

Figure 1.19 shows a processed bone image using the new system. Figure 1.20 shows a magnified section of this processed image. From Figure 1.19 and Figure 1.20, it can be observed that the white patches that were apparent in segmented images using k-means clustering, as that shown in Figure 1.16(b), are no longer present. Furthermore, each osteon region surrounding a canal has

been identified and labeled consistently as one of the three classes of osteon regions: dark osteon, osteon, or light osteon.

In summary, this new image analysis system for quantitative bone image analysis uses the spatial knowledge such as relationship between canals and osteons, expected shape of osteons, and the extent of osteons. The use of knowledge about bone cross section characteristics and microradiographs contributes to obtaining quantitative analysis results with greater accuracy and consistency compared to pixel-based algorithm that uses a simple clustering technique for segmentation. However, this system can only be applied to bone image analysis. Thus it lacks of generality for analysis of other anatomical structures.

(a)   (b)
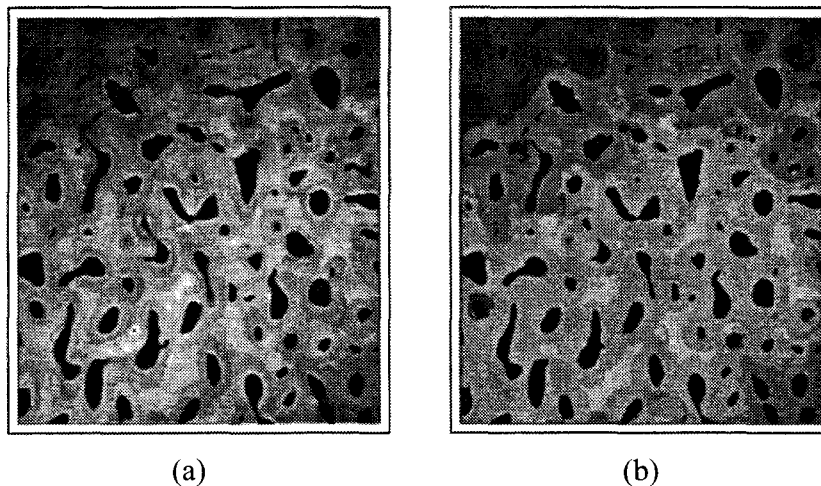
Figure 1.19 Segmentation using the new system.
(a) the original image and (b) the segmented image.
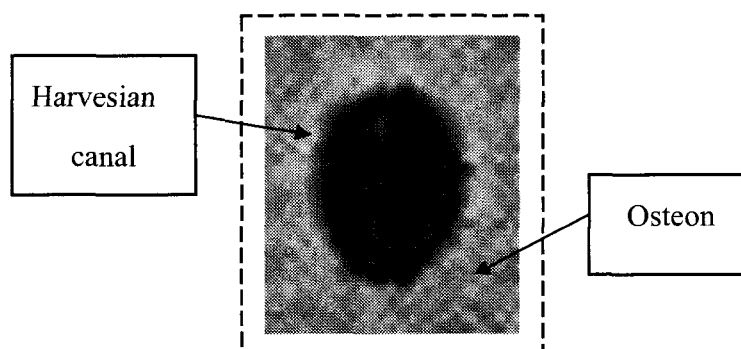
Figure 1.20 A magnified section of a segmented image containing an osteon.

1.2.3   The diagnosis system for chest

In ([18]), the authors developed an automated and knowledge-based method for segmenting chest computed tomography (CT) datasets. Anatomical knowledge including expected volume, shape, relative position, and X-ray attenuation of organs, provides feature constraints that guide the segmentation process. Knowledge is represented at a high level using an explicit anatomical model. The model is stored in a frame-based semantic network ([81]) and anatomical variability is incorporated using fuzzy sets ([82]).

In this system, anatomical knowledge is represented explicitly in a model, rather than implicitly within the segmentation algorithm. The knowledge contains information about specific anatomical parts, including expected size, shape, and location relative to other structures. Because of the variability in human anatomy, each of the features is described by fuzzy sets ([82]) that include ranges of normal. Confidence scores are used to quantify how well an image object satisfies these anatomical constraints. The knowledge is used to guide conventional segmentation algorithms and match extracted image regions to anatomical structures.

The key components of the system architecture are the anatomical model, inference engine, and image processing routines, the interaction of which are controlled via a **blackboard** ([83]), as shown in Figure 1.21. (**Appendix 1 gives an introduction to blackboard.**) System components may read data from, and write results to, the blackboard and thereby interact. This allows the components to be designed somewhat independently and to operate with a degree of autonomy.

Labeling the anatomical structures in the image data set involves matching structures in the image to corresponding objects in the model. Matching is done by transforming data from the image and the model into a common, parametric feature-space for comparison. Objects are represented in terms of features such as grey-level range, volume, shape, and position. The image processing

routines provide the means for segmenting the data set into image primitives, which are 3-D sets of contiguous voxels. The model describes objects that should appear in the image (i.e., objects for which a primitive should be able to be extracted) and provides information about the expected features of each object. The inference engine compares features of image primitives with the predictions from the model.
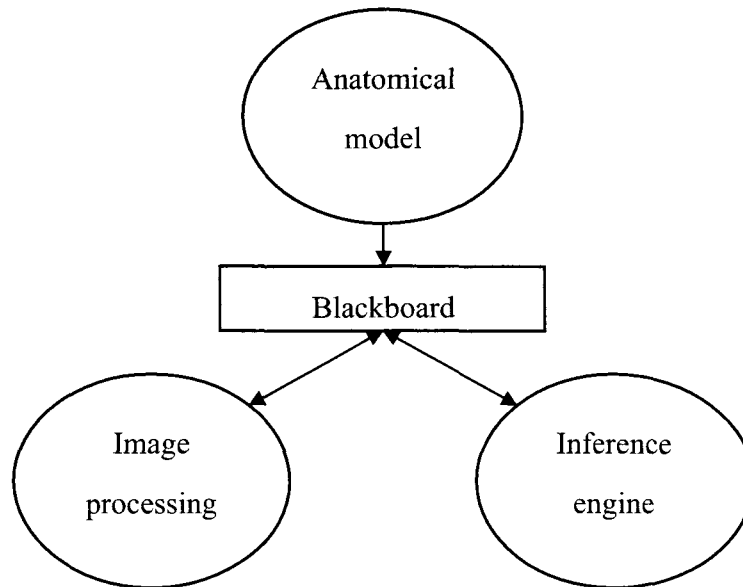
Figure 1.21 System architecture.

The principle of operation is that, for each modeled object, constraints on features are derived and written to the blackboard. Image processing routines write corresponding feature representations of segmented image primitives to the blackboard. The inference engine reads the data from both sources and does the matching. Its conclusions are then also written back to the blackboard and the information can be used to guide further matching. The mapping to feature-space allows the model and image data representations to be independent.

Figure 1.22 shows the knowledge-based segmentation results of chest for a healthy volunteer.
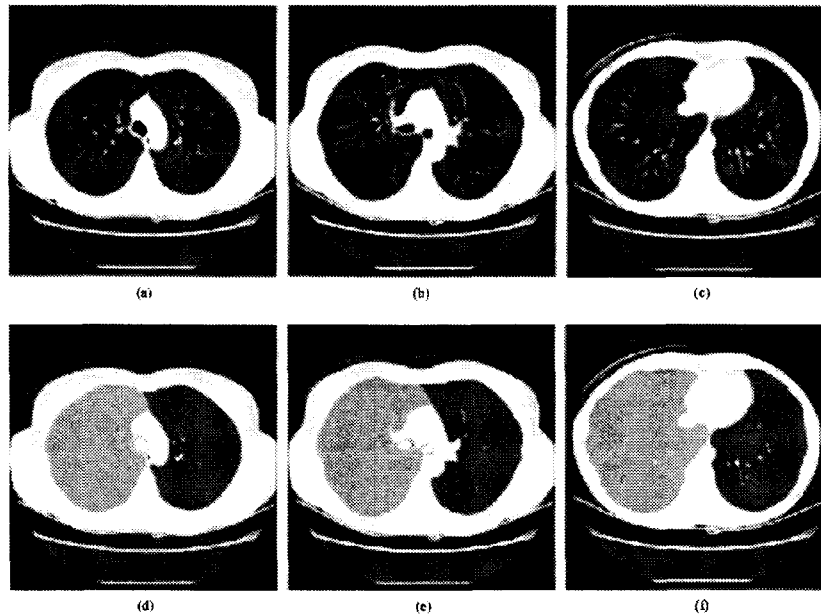
Figure 1.22 (a)-(c) Original CT images from healthy volunteer and (d)-(f) corresponding segmentation results showing central tracheobronchial tree (white) and left (dark grey) and right (light grey) lung parenchyma.

In conclusion, the authors developed an architecture for automatic knowledge-based segmentation of chest CT data that isolates the right and left lungs, central tracheobronchial tree. The use of knowledge offers improvements over unguided segmentation in terms of automation, robustness and the variety of anatomical structures that can be identified. Nevertheless, the frame-based semantic network is built **by human but not computer**. The knowledge is represented using an explicit anatomical model so it is **not extendable for other anatomical structures**. And the authors do not show in which computerized way **all these features are stored**.

1.3 Conclusion

In this chapter, we first introduce the segmentation methods for medical image analysis. Then we present three tissue classification systems.

We can see that a remarkable advantage of the active contour methods using Partial Differential Equation upon the methods using energy minimization is that contours can be split or merged

when the topology of the level set function changes. Therefore, more than one boundary can be detected simultaneously, and several initial contours can be chosen. In addition, for the methods using energy minimization, they can give good results only if the initial contour is close enough to the real edge. However, for active contour methods, the corresponding computational cost is very high because it is directly related to the size of the image to be analyzed. And many parameters have to be calculated according to the nature of the image to be analyzed.

Moreover, contour-based methods look for the discontinuities of image grey levels, while region-based methods concentrate on the homogeneity inside regions. The former is more sensitive to noises than the latter because if high frequency information is missing or unreliable, it makes boundary finding more error-prone compared to region based segmentation. In addition, region-based methods always take into consideration to contextual information so that they are very robust to noises.

Nevertheless, image segmentation is just one step but not the last step in medical image analysis. It just partitions an image into a number of non-overlapped and constituent regions which are homogeneous regarding to some features such as grey level and texture, and it is unable to identify each tissue in a medical image. Thus, following image segmentation, we need to carry out tissue classification in order to give physical sense for each segmented region, namely, we label each region to a specific tissue. From the three tissue classification systems that we present, we can see that they share the following common parts:

– Image segmentation algorithms are mostly based on pixel grey levels such as Fuzzy c-Means.

– A priori knowledge such as anatomical structure of the specific tissues is often provided.

– Rules based on the a priori knowledge for classification are generated.

Thanks to these parts, the obtained results are more accurate than the results obtained by those

pixel grey level-based image segmentation methods. However, all of these systems focus on analysis of specific parts of human body. So they are not normalized and structured, and lack of certainty and precision when being applied in other contexts. Therefore, developing a more generalized automatic tissue classification system becomes a major challenge in medical image analysis.

For the purpose of classification of tissue, we will choose to use a clustering algorithm (namely, Fuzzy C-Means) as base of medical image segmentation in our work, because cluster analysis can offer important domain knowledge, and clusters have better semantic meanings than edges regarding knowledge-based analysis ([14]).

2 Development of a new FCM-based method for medical image segmentation

Fuzzy C-Means (FCM) is a popular clustering technique frequently applied to medical image segmentation. However, FCM is sensitive to noises, which is also a disadvantage of other grey level-based methods. Many methods have been proposed to cope with this problem. Most of them generate a penalty term describing spatial information of neighboring pixels and add it to the standard FCM objective function ([6,13,49-54]). The modified FCM objective functions can then become more spatially smooth for extracting complete objects from images ([55]). In this chapter, we will propose a new FCM-based method for medical image segmentation. We will then compare the performance of our method with the FCM algorithm using Kernel with spatial constraints ([49]) and the FCM algorithm using Markov Random Field via Bayesian theory with spatial constraint ([56]). Also, we will compare our method with an algorithm using Gaussian Mixture Model with spatial constraints ([48]), whose structure is quite different from the FCM-based methods.

2.1   The proposed FCM-based method for image segmentation

In the FCM-based methods ([49,56]) for image segmentation presented in Chapter 1, there are four main drawbacks affecting the results of image segmentation:

- In these modified objective functions, additional complex derivations are often involved. This can lead to inaccurate results.

- In the definition of penalty term, the existing methods often select a fixed 3×3 observation window centered on each pixel of interest for incorporating the related spatial information of neighboring pixels. In practice, the size of window should be adapted to the real situation of neighboring pixels. The available size can be $3 \times 3, 5 \times 5, 7 \times 7$, etc.

- The importance coefficient of the penalty term in the FCM objective function is not

systematically defined. This coefficient controls the intensity of penalty and affects the results of image segmentation. It should be optimized so that both the advantages of FCM and the penalty term can be taken into account in the objective function.

- In the objective function of FCM, each pixel is generally described by the related grey level only and other important information such as relations with neighboring pixels and texture are not taken into account.

We propose a new FCM-based image segmentation method to solve the previous shortcomings, it includes three novelties:

- We use the standard FCM objective function without adding any penalty term. This can effectively reduce the difficulties related to the selection of coefficient of penalty term and complex derivations.

- Moreover, we use a **ten**-dimensional feature vector to describe each pixel. This vector includes grey level and both local and global spatial information on neighboring pixels. **An improvement on this vector is made to** reduce the algorithm complexity of FCM and more effectively extract the spatial information of objects on the image.

- Also, we propose an algorithm to define the window size in a dynamical way for extracting appropriate global spatial information from images.

Next, we first introduce the method to define the dynamical window size for extracting appropriate global spatial information for each central pixel. Then we explain how to generate the n-dimensional feature vector to describe each pixel.

2.1.1 Method for dynamically selecting the size of observation window for each pixel

For each pixel of the image, we define an observation window centered on it and then calculate the mean value of all Euclidean distances of grey levels between the central pixel and its neighboring

pixels inside this window. On the image, we move this window from left to right and from top to bottom in order to extract spatial information of objects. The size of this window can be $3 \times 3, 5 \times 5, 7 \times 7$. It is formally expressed by:

$$M = \frac{\sum_{i=1}^{N} \left(\left\| G_{(0)} - G_{(i)} \right\| \right)}{N} \qquad (2.1)$$

where

M is the mean value of the Euclidean distances,

N the number of neighboring pixels inside the window,

$G_{(0)}$ the grey level of the central pixel,

$G_{(i)}$ the grey level of the ith neighbor of the central pixel (i=1,2,...,N).

By calculating the mean values of the Euclidean distances for different sized windows, we select the window corresponding to the smallest averaged Euclidean distance. The uniformity of grey levels in this window is the highest. Obviously, when moving the window on the image, the size of window can vary with the distribution of grey levels centered on the central pixel. In this way, each object, generally considered as a group of pixels having similar grey levels, can be better extracted.

In practice, only the 3×3 window, 5×5 window, and 7×7 window are considered, because these windows are sufficient to extract spatial information. The corresponding values of N are 8, 24 and 48 respectively.

2.1.2 Generation of features for each pixel

For describing each pixel, we generate the following ten-dimensional feature vector:

$$Y_1 = \left(G_{(0)}, G_{(1)}, ... G_{(8)}, M \right) \qquad (2.2)$$

where:

$G_{(0)}$ is the grey level of the central pixel,

$G_{(1)},.....G_{(8)}$ the grey levels of its eight neighbors in a 3×3 window. They represent the local distribution of grey levels around the central pixel.

M is the smallest mean value of Euclidean distances defined in Section 2.1.1.

$(G_{(1)},...,G_{(8)})$ represents the local spatial information in the nearest neighboring area of the central pixel. This information is more detailed than any other observation windows. (M) represents the spatial information in a larger and more adaptive neighboring area of the central pixel. Thus, the feature vector includes not only local but also general spatial information around the central pixel.

Next, in order to reduce the algorithm complexity of FCM and extract more relevant local and global information on image pixels, we propose another feature vector:

$$Y_2 = \left(G_{(0)}, M_1, M_2, SD, M\right) \tag{2.3}$$

where:

$G_{(0)}$ is the grey level of the central pixel,

M the smallest mean value of Euclidean distances defined in Section 2.1.1.

M_1, M_2, SD the mean, the median and the standard deviation of all pixels in an observation window whose size is determined by M.

Thus, we obtain only 5 dimensions in Y_2. Compared to Y_1 with 10 dimensions, this new feature vector greatly reduces the algorithm complexity of FCM and makes more compact local and global spatial information on the central pixel. In general, the statistical distribution of grey levels (mean, median and standard deviation) in an adaptive window is more representative and more significant than the grey levels of the eight neighbors of the central pixel. So the spatial

information of objects on the image can be more effectively taken into account in this feature vector.

The FCM algorithm by using the feature vector Y_1 is nominated as 'Multiple Features FCM' (MFFCM), and the FCM algorithm by using the feature vector Y_2 as 'Improved Multiple Features FCM' (IMFFCM). For a window 3×3, the FCM algorithm is represented by IMFFCM_3. In the same way, we have IMFFCM_5, IMFFCM_7 for other sizes of windows. When the size of window is dynamically selected, it is represented by IMFFCM_DS.

IMFFCM_DS

Input: c, the number of cluster; m, the coefficient controlling the fuzzy degree; ε, the value for convergence; u_{ij}^0, initial memberships.

Output: the partition matrix U.

Calculate the size of observation window for each pixel by Eq.(2.1).

Generate feature vector for describing each pixel based on the observation window obtained in last step Eq.(2.3).

t=0;

Repeat

> Update cluster centers $v_i^{(t)}$ by Eq.(1.35).
>
> Update membership degrees $u_{ij}^{(t)}$ using Eq.(1.34).
>
> t=t+1;

Until $\left\| u_{ij}^{(t+1)} - u_{ij}^{(t)} \right\| < \varepsilon$

2.2   Comparison of image segmentation results between different methods and analysis

In this section, we apply the proposed algorithm to segment a number of synthetic and real images and two medical images. The parameters of the algorithm are set as follows: $m = 2$, $\varepsilon = 0.001$.

First, we apply the proposed algorithm to a synthetic image and compare its performance with different versions of modified FCM methods: FCM_S1, FCM_S2, KFCM_S1 and KFCM_S2 in ([49]), NGFCM in ([56]), GMM_S$_1$ and GMM_S$_2$ in ([48]). The corresponding results are shown in Figure 2.1 and Figure 2.2.

The synthetic image is composed of 200×200 pixels, including four classes whose grey levels are centered on 10, 80, 150 and 220 respectively (see Figure 2.1(a) and Figure 2.2(a)). Each class is corrupted by a 'Gaussian' noise in Figure 2.1 and a 'Salt & Pepper' noise in Figure 2.2. Because in MRI images, when the Signal to Noise Ratio (SNR) is large, which signifies the tissues, its distribution is approximately the Gaussian distribution. And when only noise is present, which signifies the air, its distribution is approximately the Rayleigh distribution. (**Appendix 2 gives an introduction to MRI disribution**). We add a 'Gaussian' noise to synthetic image and MRI images to test the performance of our method. We also add a 'Salt & Pepper' noise to show the robustness of our method. From Figure 2.1 and Figure 2.2, we can see that only the result of dynamically selected window size leads to best segmentation effects.

(a)

(b)

(c)

(d)

(e)

(f)

(g)

(h)

(i)

(j)

(k)

(l)   (m)   (n)
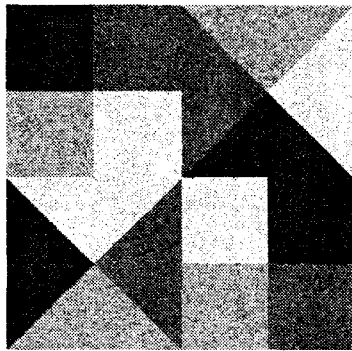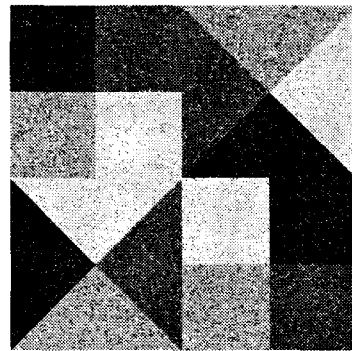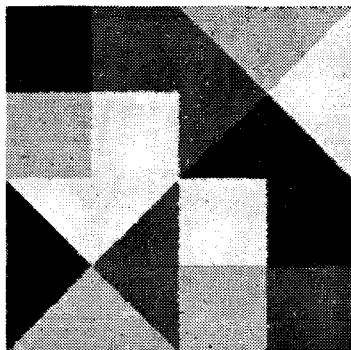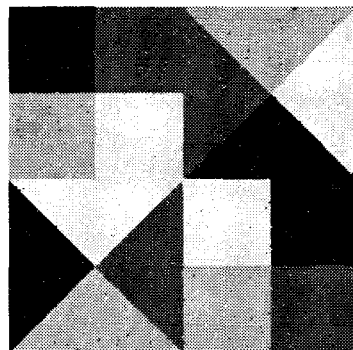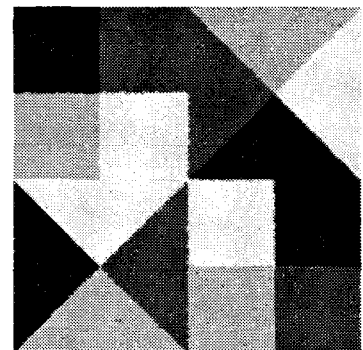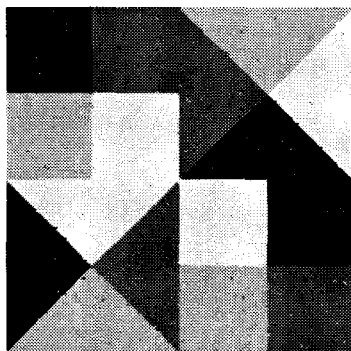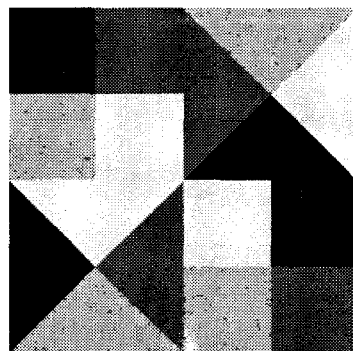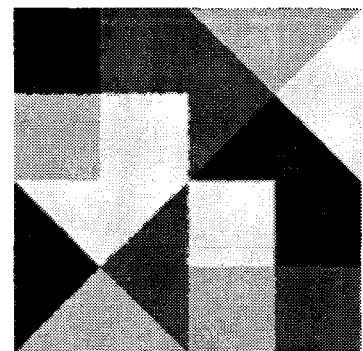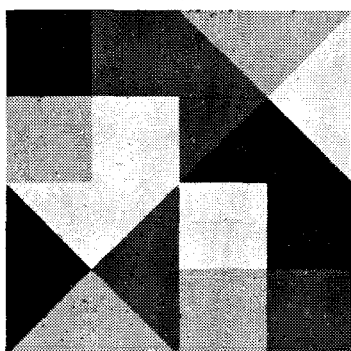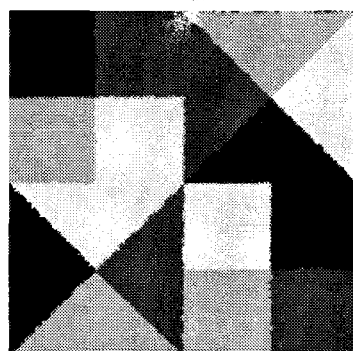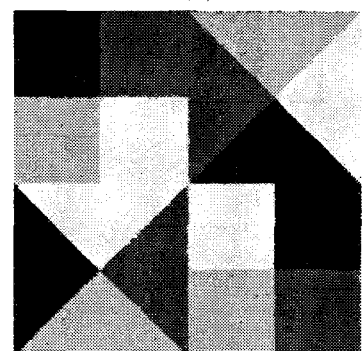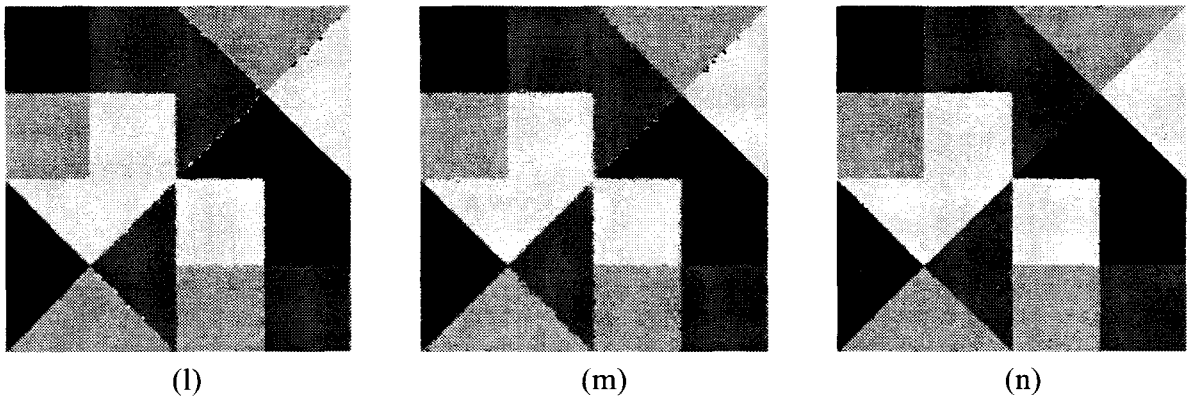
Figure 2.1 Comparison between different segmented images.

(a). original image with 5% 'Gaussian' noise. (b). result by FCM. (c). result by FCM_S1. (d). result by FCM_S2. (e). result by KFCM_S1. (f). result by KFCM_S2. (g). result by NGFCM, (h). result by GMM_S1, (i). result by GMM_S2. (j). result by MFFCM. (k). result by IMFFCM_3. (l). result by IMFFCM_5. (m). result by IMFFCM_7. (n). result by IMFFCM_DS.

(a)   (b)

(c)   (d)   (e)
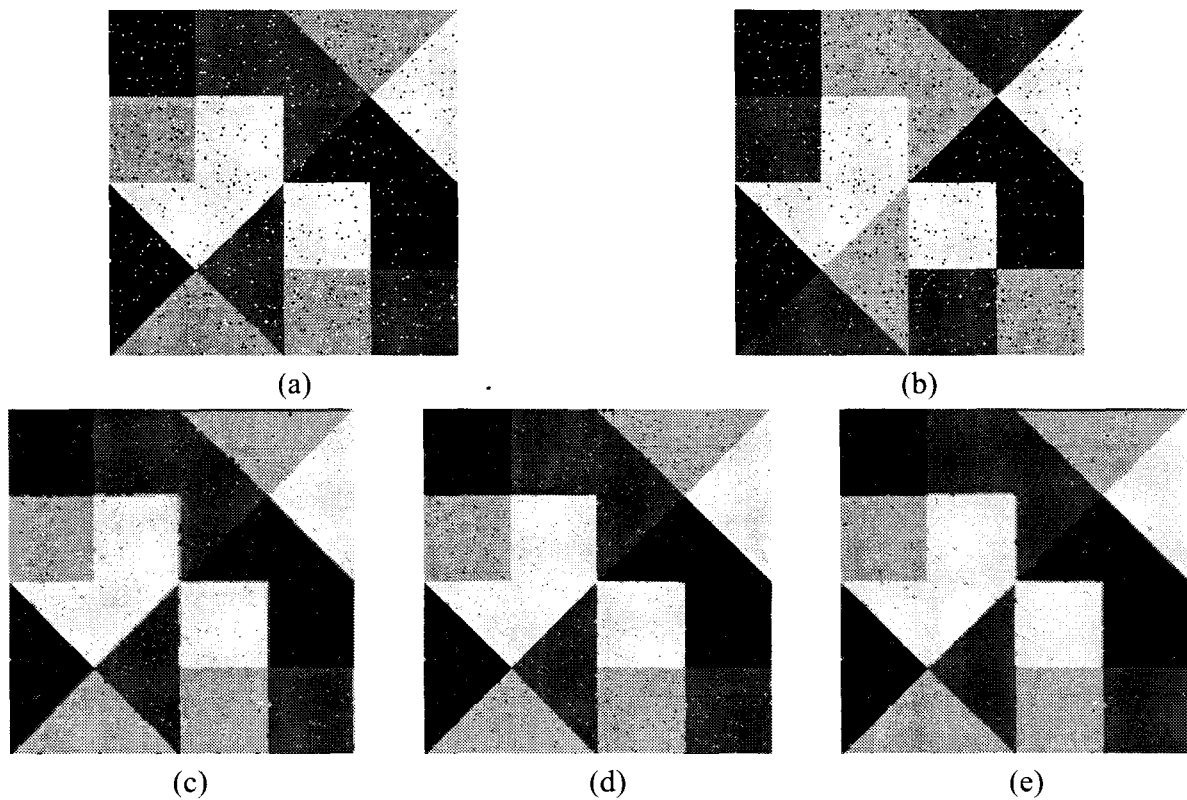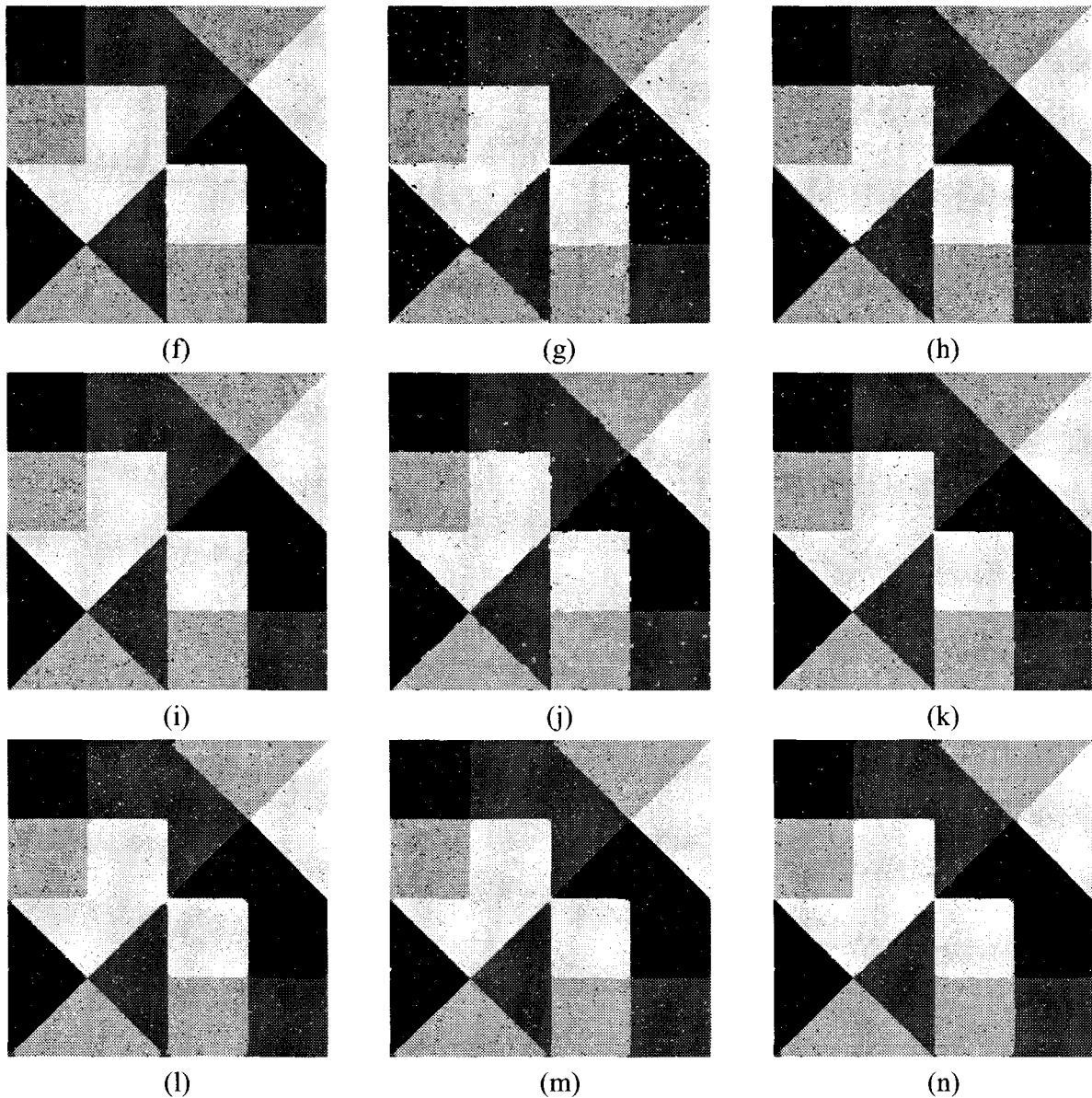
Figure 2.2 Comparison between different segmented images.

(a). original image with 2% 'Salt & Pepper' noise. (b). result by FCM. (c). result by FCM_S1. (d). result by FCM_S2. (e). result by KFCM_S1. (f). result by KFCM_S2. (g). result by NGFCM, (h). result by GMM_S1, (i). result by GMM_S2. (j). result by MFFCM. (k). result by IMFFCM_3. (l). result by IMFFCM_5. (m). result by IMFFCM_7. (n). result by IMFFCM_DS.

TABLE 2.1 and TABLE 2.2 compare the segmentation accuracy (SA) between classical FCM, FCM_S1, FCM_S2, KFCM_S1, KFCM_S2, NGFCM, GMM_S1, GMM_S2 and the proposed method. The original image is corrupted by a 'Gaussian' noise (TABLE 2.1) and a 'Salt & Pepper'

noise (TABLE 2.2) respectively. The segmentation accuracy is defined as the ratio of the number

of correctly classified pixels to the total number of pixels ([84]). The results of TABLE 2.1 and

TABLE 2.2 show that the proposed method has better performance in segmentation accuracy than

classical FCM, FCM_S1, FCM_S2, KFCM_S1, KFCM_S2, NGFCM, GMM_S1, GMM_S2, and

it is more robust to image noises.

TABLE 2.1 Comparison of segmentation accuracy on the synthetic image corrupted by 5% 'Gaussian' noise.
(a). classical FCM, (b). FCM_S1, (c).FCM_S2, (d). KFCM_S1, (e). KFCM_S2, (f). NGFCM, (g). GMM_S1, (h). GMM_S2, (i). MFFCM and (j). **IMFFCM_DS**.

	Segmentation methods									
	a	b	c	d	e	f	g	h	i	j
SA	90%	97.1%	98%	99.2%	99.3%	99.46%	99.4%	99.48%	97.5%	**99.55%**

TABLE 2.2 Comparison of segmentation accuracy on the synthetic image corrupted by 2% 'Salt & Pepper' noise.
(a). classical FCM, (b). FCM_S1, (c).FCM_S2, (d). KFCM_S1, (e). KFCM_S2, (f). NGFCM, (g). GMM_S1, (h). GMM_S2, (i). MFFCM and (j). **IMFFCM_DS**.

	Segmentation methods									
	a	b	c	d	e	f	g	h	i	j
SA	98.4%	98%	98.6%	98.9%	99.6%	99.4%	99%	99.25%	99.4%	**99.7%**

TABLE 2.3 Comparison of image segmentation accuracy under 'Gaussian' noise between classical FCM, MFFCM, and IMFFCM with different window sizes.
(a) classical FCM, (b) MFFCM, (c) IMFFCM_3, (d)IMFFCM_5, (e) IMFFCM_7, (f) **IMFFCM_DS**.

	Accuracy varying with different rates of 'Gaussian' noise						
	3%	5%	8%	15%	25%	40%	55%
a	91%	90.0%	88.7%	7.1%	82.5%	66.3%	48.2%
b	97.9%	97.5%	97%	96.3%	95.3%	78.0%	60.3%
c	99.6%	99.47%	99.2%	98.7%	95.8%	66.4%	57.1%
d	99.2%	99.16%	99.05%	98.8%	96.4%	70.8%	64.3%
e	98.9%	98.5%	98.2%	97.7%	96.3%	73.2%	68.6%
f	**99.63%**	**99.55%**	**99.3%**	**99.5%**	**96.8%**	**79.8%**	**70.8%**

TABLE 2.3 and TABLE 2.4 compare the performance of classical FCM, our FCM-based method

with three fixed sized windows and the dynamically selected window size defined in Section 2.1.1.

The original image is corrupted by a 'Gaussian' noise (TABLE 2.3) and a 'Salt & Pepper' noise (TABLE 2.4) respectively. In TABLE 2.3, we see that for all levels of image noises, the dynamically selected window always shows the best segmentation result related to fixed window sizes. It proves that we need to optimize the window size for extracting spatial information. We can also see that in low noise levels, 3×3 windows always show the best segmentation result while in high noise levels, 7×7 windows are more efficient. This is because we need to incorporate more contextual information for maintaining high accurate segmentation results when the noise level is increased. In TABLE 2.4 we can also see that the algorithm with dynamically selected window size leads to the highest segmentation accuracy. From TABLE 2.5, we can see that with the increase of noise level, the number of selected 3×3 windows decreases and the number of selected 7×7 windows increases. It proves again that we need to incorporate more contextual information with the increase of noise level.

TABLE 2.4 Comparison of image segmentation accuracy under 'Salt & Pepper' noise between classical FCM, MFFCM, and IMFFCM with different window sizes.
(a) classical FCM, (b) MFFCM, (c) IMFFCM_3, (d)IMFFCM_5, (e) IMFFCM_7, (f) **IMFFCM_DS**.

Window size	accuracy varying with different rates of 'Salt & Pepper' noise			
	2%	5%	8%	15%
a	98.4%	97.7%	96.8%	93.2%
b	99.4%	97.9%	96.1%	92.3%
c	99.4%	98.8%	97.6%	93.4%
d	99.2%	98.9%	98.1%	94.2%
e	99.1%	98.8%	98.3%	94.7%
f	**99.7%**	**99%**	**98.5%**	**94.8%**

TABLE 2.5 Numbers of dynamically selected windows with different sizes under 'Gaussian' noise for the above synthetic image.
(a) IMFFCM_3, (b)IMFFCM_5, (c) IMFFCM_7,

	Numbers of selected windows varying with 'Gaussian' noise						
	3%	5%	8%	15%	25%	40%	55%
a	12458	12050	11595	11104	6979	5187	3937
b	2924	2942	3064	3467	4780	5279	5707
c	24618	25008	25341	25429	28241	29534	30356

Figure 2.3 compares the segmentation results on a real image ([85]) between FCM, FCM_S1, FCM_S2, KFCM_S1, KFCM_S2, NGFCM, GMM_S1, GMM_S2, MFFCM and our FCM-based method with different window sizes. Figure 2.3(a) is the original image corrupted by 5% 'Gaussian' noise. We can see that the original image is badly segmented by the standard FCM method and FCM_S1, FCM_S2. However, in Figure 2.3(n), the segmentation result is the best because more details inside the coin can be extracted. In practice, the method of dynamically selected window size gives more complete spatial information on image pixels.

(a)

(b)

(c)

(d)

(e)

(f)

(g)

(h)
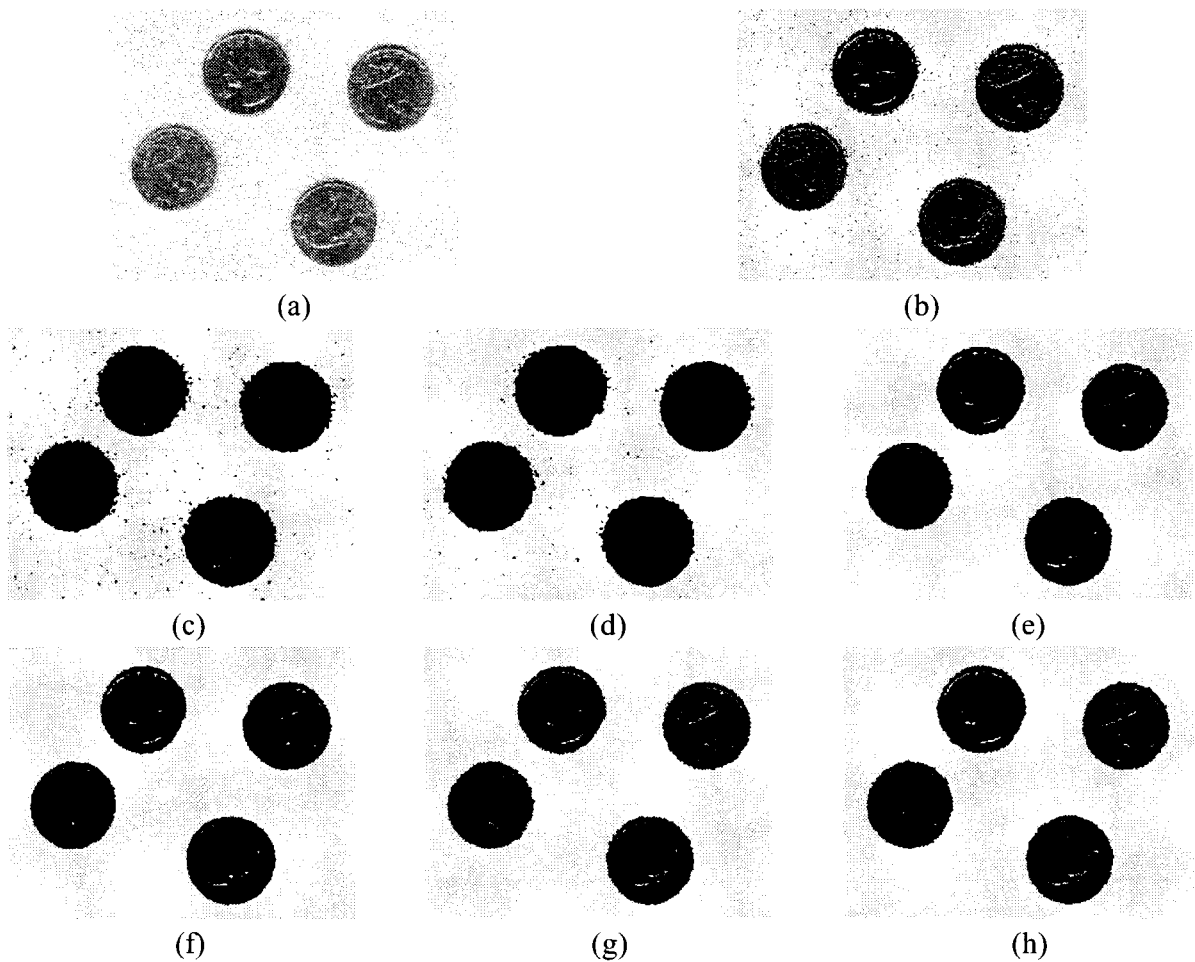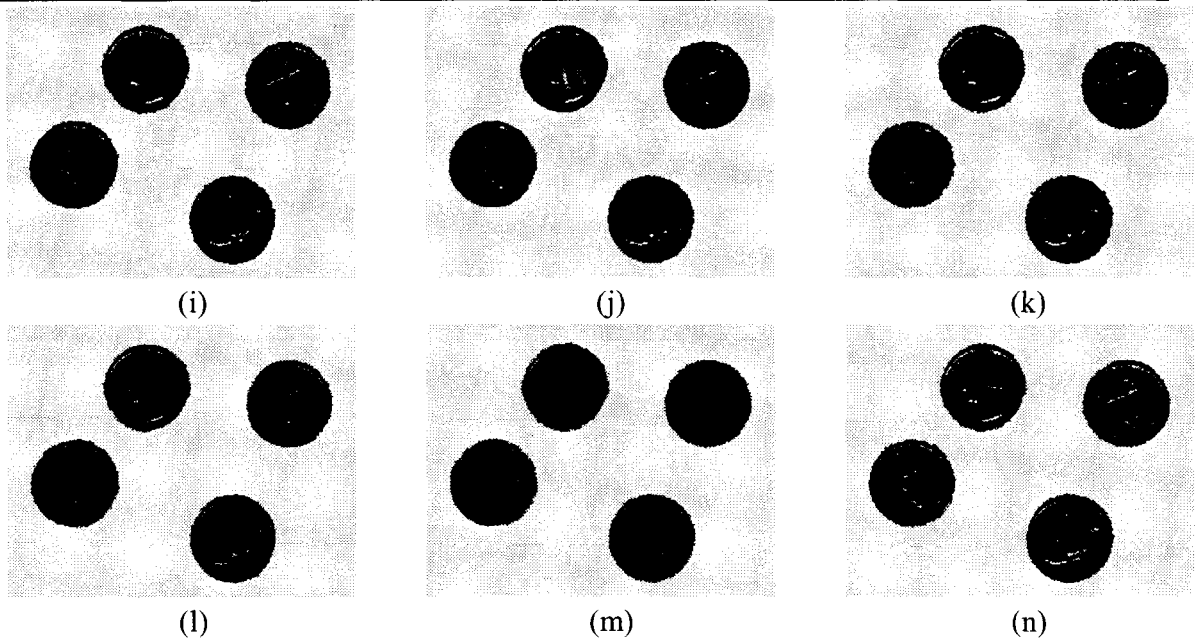
Figure 2.3 Comparison between different segmented images.

(a). original image with 5% 'Gaussian' noise. (b). result by FCM. (c). result by FCM_S1. (d). result by FCM_S2. (e). result by KFCM_S1. (f). result by KFCM_S2. (g). NGFCM, (h). GMM_S1, (i). GMM_S2. (j). result by MFFCM. (k). result by IMFFCM_3. (l). result by IMFFCM_5. (m). result by IMFFCM_7. (n). result by IMFFCM_DS.
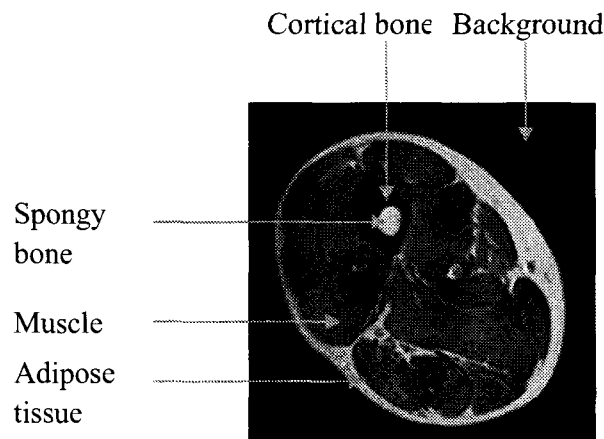
Figure 2.4 A MRI image of thigh

After we show the performance of our method on synthetic and real images, we will show the performance of our method on MRI image. Figure 2.4 is a T1-weighted MRI image of thigh with a thickness of 10 mm, and the coding is 12 bits. Thigh is composed of many tissues ([86]). However, for simplicity, only four following tissues are considered ([87]): muscle, adipose tissue,

cortical bone, and spongy bone. Then, we apply the segmentation procedure for obtaining five classes, i.e. the four tissues and background. The result of segmentation (Figure 2.5) obtained by our FCM-based method with dynamically selected window is rather poor because there is an overlap of grey levels between background and cortical bone, as well as adipose tissue and spongy bone, as shown in Figure 2.6. Thus, we segment the image into three classes: background and cortical bone, adipose tissue and spongy bone, and muscle.
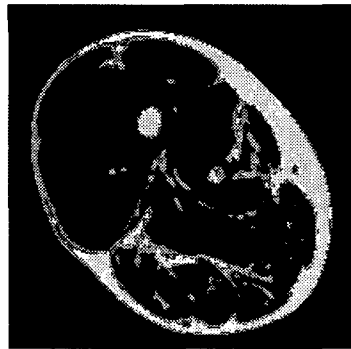
Figure 2.5 Segmentation result of MRI image of thigh.
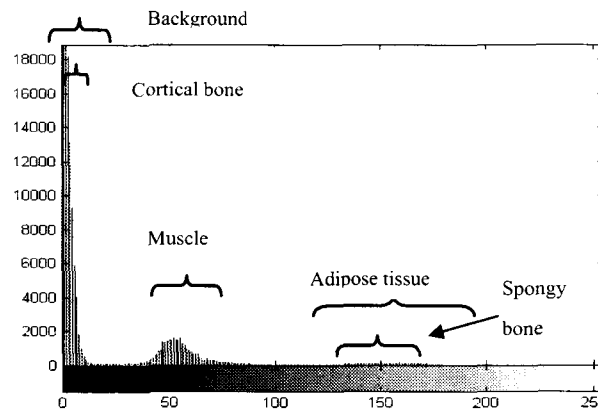
Figure 2.6 Histogram of a MRI image of thigh.

Figure 2.7, Figure 2.8 and Figure 2.9 compare the segmentation results between the image without noise and that with 3% and 8% 'Gaussian' noise. In Figure 2.7, the original image and the corresponding reference segmentation result provided by a medical expert in the CHRU (France) are given in Figure 2.7(a) and Figure 2.7(b) respectively. We can see that in Figure 2.7, Figure 2.8 and Figure 2.9 the segmentation performance of the method of dynamically selected window outperforms the others.
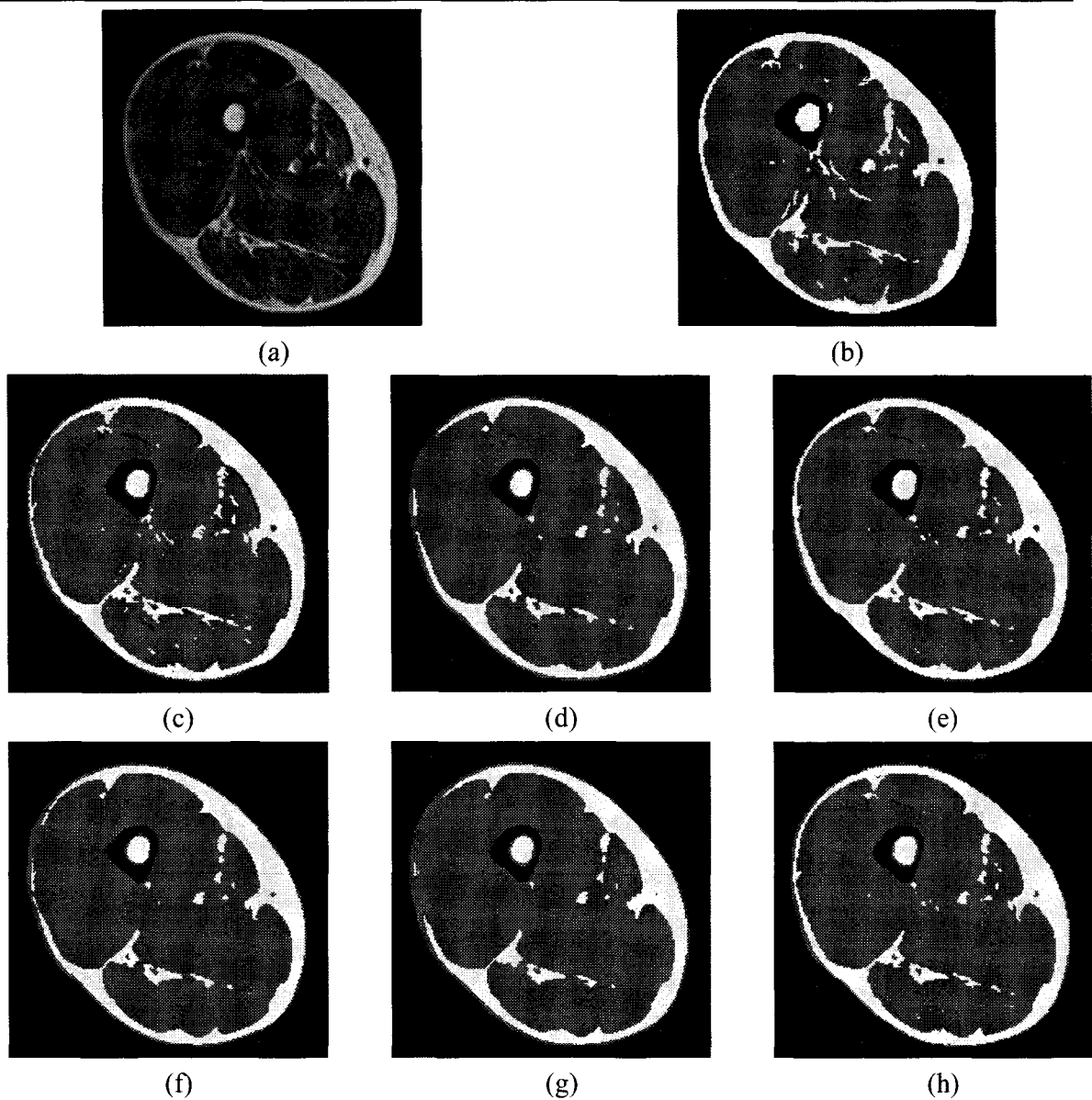
Figure 2.7 Segmentation results for one image of thigh.

(a) original image. (b) expert's segmentation result. (c) result by FCM. (d) result by MFFCM. (e) result by IMFFCM_3.

(f) result by IMFFCM_5. (g) result by IMFFCM_7. (h). result by IMFFCM_DS.
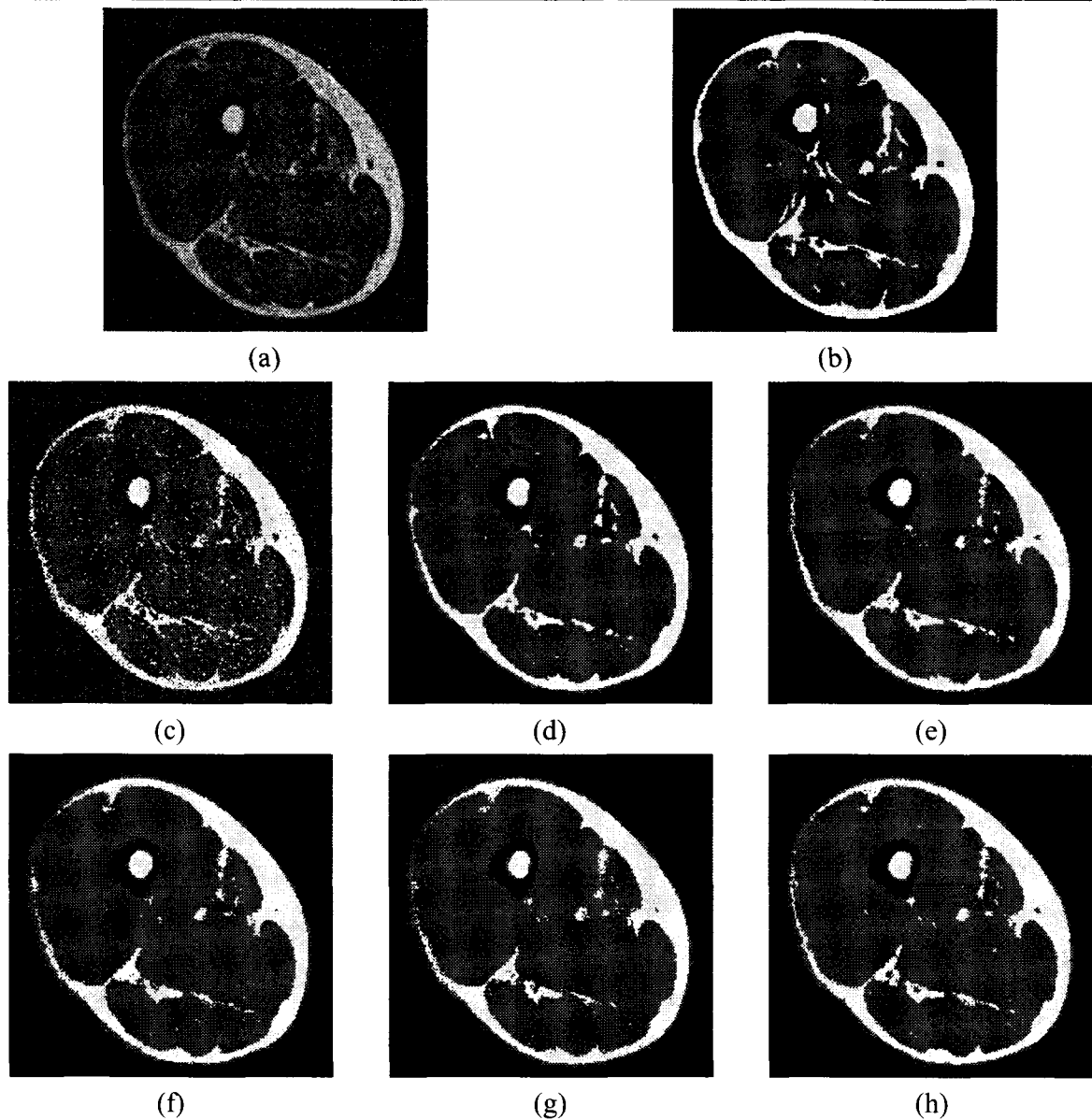
Figure 2.8 Segmentation results for one image of thigh.

(a) original image with artificially added 3% 'Gaussian' noise. (b) expert's segmentation result. (c) result by FCM. (d) result by MFFCM. (e) result by IMFFCM_3. (f) result by IMFFCM_5. (g) result by IMFFCM_7. (h). result by IMFFCM_DS.
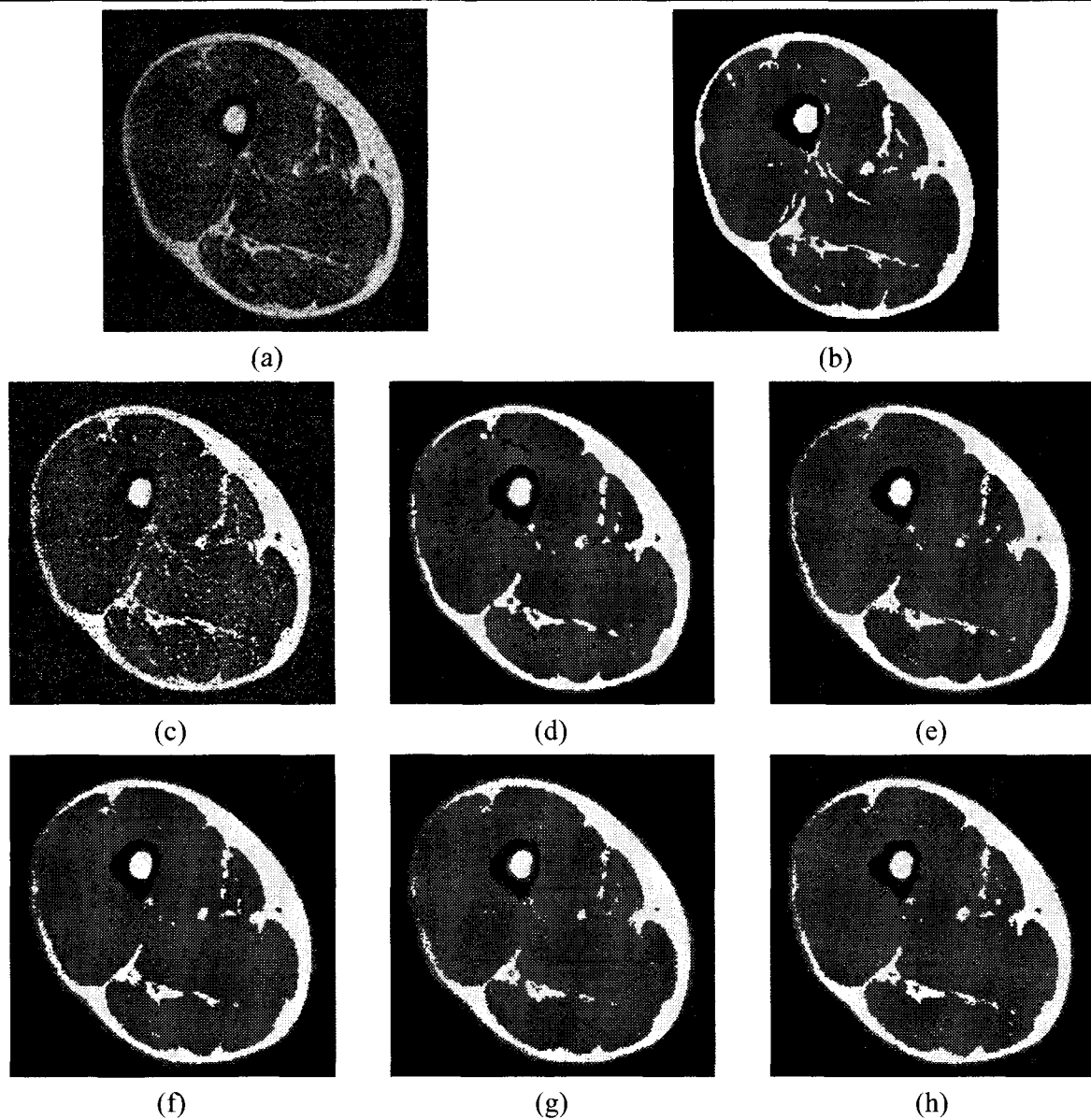
Figure 2.9 Segmentation results for one image of thigh.

(a) original image with artificially added 8% 'Gaussian' noise. (b) expert's segmentation result. (c) result by FCM. (d) result by MFFCM. (e) result by IMFFCM_3. (f) result by IMFFCM_5. (g) result by IMFFCM_7. (h). result by IMFFCM_DS.

TABLE 2.6-2.8 quantitatively compare the classification results obtained from our FCM-based method with different window sizes and the reference classification results, for one image without noise, one with 3% 'Gaussian' noise, and one with 8% 'Gaussian' noise, which are shown in Figure 2.7-2.9. The comparison criterion (cc) is given as follows.

$$cc = \frac{A_{ij} \cap A_{ref\,j}}{A_{ij} \cup A_{ref\,j}}$$

(2.4)

where A_{ij} represents the set of pixels belonging to the jth class obtained by the ith method, and $A_{ref\,j}$ the set of pixels belonging to jth class in the reference segmented image.

In TABLE 2.6, we see that the performance of IMFFCM_DS on cortical bone and background is best among all methods. However, we see that the performance of IMFFCM_3 on adipose tissue and spongy bone, as well as muscle is better than IMFFCM_DS, and outperforms all other methods. In practice, if the original image which is not corrupted by 'Gaussian' noise is relatively homogeneous, a 3×3 window is good enough to obtain appropriate spatial information for segmentation. If we use IMFFCM_DS in this case, spatial information will be over extracted and result in incorrect segmentation.

From TABLE 2.7 and 2.8, we can see that the method of dynamically selected window size shows the best segmentation performance of all the methods. In addition, with the increase of noise level, the classification rate is generally stable, which means that our method is very robust to noises. Moreover, in low noise level, the performance of our method with 3×3 window is the best among those three window sizes. When noise level increases, the one with 5×5 window is the best. This also explains and confirms the fact that with the increase of noise level, spatial information in a larger and adaptive neighboring area is needed.

TABLE 2.6 Quantitative comparison of segmentation results for one image of thigh by classical FCM and our FCM-based method with different window sizes.
(a) MFFCM, (b) IMFFCM_3, (c) IMFFCM_5, (d) IMFFCM_7, (e) IMFFCM_DS.

	Cortical bone & background	Adipose tissue & spongy bone	Muscle
FCM	95.73%	81.43%	90.62%
MFFCM	95.55%	77.54%	89.54%
IMFFCM _3	95.75%	**82.77%**	**92.05%**
IMFFCM _5	95.73%	78.27%	89.94%
IMFFCM _7	95.2%	76.72%	88.9%
IMFFCM_DS	**95.87%**	81.98%	90.76%

TABLE 2.7 Quantitative comparison of segmentation results for one image of thigh corrupted by 3% 'Gaussian' noise by classical FCM and our FCM-based method with different window sizes.
(a) MFFCM, (b) IMFFCM_3, (c) IMFFCM_5, (d) IMFFCM_7, (e) IMFFCM_DS.

	Cortical bone & background	Adipose tissue & spongy bone	Muscle
FCM	70.02%	69.08%	60.84%
MFFCM	92.2%	76.39%	86.34%
IMFFCM _3	94.34%	76.88%	87.94%
IMFFCM _5	94.18%	75.77%	87.74%
IMFFCM _7	94.24%	75.14%	87.77%
IMFFCM_DS	**95.04%**	**77.98%**	**88.83%**

TABLE 2.8 Quantitative comparison of segmentation results for one image of thigh corrupted by 8% 'Gaussian' noise by classical FCM and our FCM-based method with different window sizes.
(a) MFFCM, (b) IMFFCM_3, (c) IMFFCM_5, (d) IMFFCM _7, (e) IMFFCM_DS.

	Cortical bone & background	Adipose tissue & spongy bone	Muscle
FCM	69.26%	69.02%	59.23%
MFFCM	93.42%	77.25%	87.26%
IMFFCM _3	93.05%	75.76%	86.78%
IMFFCM _5	94.12%	76.64%	88.08%
IMFFCM _7	93.7%	74.24%	87%
IMFFCM_DS	**94.31%**	**77.56%**	**88.38%**

Figure 2.10 and Figure 2.11 compare the segmentation results for one image with 5% 'Gaussian'

noise and one image with 3% 'Gaussian' noise when applying classical FCM, FCM_S1, FCM_S2, KFCM_S1, KFCM_S2, NGFCM, GMM_S1, GMM_S2, MFFCM and our FCM-based method with dynamically selected window. TABLE 2.9 and TABLE 2.10 show the corresponding quantitative comparison results. We can see that our method leads to the best segmentation results. As this method incorporates both local and global spatial information of neighboring pixels, it is more robust to noises.

(a)　　　　　　　　(b)　　　　　　　　(c)

(d)　　　　　　　　(e)　　　　　　　　(f)

(g)　　　　　　　　(h)　　　　　　　　(i)
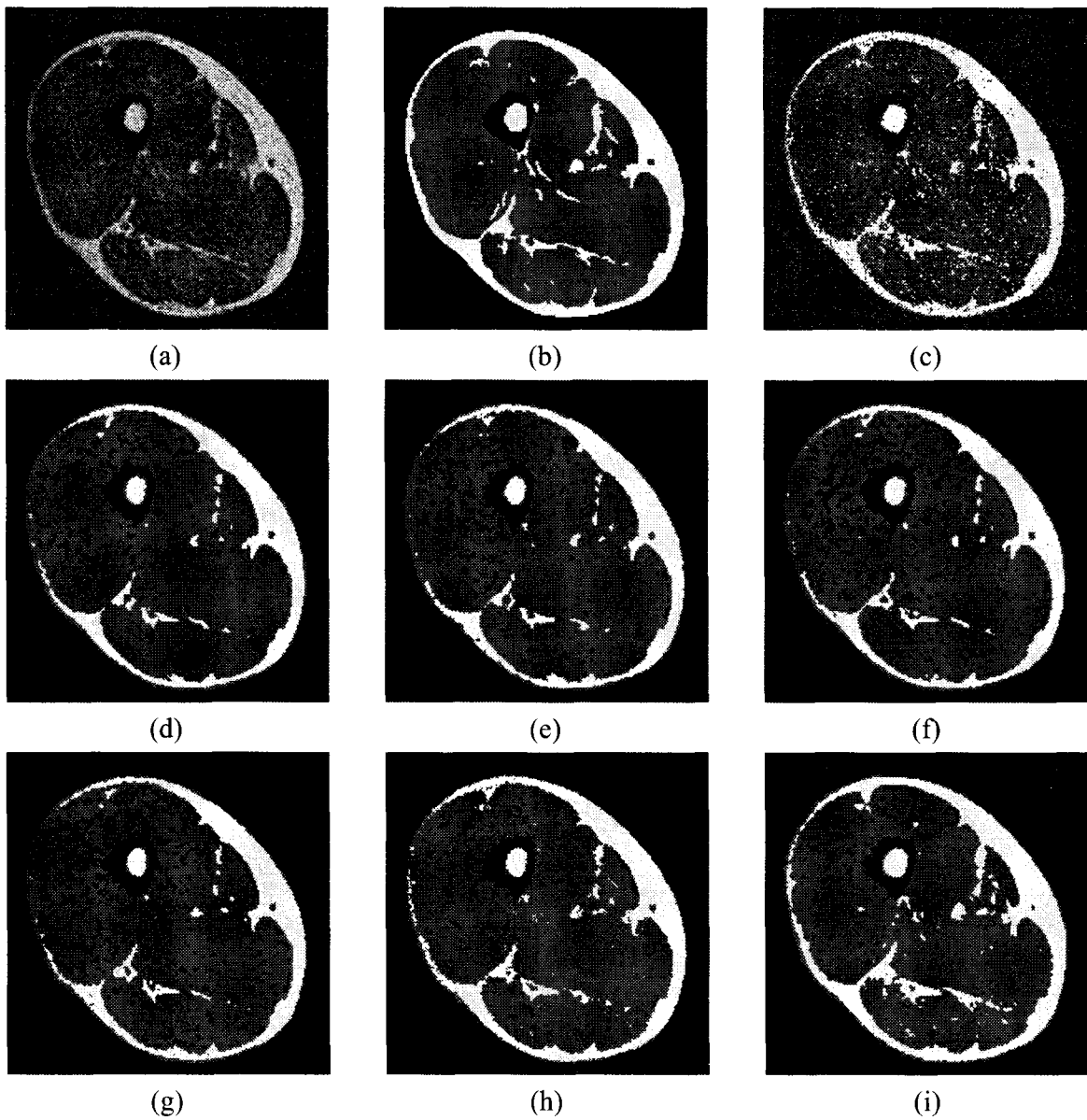
(j)　　　　　　　　(k)　　　　　　　　(l)

Figure 2.10 Segmentation results for one image of thigh with artificially added noise.
(a). original image with 5% 'Gaussian' noise. (b) expert's segmentation result. (c). result by FCM. (d). result by
FCM_S1. (e). result by FCM_S2. (f). result by KFCM_S1. (g). result by KFCM_S2. (h). NGFCM, (i). GMM_S1, (j).
GMM_S2. (k). result by MFFCM. (l). result by IMFFCM_DS.

(a)　　　　　　　　(b)　　　　　　　　(c)

(d)　　　　　　　　(e)　　　　　　　　(f)

| (g) | (h) | (i) |

| (h) | (j) | (l) |
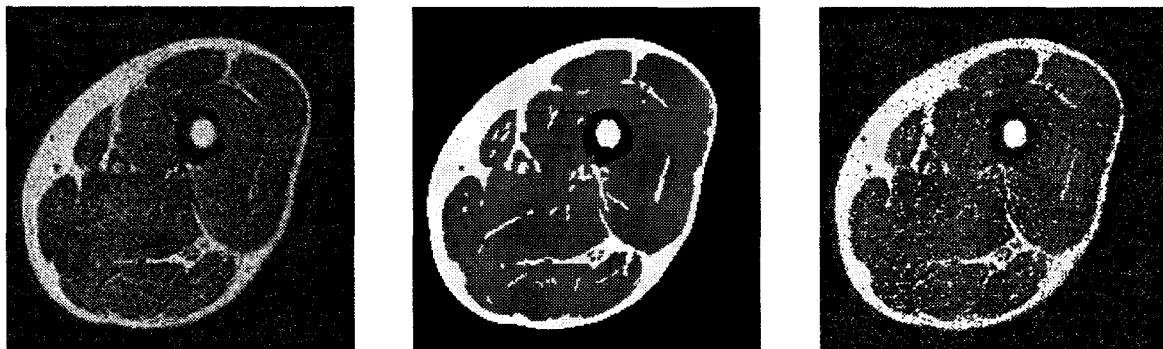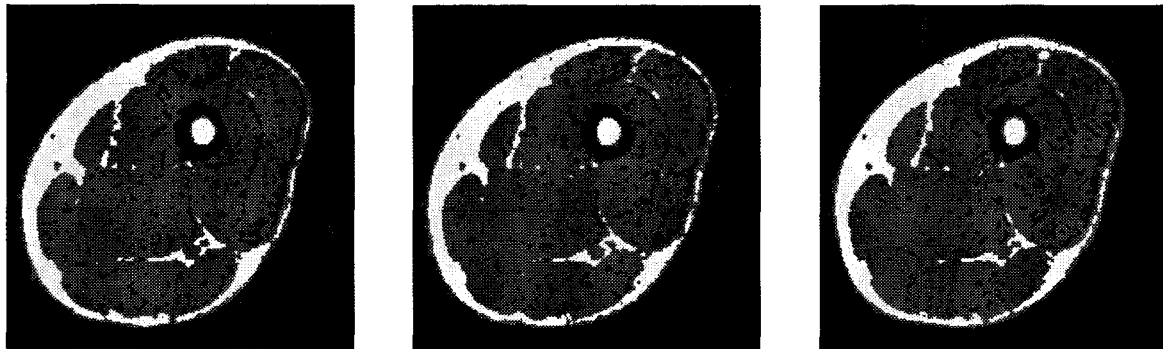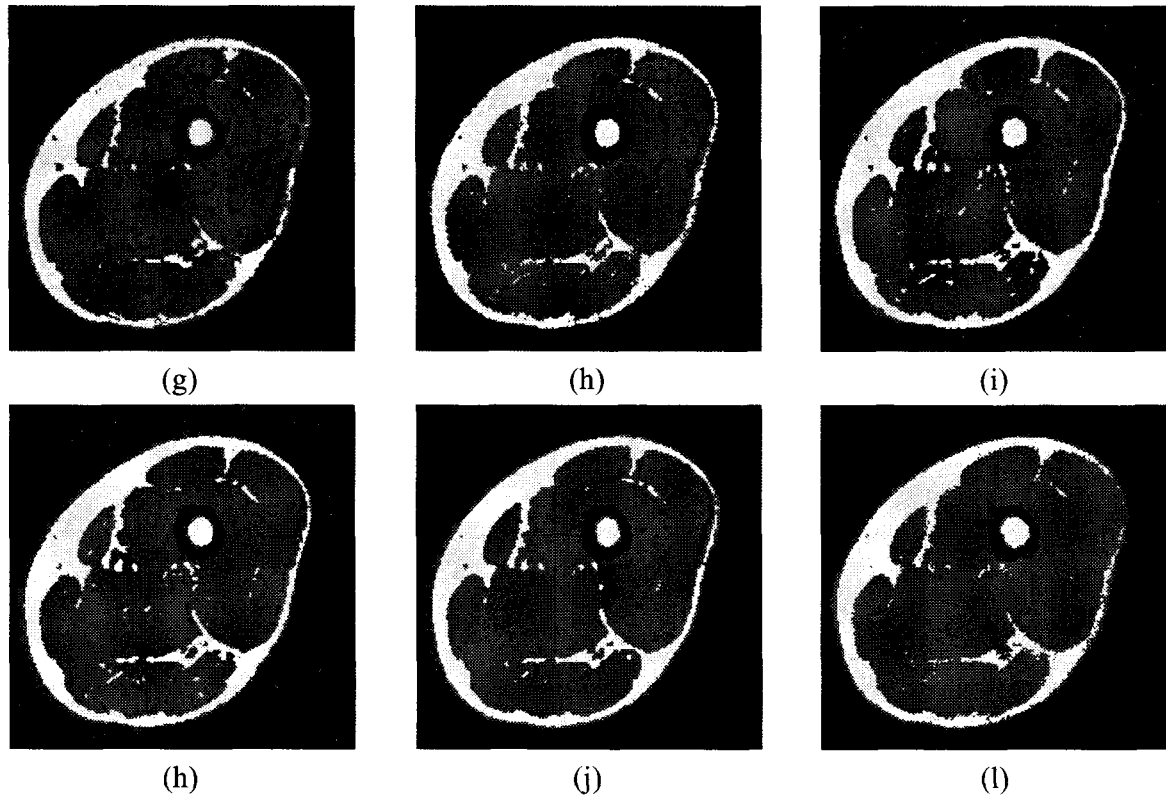
Figure 2.11 Segmentation results for one image of thigh with artificially added noise.

(a). original image with 3% 'Gaussian' noise. (b) expert's segmentation result. (c). result by FCM. (d). result by FCM_S1. (e). result by FCM_S2. (f). result by KFCM_S1. (g). result by KFCM_S2. (h). NGFCM, (i). GMM_S1, (j). GMM_S2. (k). result by MFFCM. (l). result by IMFFCM_DS.

TABLE 2.9 Quantitative comparison of segmentation results for one image of thigh corrupted by 5% 'Gaussian' noise in Figure 2.10.

	Cortical bone & background	Adipose tissue & spongy bone	Muscle
FCM	69.32%	69.05%	59.54%
FCM_S1	87.3%	69.93%	79.05%
FCM_S2	87.63%	69.57%	79.26%
KFCM_S1	85.76%	69.38%	77.16%
KFCM_S2	82.49%	68.89%	72.71%
NGFCM	92.53%	76.84%	86.15%
GMM_S1	92.71%	77.78%	87%
GMM_S2	93.45%	77.31%	87.06%
MFFCM	92.84%	76.91%	86.87%
IMFFCM_DS	**94.59%**	**77.88%**	**88.45%**

TABLE 2.10 Quantitative comparison of segmentation results for one image of thigh corrupted by 3% 'Gaussian' noise in Figure 2.11.

	Cortical & background	Adipose tissue & spongy bone	Muscle
FCM	73.27%	69.9%	58.56%
FCM_S1	86.17%	65.93%	71.79%
FCM_S2	87.58%	66.68%	73.91%
KFCM_S1	87%	65.33%	72.85%
KFCM_S2	87.3%	66.18%	73.4%
NGFCM	93.03%	76.36%	83.53%
GMM_S1	93.22%	76.99%	85.38%
GMM_S2	92.27%	76.9%	84.56%
MFFCM	93.31%	77.43%	84.65%
IMFFCM_DS	**94.89%**	**77.83%**	**86.45%**

The experiments have been carried out on an ASUS computer with 1.5 GHz Intel Pentium processor and a RAM of 256M. The running time for each image varies between 20s –50s. A FCM-based segmentation method always converges within 10-30 iterations. With the increase of noise level, more running time and more iterations are needed. (**Appendix 3 gives a comparison on the algorithm complexity among different segmentation methods.**)

2.3   Conclusion

In this chapter, we introduce our FCM-based method for image segmentation. Compared to the FCM using Kernel with spatial constraints ([49]), the FCM using Markov Random Field via Bayesian theory with spatial constraint ([56]), as well as an algorithm using Gaussian Mixture Model with spatial constraints ([48]) whose structure is quite different from FCM-based methods, our method shows robust and stable performance. Nevertheless, in the analysis of medical images, segmentation with context independent features such as grey level and texture often leads to unsatisfactory results because these general features can not take into account the specialized background knowledge, which is important when doctors study them manually using their own vision and experience. Therefore, it is necessary to incorporate our a priori knowledge on medical image in order to guide or control the segmentation procedure for obtaining tissue classification.

3 Integration of human knowledge for intelligent tissue classification

In Chapter 2, we present our FCM-based method, and it shows robust and stable performance in image segmentation. However, image segmentation just partitions an image into a number of non-overlapped and constituent regions which are homogeneous inside with respect to some characteristics such as grey level or texture. Thus, specialized background knowledge is not taken into consideration in image segmentation. This knowledge is often indispensable when doctors carry out medical analysis manually.

A tissue may have varied image features ([14]). The grey level-based segmentation often results in:

– One segmented class includes pixels from different tissues.

– One tissue is separated into different classes.
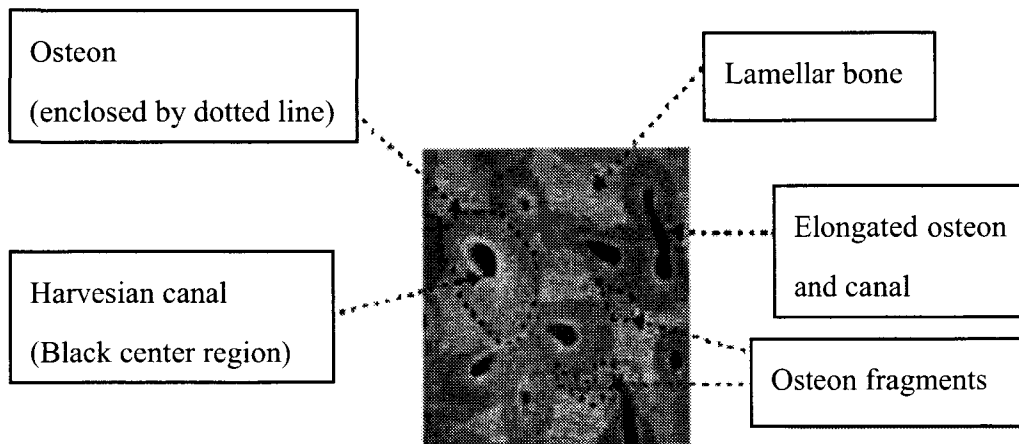
Figure 1.15 Magnified microradiograph of bone with features identified.

We take the Figure 1.15 – 1.17 again to show these two problems. Figure 1.15 shows the

important features in the bone cross section, the Harvesian canals, osteons, osteon fragments, and lamellar bone. The Harvesian canals, which are quite easily identified in the image, are the black areas. Osteons regions refer to the grey regions surrounding the canals. Different grey levels of the osteon regions indicate the levels of bone mineralization, where the lighter regions are more mineralized. The osteon fragments are the osteon regions that do not surround any canals. The brightest parts in the image that do not constitute the other regions are called the lamellar bone regions.

Figure 1.16 shows the segmentation result using an automatic system for bone image processing ([80]) which is based on K-means clustering algorithm ([37]). The regions in the bone cross section have been identified quite successfully, with the canals, osteons and lamellar assigned to different clusters. However, there are noticeable segmentation errors in some processed images, the bright patches (due to imaging artifacts) surrounding canals have been misclassified as lamellar regions. Figure 1.17 shows a magnified section of a segi ·nted image containing an osteon. These inaccuracies in segmentation area are the consequei .:e of the simplicity of the clustering method as it relies only on pixel grey level for segmentation.

(a)   (b)
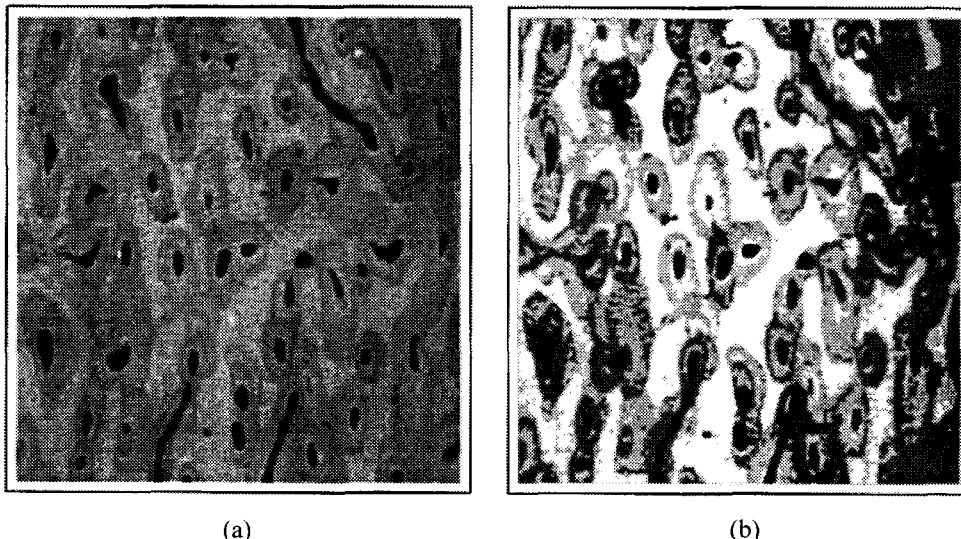
Figure 1.16 An example result of processing a bone image using the system.
(a) Original image. (b) Segmented image.
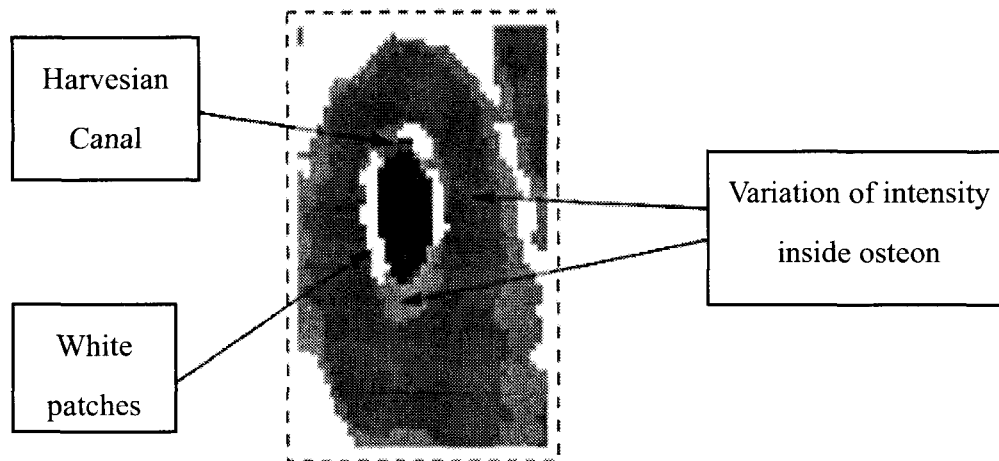
Figure 1.17 A magnified section of a segmented image containing an osteon.

For solving these problems, we propose to integrate a priori knowledge on medical image analysis in order to guide or control the segmentation procedure to obtain better results of tissue classification.

Various tissue classification systems with medical applications have been developed, such as:

- The system for brain ([14-16]),

- The system for bone ([17]), and

- The system for chest ([18]).

Nevertheless, all these systems focus on the specific applications. So they are not normalized and structured, and lack of certainty and precision in other applications. In addition, they do not hold the user-friendly interface.

In this chapter, we first develop a specific system for automatic classification of human thigh which is based on the a priori knowledge concerning the tissue geometric structure ([29]) of thigh. Next, we carry out the abstraction to find the common tissue features among different parts of human body. In this way, we construct generalized model which is no longer limited to a specific application. We validate this generalized system on human thigh, crus, arm, forearm, and brain and we obtain satisfying results. Moreover, we add a user-friendly interface to facilitate the human

machine interaction to obtain the a priori knowledge from experts.

3.1 A specific intelligent system for automatic classification of human thigh

In this section, we first introduce our specific model for human thigh, then present the experimental results. In the end, we give a conclusion.

3.1.1 Specific model

The a priori knowledge on medical image analysis used in our study concerns the tissue geometric structure ([29]), especially the relative positions and the neighboring relations between different tissues in the slice. The five components in a MRI image of thigh are denoted as (Figure 3.1):

- A: image background,

- B: adipose tissue,

- C: muscle,

- D: cortical bone,

- E: spongy bone.
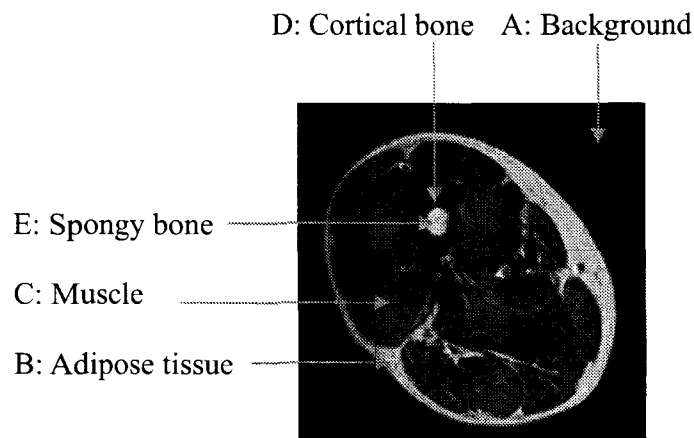
Figure 3.1 A MRI image of thigh.
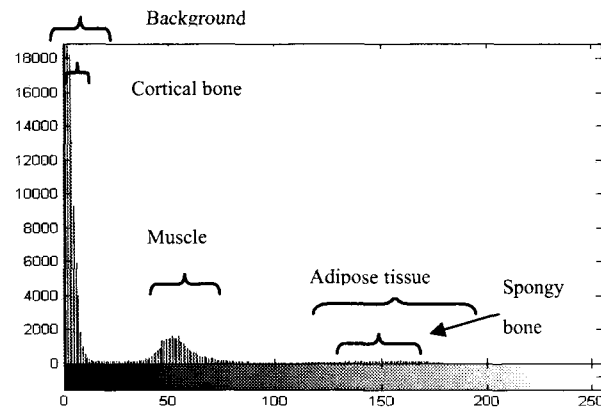
Figure 2.6 Histogram of a MRI image of thigh.

We take Figure 2.6 again to show the histogram of a MRI image of thigh.

In order to identify the four tissues, namely, adipose tissue, muscle, cortical bone, and spongy bone, we symbolize the surrounding relation and the neighboring relation between two components on the image.

We use a symbol '$\propto$' to denote the surrounding relation between two components on the image. From the a priori knowledge, we have:

(1) $B \propto A, C \propto A, D \propto A, E \propto A$

(2) $C \propto B, D \propto B, E \propto B$

(3) $D \propto C, E \propto C$

(4) $E \propto D$

The relation (1) means that all the four tissues of the thigh are included inside the background A. The relations (2) - (4) can be explained in the same way.

Next, we use '•' to denote the neighboring relation between two components on the image. We have:

(5) $A • B$

(6) B • A, B • C, B • D

(7) C • B, C • D

(8) D • B, D • C, D • E

(9) E • D

The relation (5) means that background A and adipose tissue B border each other. The relations (6) - (9) can be understood in the same way.

In addition, we can observe from Figure 3.1 and Figure 2.6 that the grey level of the background A is the darkest related to the four tissues and it is generally located in the regions close to the image edges. So, we can remove it easily according to its grey level and its location. For the remaining components B, C, D and E, the grey levels of the adipose tissue B and the spongy E are rather close each other.
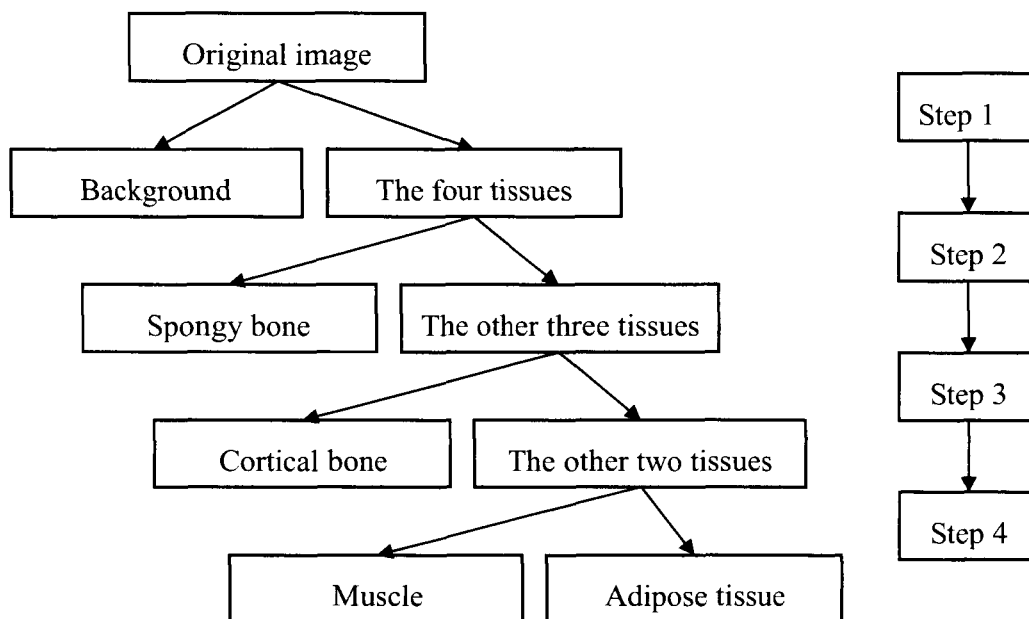
Figure 3.2 Knowledge guided segmentation of a MRI image of thigh.

Based on all these knowledge based rules, we can segment the original image of thigh into five classes using four steps. The principle of this procedure is shown in block diagram (Figure 3.2). In order to control the procedure of segmentation, we run our FCM-based method with dynamically selected window several times (step 1, 3, and 4 of Figure 3.2) for classifying image pixels into two

classes at each step.

Step 1: Background identification

From Figure 3.1, we can see that spongy bone and adipose tissue are the brightest related to the other classes and the background is the darkest. If we segment the original image into two classes using our FCM-based method with dynamically selected window, then the background is in one class, and adipose tissue in another (Figure 3.3). From the surrounding relation (1), we know that the background is the most exterior related to the other four classes. And from the neighboring relation (5), we know that background and adipose tissue border each other. Thus, we can easily extract the background from the original image. The corresponding result is shown in Figure 3.4.

Figure 3.3 Segmentation of the original image into two classes.
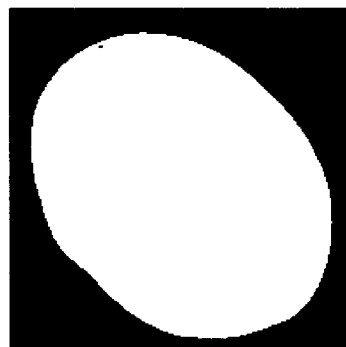
Figure 3.4 Result of classifying background.
(Black part is background, white part includes the four tissues.)

Step 2: Identification of spongy bone

We can observe in Figure 3.1 that spongy bone and cortical bone are strongly contrasted. The spongy bone is the brightest, and the cortical bone is the darkest. They will certainly belong to two different classes (Figure 3.3). From the surrounding relation (4) we know that spongy bone is surrounded by the cortical bone. From the neighboring relation (9) we know that spongy bone and cortical bone border each other. Thus, if we select the class of the spongy bone, it is a connected region and isolated from the outside. As the background belongs to the same class as cortical bone and we have already removed it at Step 1, the remaining pixels of this class belong to cortical bone and spongy bone is located in another class. Moreover, only for the application of thigh, we carry out a statistical analysis on several sequences of MRI images of thigh in order to obtain the relative position of spongy bone to the top, the bottom, the left side, and the right side of thigh, so we can separate it from the original image. This relative position of the spongy bone is described in Figure 3.5 (v is the vertical length of the thigh, and h is the horizontal length of the thigh). From this knowledge, the spongy bone is compressed to a small rectangle and it can be extracted by comparing grey levels with those of the neighboring pixels in it. (Figure 3.6).
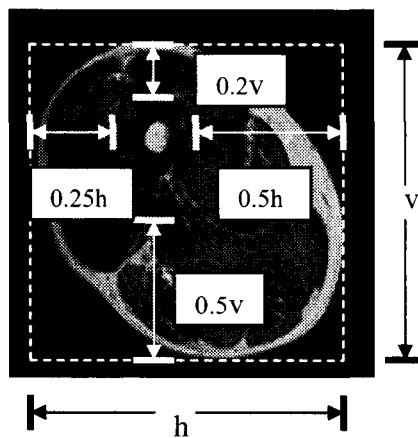
Figure 3.5 Determination of the relative position of the spongy bone of thigh (a rectangle).
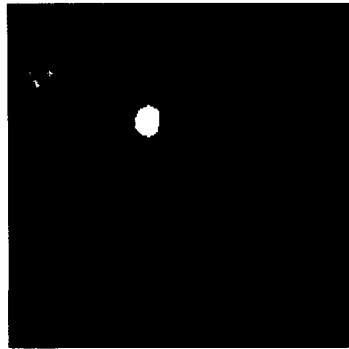
Figure 3.6 Extraction of the spongy bone from the rectangle.

Step 3: Identification of cortical bone

If we select a suitable window centered on the extracted spongy bone, we can obtain spongy bone, cortical bone, and one part of muscle in it. As we have already identified the spongy bone, we just need to segment the other two tissues using our FCM-based method. The cortical bone can be identified by the surrounding relation (4) and neighboring relation (9). Only for the application of thigh, we carry out a statistical analysis on several sequences of MRI images of thigh in order to determine this window. The size of this window is selected as follows.

Denoting m= min(h', v'), smaller value of the height and the width of the spongy bone (Figure 3.6). According to the knowledge, the size of the suitable window can be selected so that the distance between each of three edges (left, right, top) of the spongy bone and the corresponding edge of the window is m and the bottom edge of the window crosses the middle line of thigh (Figure 3.7).

In this window, we remove the identified spongy bone and segment the other pixels into two classes using our FCM-based method (Figure 3.8). From the surrounding relation (4) we know that the spongy bone is surrounded by the cortical bone, and from the neighboring relation (9), we know that spongy bone and cortical bone border each other. Therefore, the segmented class which borders with spongy bone, then we select the maximum connected component in this class, is considered as the cortical bone (Figure 3.9).

Middle line of thigh
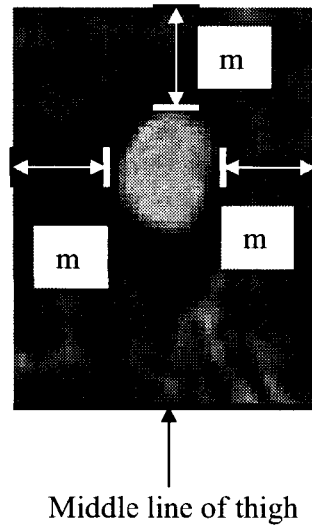
Figure 3.7 Selection of a suitable window for extracting cortical bone.
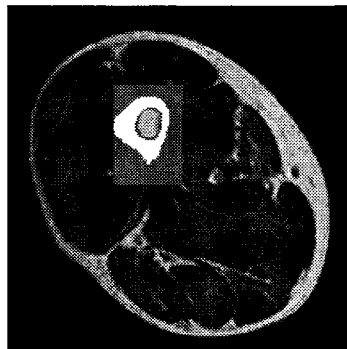
Figure 3.8 Segmentation of pixels around the spongy bone in the selected window.
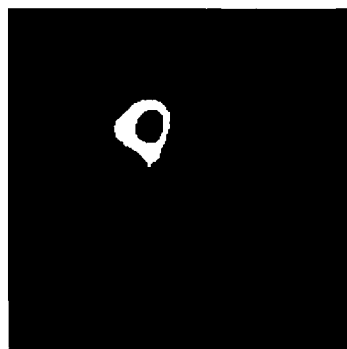
Figure 3.9 Identified cortical bone.

Step 4: Identification of adipose tissue and muscle

This last step is to identify adipose tissue and muscle using our FCM-based method. From the

surrounding relation (2), we know that muscle is surrounded by the adipose tissue. Therefore, we first recognize adipose tissue then muscle. The results are shown in Figure 3.10 and Figure 3.11.
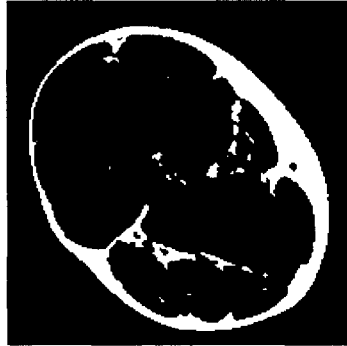
Figure 3.10 Identified adipose tissue.

Figure 3.11 Identified muscle.

3.1.2 Experimental results and analysis

In this part, we show the experimental results of the knowledge guided segmentation for classifying tissues of thigh. The following parameters have been used in all experiments: $m = 2, \varepsilon = 0.001$.

To compare the performance of dynamically selected window, 3×3 window, 5×5 window, and 7×7 window, we test them on 52 images of thigh in the mid-thigh level. Located on the axial plane, all of them are T1-weighted MRI images with a thickness of 10 mm, they are from 26 sequences of MRI images of thigh, each corresponding to one patient, and those patients are from 45 to 70 years old. The images are obtained from a system of Philips Intera of 1.5 Tesla, the size of voxel is 0.93

* 0.93 * 1.0 mm^3, and the coding is 12 bits. In addition, the signal has been analyzed by spin echo technique in order to minimize artifacts.

Clinical interest of this study is to analyze the evolution of the volume of soft tissue at the mid thigh. It has been shown that there is a relationship between the muscle surface and strength ([88]). It is also possible to analyze the evolution of soft tissues along the lower segments ([89]). Other studies have shown a significant correlation of muscle volume in the hemiplegic subject with an index of functional independence ([90]). The tissue classification can also be used in biomechanics to calculate the inertial properties of body segments from MRI sequences ([91]).

Having segmented each image of thigh into one background and four tissues, we assign the following grey levels to these classes in order to generate a synthetic image and intuitively compare the classification results between them. The grey levels of pixels on this synthetic image are:

background: 20; adipose tissue: 100; spongy bone: 150; cortical bone: 200; muscle: 250;

Figure 3.12, Figure 3.13 and Figure 3.14 compare the classification results between the image without noise and that with 3% and 8%'Gaussian' noise. In Figure 3.12, the original image and the corresponding reference classification result provided by a medical expert in the CHRU (France) are given in Figure 3.12 (a) and Figure 3.12 (b) respectively. The synthetic images obtained from the classification results with the four different window sizes are shown in Figure 3.12 (c)-(g). The same principle is applied to Figure 3.13 and Figure 3.14. We can see that in Figure 3.12, Figure 3.13 and Figure 3.14 the classification performance of the method of dynamically selected window outperforms the others.

(a)

(b)

(c)

(d)

(e)

(f)

(g)
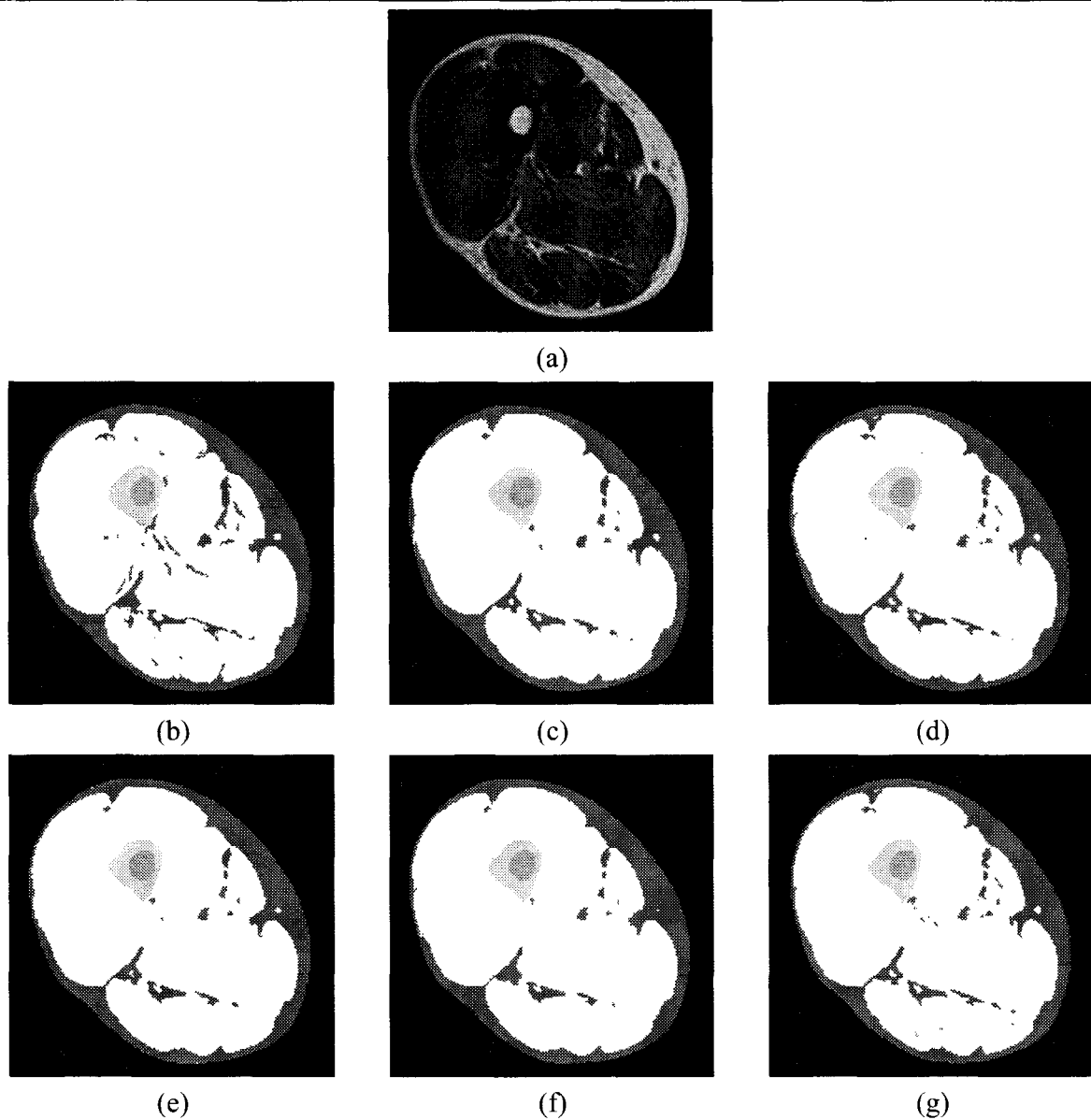
Figure 3.12 Classification results for one image of thigh.

(a) original image. (b) expert's classification result. (c) result by MFFCM. (d) result by IMFFCM_3. (e) result by IMFFCM_5. (f) result by IMFFCM_7. (g). result by IMFFCM_DS.

(a)

(b)   (c)   (d)

(e)   (f)   (g)
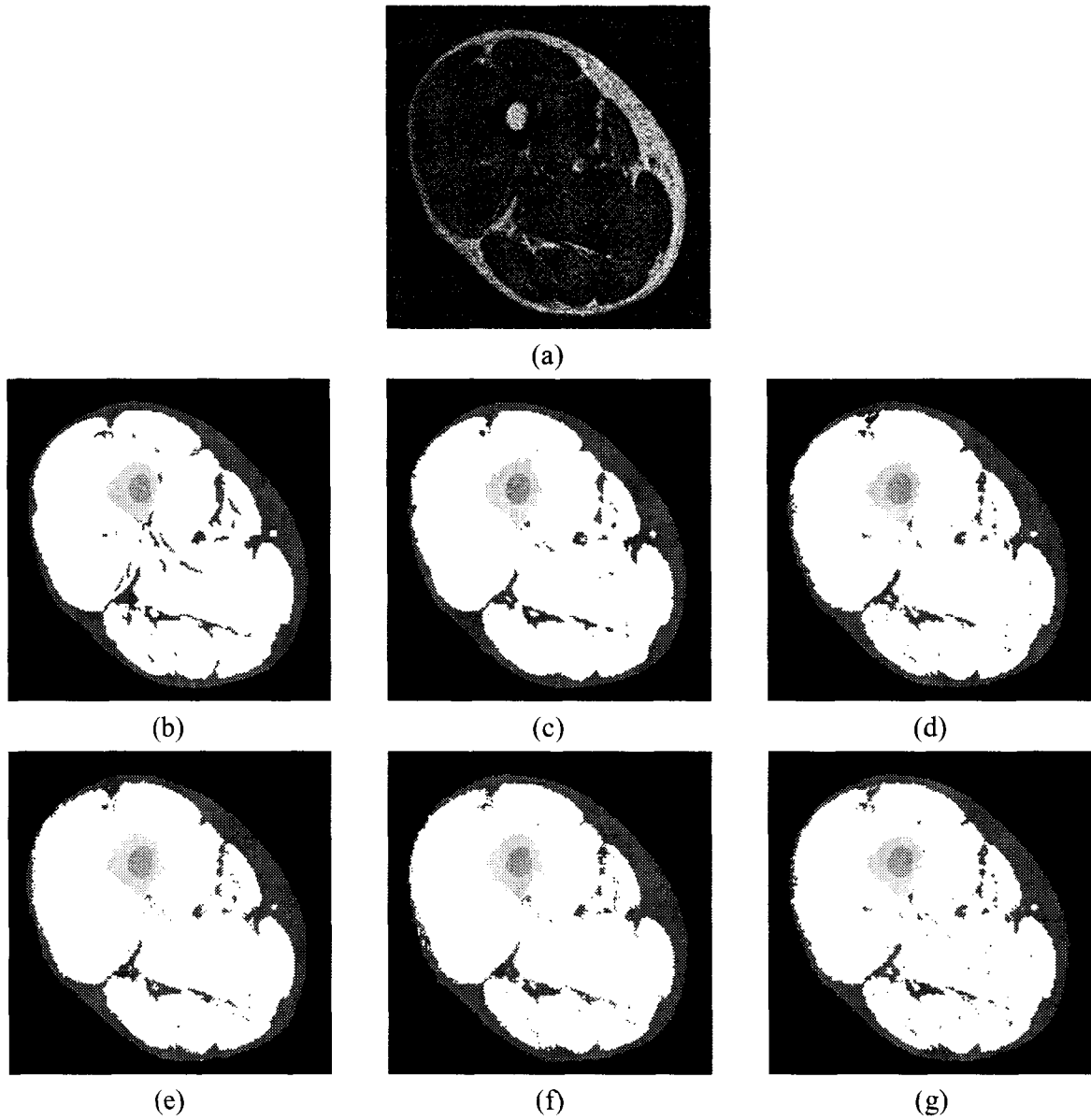
Figure 3.13 Classification results for one image of thigh with artificially added noise.

(a) original image with artificially added 3% 'Gaussian' noise. (b) expert's classification result. (c) result by MFFCM.

(d) result by IMFFCM_3. (e) result by IMFFCM_5. (f) result by IMFFCM_7. (g). result by IMFFCM_DS.

(a)

(b)   (c)   (d)

(e)   (f)   (g)
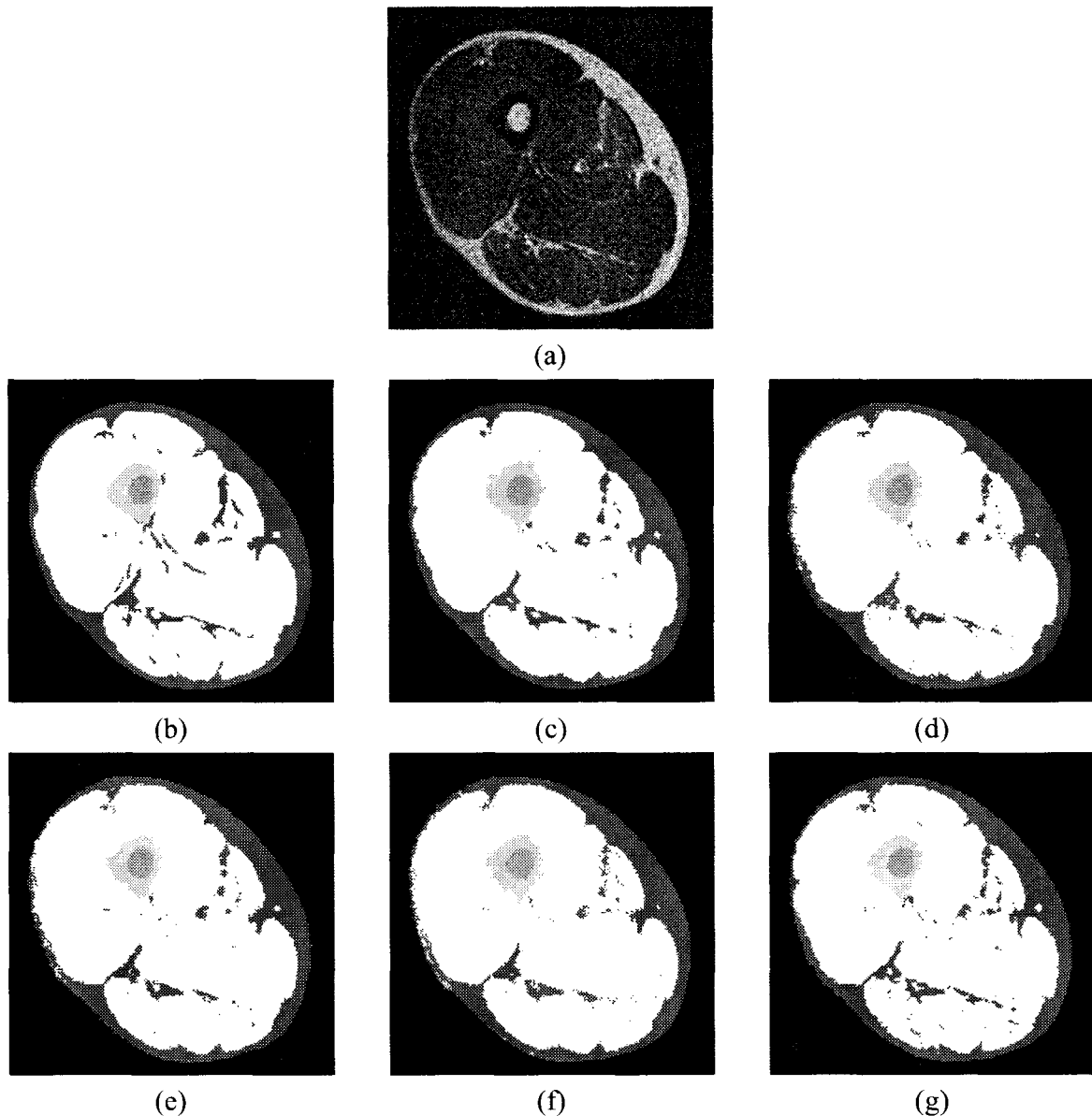
Figure 3.14 Classification results for one image of thigh with artificially added noise.
(a) original image with artificially added 8% 'Gaussian' noise. (b) expert's classification result. (c) result by MFFCM.
(d) result by IMFFCM_3. (e) result by IMFFCM_5. (f) result by IMFFCM_7. (g). result by IMFFCM_DS.

TABLE 3.1-3.3 quantitatively compare the classification results obtained from our FCM-based method with different window sizes and the reference classification results, for one image without noise, one with 3% 'Gaussian' noise, and one with 8% 'Gaussian' noise. The comparison criterion (cc) is the same as in Eq.(2.4).

TABLE 3.1 Quantitative comparison of classification results for one image of thigh by our FCM-based method with different window sizes.
(a) MFFCM, (b) IMFFCM_3, (c) IMFFCM_5, (d) IMFFCM_7, (e) IMFFCM_DS.

	Adipose tissue	Cortical bone	Muscle	Spongy bone
MFFCM	0.7856	0.8560	0.9493	0.8182
IMFFCM_3	0.8276	0.8780	0.9541	0.8522
IMFFCM_5	0.7931	0.8778	0.9500	0.8492
IMFFCM_7	0.7860	0.8719	0.9465	0.8464
IMFFCM_DS	**0.8356**	**0.8778**	**0.9563**	**0.8632**

TABLE 3.2 Quantitative comparison of classification results for one image of thigh corrupted by 3% 'Gaussian' noise by our FCM-based method with different window sizes.
(a) MFFCM, (b) IMFFCM_3, (c) IMFFCM_5, (d) IMFFCM_7, (e) IMFFCM_DS.

	Adipose tissue	Cortical bone	Muscle	Spongy bone
MFFCM	0.8095	0.7907	0.9447	0.8498
IMFFCM_3	0.8022	0.8250	0.9459	0.8601
IMFFCM_5	0.7849	0.8009	0.9431	0.8256
IMFFCM_7	0.7745	0.7986	0.9366	0.8537
IMFFCM_DS	**0.8194**	**0.8370**	**0.9482**	**0.8606**

TABLE 3.3 Quantitative comparison of classification results for one image of thigh corrupted by 8% 'Gaussian' noise by our FCM-based method with different window sizes.
(a) MFFCM, (b) IMFFCM_3, (c) IMFFCM_5, (d) IMFFCM_7, (e) IMFFCM_DS.

	Adipose tissue	Cortical bone	Muscle	Spongy bone
MFFCM	0.8048	0.7717	0.9453	0.8398
IMFFCM_3	0.7685	0.8051	0.9408	0.8181
IMFFCM_5	0.7849	0.8172	0.9417	0.8353
IMFFCM_7	0.7508	0.77	0.9328	0.8281
IMFFCM_DS	**0.8127**	**0.82**	**0.9480**	**0.8434**

From TABLE 3.1-3.3, we can see that the method of dynamically selected window size shows the best classification performance of all the methods. In addition, with the increase of noise level, the classification rate is generally stable, which means that our method is very robust to noises. Moreover, in low noise level, the performance of our method with 3×3 window is the best among those three window sizes. When noise level increases, the one with 5×5 window is the best. This also explains the fact that with the increase of noise level, spatial information in a larger and

adaptive neighboring area is needed.

We perform an analysis of confidence intervals ([92]) on our classification result obtained by IMFFCM_DS for adipose tissue (TABLE 3.1) to show the stability of our results. The obtained confidence interval is [0.8324, 0.8388], which is very close to the sample mean 0.8356. This small confidence interval can explain why the results are close each other in some tables. In fact, this small variation of the results means that our method is very robust and stable. **The detailed analysis is given in Appendix 4.**

Figure 3.15 compares the classification results for one image with 1% 'Gaussian' noise when applying FCM_S1, FCM_S2, KFCM_S1, KFCM_S2 and our FCM-based method with dynamically selected window. The four classical methods have been applied in the same way as our FCM-based method by segmenting one class into two sub-classes at each step. TABLE 3.4 shows the corresponding quantitative comparison results. We see that our method shows the best classification result. As it incorporates both local and global spatial information of neighboring pixels, it is more robust to noise.
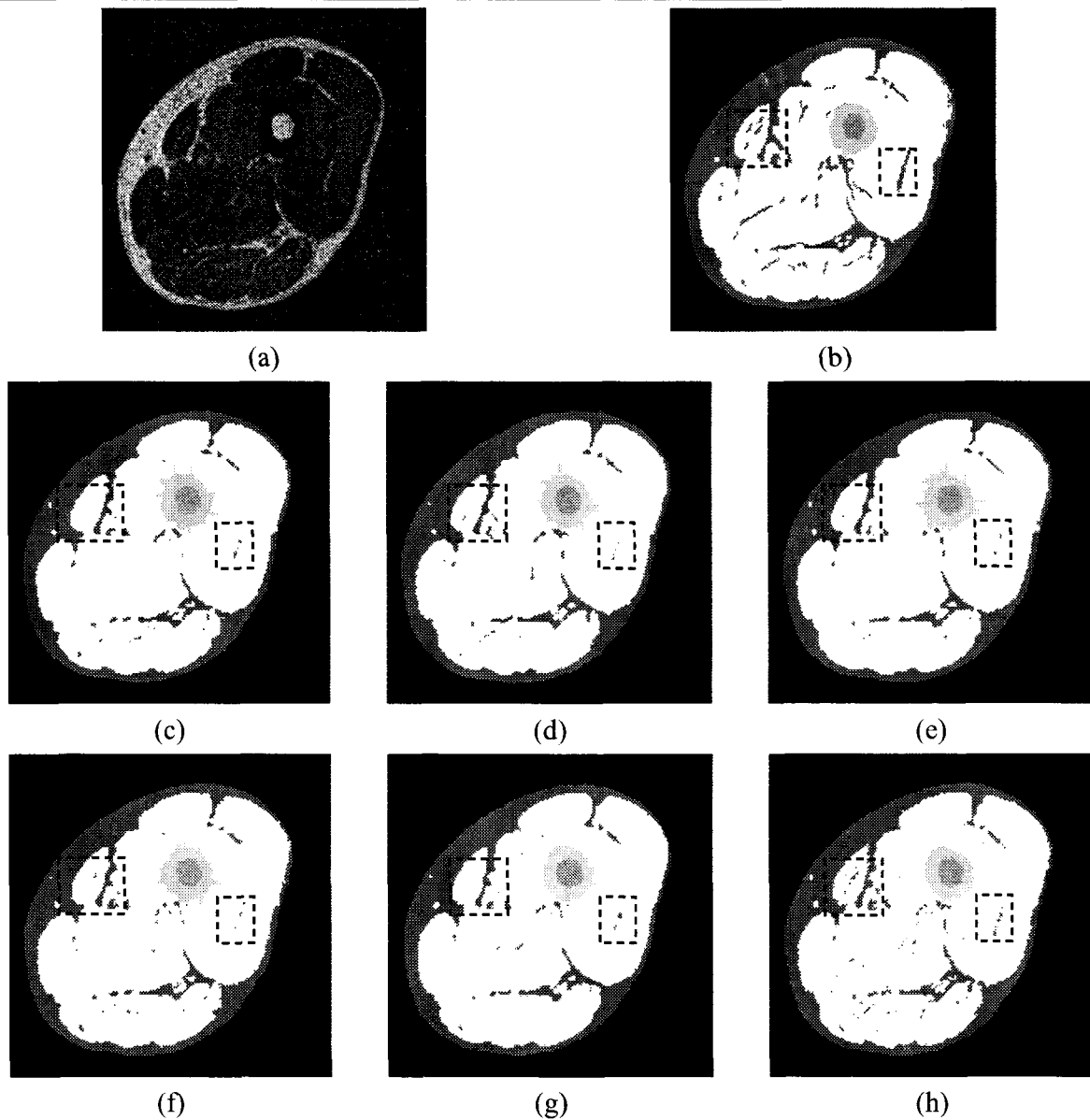
Figure 3.15 Classification results for one image of thigh with artificially added noise.

(a) original image with artificially added 1% 'Gaussian' noise. (b) expert's classification result. (c) result by FCM_S1. (d) result by FCM_S2. (e) result by KFCM_S1. (f) result by KFCM_S2. (g) result by MFFCM. (h). result by IMFFCM_DS.

TABLE 3.4 Quantitative comparison of classification results for one image of thigh corrupted by 1% 'Gaussian' noise.

	Adipose tissue	Cortical bone	Muscle	Spongy bone
FCM_S1	0.7960	0.6874	0.9264	0.8018
FCM_S2	0.8099	0.7124	0.9298	0.8125
KFCM_S1	0.7724	0.6384	0.9207	0.7948
KFCM_S2	0.7793	0.7041	0.9253	0.8273
MFFCM	0.7839	0.7368	0.9309	0.7615
IMFFCM	**0.8140**	**0.8213**	**0.9349**	**0.8553**

The experiments have been carried out on an ASUS computer with 1.5 GHz Intel Pentium processor and a RAM of 256M. The running time for each image varies between 20s –50s. A FCM-based segmentation method always converges within 10-30 iterations. With the increase of noise level, more running time and more iterations are needed.

In this section, we present an intelligent specific system for tissue classification of thigh. In this system, a priori knowledge is incorporated to guide and control the segmentation procedure for tissue classification. Four steps have been proposed for correctly separating the five classes of the thing image: background, spongy bone, cortical bone, adipose tissue and muscle. Compared to the other existing classification results, our results are satisfying. For example, muscle and adipose tissue can not be recognized in ([93]), cortical bone and spongy bone can not be recognized in ([4]), and adipose tissue and spongy bone can not be recognized in ([2]). In practice, for most of the existing medical image segmentation methods, background knowledge or specialized knowledge has never been incorporated.

One drawback of the proposed method is that it lies too much on the specific knowledge of the thigh structure and background knowledge incorporation is a manual procedure. For segmenting images of other organs, we need to incorporate new background knowledge and construct new models. Therefore, it is necessary to develop a more generalized system permitting to formalize all kinds of human knowledge on medical image observation and automatically incorporate them into the image segmentation procedure.

Although the classification rate is not greatly higher than existing methods, the proposed method is very significant in medical image analysis. In fact, the significance of different medical classification methods is in two levels: (1) robustness related to noises, (2) accuracy for identification of some key but small medically interpretable details, such as tumors and deformation of organs. The proposed tissue classification method has been proven to be very efficient when noise level becomes important. Moreover, the proposed method lead to higher accuracy of tissue identification related to the existing techniques and then some details such as that observed in the rectangle of Figure 3.15 can be recognized and interpreted. Of course, most of existing classification methods can also lead to high classification rates for identifying massive human body parts. However, in practice, a classification rate of 98% can give a medical conclusion quite different from that of 99%. Higher the classification rate is, closer the related automatic tissue classification system is to professional medical experts.

Using the obtained classification results, we will keep in working on the quantification of the muscle/fat ratio, assessment of the muscle/fat temporal variation, and measurement of the volume of muscle, fat and bone in human legs. Also, we will attempt to select other features to describe each pixel of the image. In addition, we will analyze the performance when we use the kernel-based distance ([60-63]) to replace the Euclidean distance in the standard FCM objective function.

3.2   Generalized system for automatic tissue classification

In Section 3.1, we present an intelligent specific system for tissue classification of thigh. In this system, a priori knowledge is integrated to guide and control the segmentation procedure for obtaining tissue classification. Compared to the other existing classification results, our results are satisfying.

One disadvantage of the proposed method is that it depends too much on the specific knowledge of

the thigh structure and background knowledge incorporation is a manual procedure. For segmenting other organs, we need to construct new models to incorporate new background knowledge.

In this section, we carry out the abstraction in order to find the common tissue features among different parts of human body. In this way, we construct a more generalized system which is not limited to a specific application but permits to formalize all kinds of human knowledge on medical image observation. We have tried to integrate the knowledge into the segmentation procedure, but the results are not satisfying. So we propose to do the image segmentation first. Then, based on the segmentation result, we incorporate the knowledge into the image classification procedure.

3.2.1 Three-level system architecture

We construct a three-level structure for our medical image analysis system. It is shown in Figure 3.16.

The low level is the knowledge acquisition, it contains two components: Interface module and Knowledge Base module. Interface module is a "ask-answer" form. By using this form, we can obtain the knowledge expressed by experts using linguistic description. From all the answers in the forms for the application of thigh, crus, arm, forearm, and brain, we find six common features, of which our Knowledge Base module is composed: (1). relative positions between tissues, (2). neighboring relation of each tissue, (3). ranking order of all tissues according to their areas, (4). number of connected components of certain tissues, (5). tissues which have similar grey level, and (6). shapes of certain tissues.

The middle level is rules generation, it includes two parts: geometric models module and rules module. We symbolized the knowledge which is acquired from the low level. The Geometric models module permits to formalize the knowledge given by experts. Then, we define seven rules

for each geometric model. These rules permit to label tissues from original image.
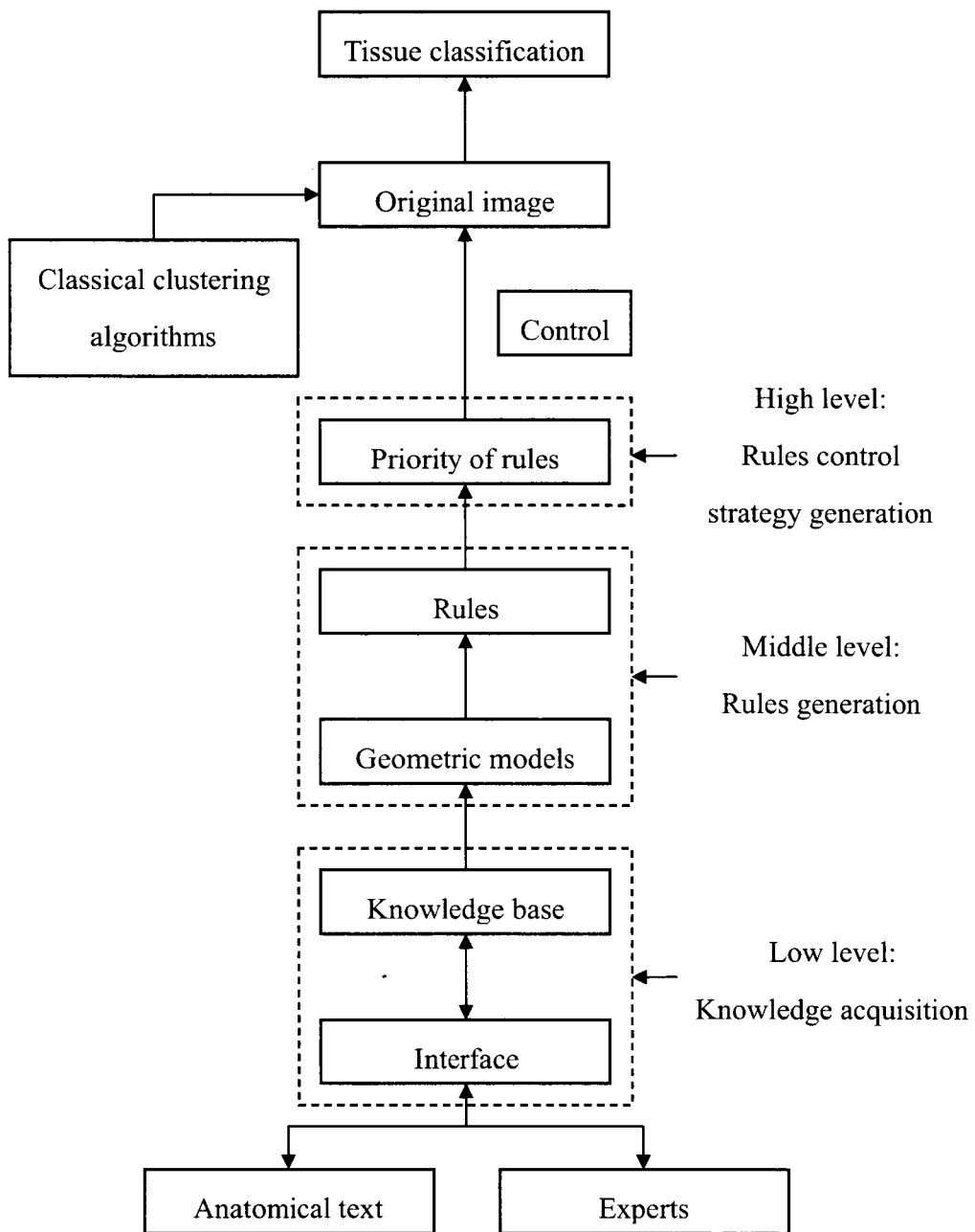
Figure 3.16 The three-level structure for tissue classification with knowledge incorporation.

In **high level**, the Rules control strategy generation level, we propose two principles to define the priorities for these rules in order to optimize their application. The rules with higher priorities

will be applied before those with lower priorities.

Next, more details are given as follows.

3.2.1.1 Low level: Knowledge acquisition

The low level includes a Knowledge base module and an Interface module. The knowledge base is composed of a number of features used for classifying each tissue. Normally, this knowledge is acquired through three channels ([94]). The first is a documented discussion with a neurologist which aides in deciding what are the important anatomical features that need to be modeled. The second is the use of anatomical text books and neuro-anatomical atlases. And the third is an informal discussion with neurologists and neuro-radiologists. These channels allow to record any anomalies in the representation of the anatomy of tissues. The Interface module is an online questionnaire. The experts are invited to fill this questionnaire or we search for the answers from the anatomical text books. Thus, the knowledge is expressed using linguistic description.

We take the human thigh as an example to show this questionnaire:

1. Does the spongy bone is included inside the cortical bone?

2. Does the adipose tissue and the muscle border each other?

3. Can you tell us which tissue have the maximum area among muscle, spongy bone and cortical bone?

4. How many connected components does the spongy bone have?

5. Does the spongy bone and the adipose tissue have similar grey level?

6. Can you tell us the shape of the adipose tissue?

....

From all the answers collected in this questionnaire, we concentrate on the following six features, of which the Knowledge base module is composed.

(1). Relative positions between tissues

Tissues can be correctly identified and separated from segmented class if we know the relative positions between them. For example, if we know that two segmented classes are tissue 1 and tissue 2, and tissue 1 is located on the left of tissue 2, we can identify them easily.

(2). Neighboring relation of each tissue

It is an important feature for identifying a tissue. We can identify one tissue easily from a set of segmented classes if its neighboring tissue is already identified or labeled.

(3). Ranking order of all tissues according to their areas

This information is important for identifying one tissue if we know its area is between two already labeled tissues. Especially, it enables to recognize the tissue corresponding to the biggest or the smallest area.

(4). Number of connected components of certain tissues

If we know exactly the number of connected components of one specific tissue, we can identify it easily.

(5). Tissues having similar grey level

When we carry out image segmentation, we often obtain several tissues in the same class because they have similar grey levels. This knowledge permits to recognize tissues in the same class using other geometric features such as relative positions between tissues. This knowledge can also be used to determine the number of classes before starting the FCM algorithm for image segmentation.

(6). Shape of certain tissue

Undoubtedly, this information can help us to identify tissues with regular shapes.

3.2.1.2 Middle level: Rules generation

In the low level, we collect in the Knowledge base module a series of features for tissue classification. In the Geometric model module of the middle level, we formalize these features and then store them in a predefined data structure, i.e. a 2-dimensional array. Thus, using this formalized knowledge on geometric features of tissues, we can effectively build an automatic system for tissue classification. Based on these formalized features, we set up in the Rules module one rule for each feature in order to label tissues.

Assuming there exist n tissues on a specific medical image denoted as $T_1,...,T_n$, we formalize the knowledge on geometric features of tissues as follows.

(1). The set of **Relative Positions** between tissues

$$RP = \left\{ < A, T_i, T_j > \mid i, j \in \{1,...,n\} \text{ and } T_i \neq T_j \right\}$$ (3.1)

where A is an attribute between two tissues and

$A \in$ {above, below, left, right, above left, below left, above right, below right, surrounding, outside} (3.2)

For example, " <above, Tissue1, Tissue2> " means that Tissue1 is above Tissue2.

(2). The matrix of **Neighbors for Tissues**

It is a n×n matrix denoted as $NT = \{nt_{ij}\}$, $i, j \in \{1,...,n\}$. nt_{ij} is the element in the position (i,j) of the matrix.

- If $nt_{ij} = 1$, then T_i and T_j are neighbors.

- If $nt_{ij} = 0$, then T_i and T_j are not neighbors.

(3). The **List of Tissues** with one connected component ranked in the decreasing order of their

Areas

$$LTA = \{T_{i1}, T_{i2}, ..., T_{iq}\} \ where \ i, q \in \{1, ..., n\}, \ Area(T_{ij}) > Area(T_{ik}) \ for \ j < k \qquad (3.3)$$

T_{iq} is the qth tissue in the ith list.

(4). The set of Numbers of Connected components in tissues

$$NC = \{< T_i, nc_i > | \ i \in \{1, ..., n\}\} \qquad (3.4)$$

nc_i is the number of connected components in tissue T_i.

(5). The set of Groups of Tissues having similar grey levels

$$GT = \{GT_i \ | \ i \in \{1, ..., p\} \ \text{p is number of groups of grey levels,} \ \} \qquad (3.5)$$

and $\qquad$ Grey_level(T_j)=Grey_level(T_k) for any two tissues $T_j, T_k \in GT_i (j \neq k)$ $\qquad$ (3.6)

GT_i is the ith group of tissues having similar grey levels.

(6). The Set of shapes for the Tissues with one connected component

$$ST = \{< T_i, S_i > | \ i \in \{1, ..., n\} \ and \ S_i \in \{\text{triangle, circle, rectangle,} ...\}\} \qquad (3.7)$$

In this way, all geometric knowledge collected from experts are formalized and stored in the related data structure described as follows.

(1). **Relative Positions between tissues**

Name of array: RelativePosition

The data structure is a n×3 array in the following form:

Attribute	Tissue 1	Tissue 2

Attribute = {above, below, left, right, above left, below left, above right, below right, surrounding,

outside}.

For example, (above, Tissue 1, Tissue 2) means Tissue 1 is above Tissue 2.

(2). Neighboring Relation of each tissue

Name of array: NeighboringRelation

The data structure is a n×n array in the following form:

	Tissue 1	Tissue 2	...	Tissue n
Tissue 1				
Tissue 2				
...				
Tissue n				

For example, NeighboringRelation(1,2) = 1 means Tissue 1 and Tissue 2 are neighbors.

(3). Ranking Order of all tissues according to their Areas

Name of array: RankingOrderofArea

The size of array depends on the number of tissues whose areas are known for us. The corresponding data structure is in the following form:

Tissue 1	Tissue 2	Tissue 3	...	Tissue n

The ranking order of the areas of the tissues is descendent. For example, (Tissue 1, Tissue 2, Tissue 3) means Area(Tissue 1) > Area(Tissue 2) > Area(Tissue 3).

(4). Number of Connected components of certain tissues

Name of array: NumberofConnectedComponents

The data structure is a n×2 array in the following form:

Number of connected components	Tissue name

For example, (1, Tissue n) means the number of connected components of Tissue n is 1.

(5). Tissues which have Similar Grey Level

Name of array: SimilarGreyLevel

The size of array depends on the number of tissues having similar grey levels, the data structure is defined in the following form:

Tissue 1	Tissue 2	Tissue 3	...	...

For example, (Tissue 1, Tissue 2, Tissue 3) means Tissue 1, Tissue 2 and Tissue 3 have similar grey levels.

(6). Shape of certain Tissue

Name of array: ShapeofTissue

The data structure is a $n \times 2$ array in the following form:

Tissue name	Shape

Shape = {triangle, circle, rectangle, ...}

For example, (tissue 1, circle) means the shape of tissue 1 is a circle.

In addition, we need three more arrays to store the segmentation result by our proposed FCM algorithm, the clasification state for each tissue, and the already classified tissues, respectively.

(1). Segmentation result by our proposed FCM algorithm

Name of array: SegmentationResult

The data structure is a $n \times n$ array, with the same size as the original image. Before we run our proposed FCM algorithm, we predefine the number of classes for image segmentation. When the segmentation is finished, each pixel in the original image is labeled a specific class. The array "SegmentationResult" is just used to store the corresponding class label for each pixel in the

original image.

We assign a specific value to each class. For example, we assign the value "1" to class 1, "2" to class 2, etc. So each pixel in the original image will be assigned a specific value according to its class label, this value is stored in the corresponding position in array "SegmentationResult".

For example, the pixel in the position (3,5) of the original image belongs to class 2, so "2" is stored in the position (3,5) of the array "SegmentationResult".

(2). The clasification state for each tissue

Name of array: ClassificationState

The data structure is a 1×n array, n is the number of tissues in the original image. It is in the following form:

State of Tissue 1	State of Tissue 2	State of Tissue 3	...	State of Tissue n

For example, if Tissue n is not classified yet, the value in the corresponding position in this array is "0". If Tissue n is already classified, the value in the corresponding position in this array is "1".

(3). The already classified tissues

Name of array: ClassifiedTissues

The data structure is a n×n array, with the same size as the original image. We initialize each element in this array as "255".

Before classifying tissues, we assign a specific value to each tissue in order to denote them. For example, we assign the value "1" to muscle, "2" to adipose tissue, etc. When a specific tissue is classified, all the pixels belonging to this tissue are assigned the corresponding label value. Then, for all these pixels, their label value is stored in corresponding positions in the array

"ClassifiedTissues".

When applying the Fuzzy C-Means algorithm for image segmentation, we often obtain several tissues in one segmented class and several classes corresponding to one tissue. This is because the feature used in this algorithm is based on grey levels. A knowledge guided intelligent control procedure is used for splitting obtained classes of pixels denoted as $C_1, C_2, ..., C_p$ into tissues. The predefined number of classes for the Fuzzy C-Means algorithm is p (we define this number by our a priori knowledge on images), i.e. the number of groups each including tissues of similar grey levels. In this case, we obtain classes each having similar grey levels.

For splitting each class into tissues and give significance to each class, we define the following rules according to the previous geometric model. These rules permit to recursively label tissues from classes.

Rule 1: Background extraction

It is easy to extract and label the background from an image because it is an object with only one connected component linking all the four bounds of the image.

Rule 2: Relative positions of tissues

For any labeled tissue T_i,

IF there exists only one unlabeled tissue T_j so that $< A, T_i, T_j > \in RP$ (A can be any relation attribute),

AND IF T_j does not have similar grey levels with any other tissues,

THEN we can find the class corresponding to T_j by comparing positions of pixels and label it.

Rule 3: Neighbors of tissues

For each unlabeled tissue T_i,

IF its neighboring tissues have been all labeled,

THEN we can find and label T_i using connectivity analysis related to these neighboring tissues.

Rule 4: The tissues with one connected component ranked in the decreasing order of their areas

IF any group of similar grey levels GT_i has only one unlabeled tissue,

THEN we can rank all the unlabeled classes with one connected component according to their areas and make equivalence between them and all ranked unlabeled tissues with one connected component.

Rule 5: Numbers of connected components in tissues

Given a specific number of connected components,

IF the number of unlabeled tissues is 1,

AND IF the number of unlabeled classes is 1,

THEN this class is then equivalent to the related tissue.

Rule 6: Groups of tissues having similar grey levels

For each group of tissues GT_i corresponding to one class obtained by the fuzzy c-means algorithm,

IF only one tissue in it has not been labeled,

THEN we can easily label it by deducing the pixels corresponding to labeled tissues from this class.

Rule 7: Shapes of the tissues with one connected component

For each shape,

IF the number of unlabeled tissues in ST is 1,

AND IF the number of corresponding unlabeled classes with one connected component is 1,

THEN this class is equivalent to the related tissue.

3.2.1.3 High level: Rule control strategy generation

When we run our classification system, we first check the array "SimilarGreyLevel" in the Knowledge base module in order to determine the number of classes for segmenting the original image. Then we run the clustering algorithm to obtain the segmentation. Next, we can perform the classification by iteratively applying the above seven rules. In order to optimize the application of these rules, we define three priorities for these rules. The rules with higher priorities will be applied before those with lower priorities. Two principles are proposed to define the priorities.

(1). The priority of a rule can be defined according to the number of the corresponding premises. Rules with fewer number of premises have higher priority than those with bigger number of premises. Then, we have: (a) Rule 1 has the highest priority, (b) Rules 2, 5, and 7 have the lowest priority, and (c) the priority of Rules 3, 4, 6 is medium.

(2). The priority of a rule can be defined according to the number of arrays involved. Rules with fewer number of arrays involved have higher priority than those with bigger number of arrays involved. For example, for applying the Rule 3, four arrays are involved, namely, the array "ClassificationState", "NeighboringRelation", "RelativePosition", and "ClassifiedTissues". So we have: (a) Rule 1 has the highest priority, (b) Rules 2, 3, and 4 have the lowest priority, and (c) the priority of Rules 5, 6, and 7 is medium.

Figure 3.17 shows the optimized strategy for rules application using the first principle proposed above. We can see that

– High priority: Applying Rule 1 for extracting the background.

– Medium priority: Recursively applying the combination of Rule 3, Rule 4 and Rule 6 for

identifying new tissues from the obtained classes until we can not recognize any new tissue.

– Low priority: Recursively applying the combination of Rule 2, Rule 5, Rule 7 for obtaining new tissues from the remaining classes until we can not recognize any new tissue.

The system recursively applied the rules in medium priority and the rules in low priority until all the known tissues are identified.
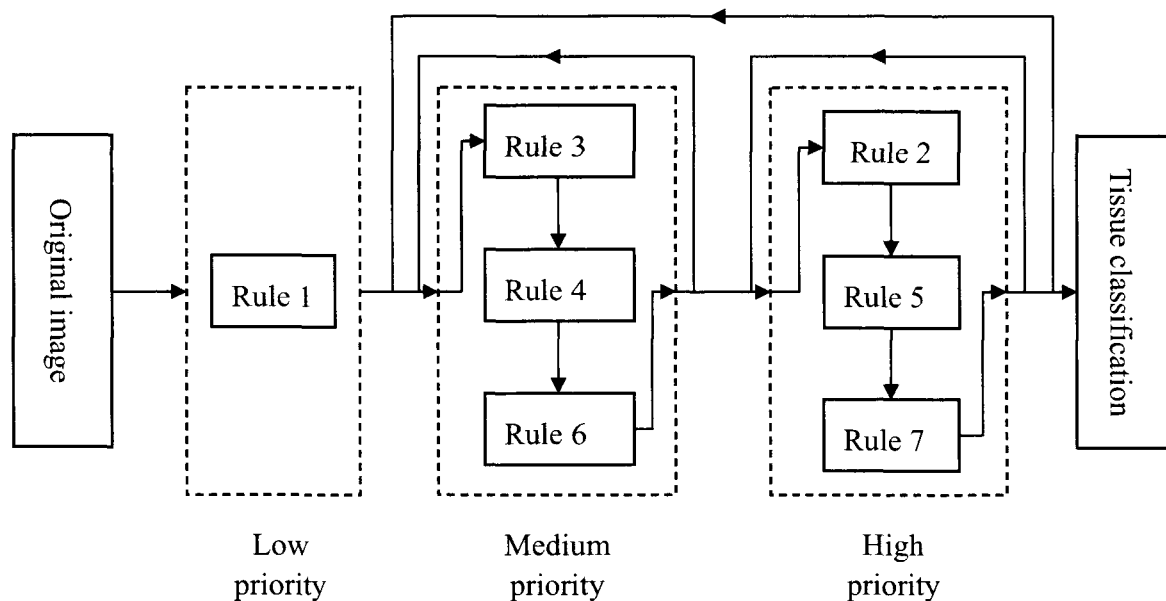
Figure 3.17 Optimized strategy for rules application.

3.2.2 Validation of the system using several specific applications

In this section, we first give an example for tissue classification of thigh to show how our system run. Then, we validate this system on human crus, arm, forearm, and brain to show its generality and certainty on other parts of human body. We first validate this system on human thigh. We use the Figure 3.1 again to show an image of thigh. We can see there are five classes to be identified: image background, adipose tissue, muscle, cortical bone, and spongy bone.

D: Cortical bone   A: Background

E: Spongy bone

C: Muscle
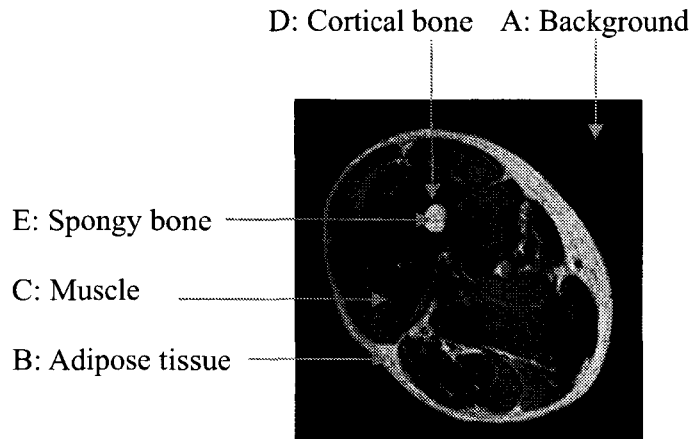
B: Adipose tissue

Figure 3.1 A MRI image of thigh.

In the Interface module, we prepare the following "ask-answer" form:

(1). Whether the spongy bone is included inside the cortical bone?

(2). Does the adipose tissue and the muscle border each other?

(3). Can you tell us which tissue has the maximum area among muscle, spongy bone and cortical bone?

(4). How many connected components does the spongy bone have?

(5). Does the spongy bone and the adipose tissue have similar grey level?

(6). Can you tell us the shape of the adipose tissue?

....

After we obtain the answers, we concentrate on the following six features, of which our Knowledge base module is composed.

(1). Relative positions between tissues

The spongy bone is included inside the cortical bone.

The muscle is included inside the adipose tissue.

....

(2). Neighboring relation of each tissue

The adipose tissue and the muscle border each other.

The spongy bone and the cortical bone border each other.

....

(3). Ranking order of all tissues according to their areas

The spongy bone's area is less than the muscle's area.

The cortical bone's area is less than the adipose tissue's area.

....

(4). Number of connected components of certain tissues

The spongy bone has one connected component.

The cortical bone has one connected component.

....

(5). Tissues which have similar grey level

The spongy bone and the adipose tissue have similar grey level.

The cortical bone and the background have similar grey level.

(6). Shape of certain tissue

Nothing.

Knowledge base module contains a series of features for tissue classification. In the Geometric model module of the middle level, we will symbolize them then store them in a computerized way.

(1). The set of relative positions between tissues:

We have symbolized this feature in Eq.(3.1), so we do not repeat to show it here.

<surrounding, adipose tissue, image background> (which means adipose tissue is included inside image background)

<surrounding, muscle, image background>

<surrounding, cortical bone, image background>

<surrounding, spongy bone, image background>

<surrounding, muscle, adipose tissue>

<surrounding, cortical bone, adipose tissue>

<surrounding, spongy bone, adipose tissue>

<surrounding, cortical bone, muscle>

<surrounding, spongy bone, muscle>

<surrounding, spongy bone, cortical bone>

<outside, image background, adipose tissue>(which means image background is outside adipose tissue)

<outside, cortical bone, spongy bone>

(2). The matrix of neighbors for tissues

	Background	AdiposeTissue	Muscle	Cortical Bone	Spongy Bone
Background	0	1	0	0	0
AdiposeTissue	1	0	1	1	0
Muscle	0	1	0	1	1
Cortical Bone	0	1	1	0	1
Spongy Bone	0	0	1	1	1

For example, NeighboringRelation(1,2)=1 means Background and Adipose Tissue are neighbors.

NeighboringRelation(3,4)=1 means Muscle and Cortical Bone are neighbors.

(3). The list of tissues with one connected component ranked in the decreasing order of their areas

We have symbolized this feature in Eq.(3.3), so we do not repeat to show it here.

<adipose tissue, cortical bone> (means the area of adipose tissue is more than cortical bone)

<adipose tissue, spongy bone>

<muscle, cortical bone>

<muscle, spongy bone>

(4). The set of numbers of connected components in tissues

We have symbolized this feature in Eq.(3.4), so we do not repeat to show it here.

<spongy bone, 1> (means spongy bone has one connected component)

<cortical bone, 1>

<background, 1>

(5). The set of groups of tissues having similar grey levels

We have symbolized this feature in Eq.(3.5) and Eq.(3.6), so we do not repeat to show it here.

<background, cortical bone> (means background and cortical bone have similar grey levels)

<adipose tissue, spongy bone>

Then, we store the symbolized knowledge in 2-dimensional arrays. In all these arrays, the five classes are assigned the following values:

1: image background,

2: adipose tissue,

3: muscle,

4: cortical bone,

5: spongy bone.

(1). Relative positions between tissues

Name of array: RelativePosition

The array is in this form:

Attribute	Tissue 1	Tissue 2

The different attributes are assigned the following values:

1: above,

2: below,

3: left,

4: right,

5: above left,

6: above right,

7: below left,

8: below right,

9: surrounding,

10: outside.

So the complete array is:

Attribute	Tissue 1	Tissue 2
9	2	1
9	3	1
9	4	1
9	5	1
9	3	2
9	4	2
9	5	2
9	4	3
9	5	3
9	5	4
10	1	2
10	4	5

For example, in row 1, (9,2,1) means adipose tissue(2) is included inside(9) background(1).

(2). Neighboring relation of each tissue

Name of array: NeighboringRelation

The position of each element in the array denotes the neighboring relation of any two tissues. For example, NeighboringRelation (3,4) = 1 means that muscle (row: 3) and cortical bone (column: 4) have neighboring relation.

	Background	AdiposeTissue	Muscle	Cortical Bone	Spongy Bone
Background	0	1	0	0	0
AdiposeTissue	1	0	1	1	0
Muscle	0	1	0	1	1
Cortical Bone	0	1	1	0	1
Spongy Bone	0	0	1	1	1

(3). Ranking order of all tissues according to their areas

Name of array: RankingOrderofArea

Tissue 1	Tissue 2	Tissue 3	...	...

The ranking order of areas of tissue is descendent. So the array is:

2	4

(which means the area of adipose tissue(2) is more than cortical bone(4))

2	5

3	4

3	5

(4). Number of connected components of certain tissues

Name of array: NumberofConnectedComponents

Number of connected components	Tissue name

So the array is:

Number of connected components	Tissue name
1	1
1	4
1	5

For example, in row 3, (1, 5) means spongy bone(5) has one connected component.

(5). Tissues which have similar grey level

Name of array: SimilarGreyLevel

Tissue 1	Tissue 2	Tissue 3	...	...

So the array is:

1	4

(which means background(1) and cortical bone(4) have similar grey levels)

2	5

Next, we will show the classification procedure for human thigh step by step.

As introduced in the part: High level: Controls generation, the computer first checks the array "SimilarGreyLevel" in Knowledge base module to determine the number of clusters for segmenting the original image, and then it runs the clustering algorithms to obtain the segmentation.

Figure 3.18 is the original image of human thigh, and Figure 3.19 is the result of segmentation.
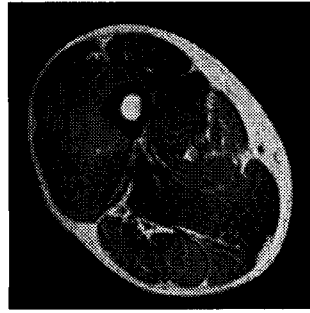
Figure 3.18 Original image of human thigh.

Figure 3.19 Result of segmentation.

Next, we use the optimized strategy for rules application (Figure 3.17) to this example.

Step 1: **Applying Rule 1 for extracting the background.**

Figure 3.20 is the result of identification of background.
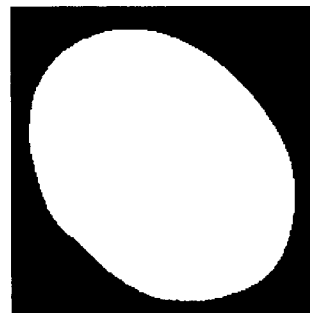
Figure 3.20 Identification of background.

Step 2: **Recursively applying the combination of Rule 3, Rule 4 and Rule 6 for separating new tissues from the obtained classes.**

Rule 3 is first applied. Because there is not any unlabeled tissue whose neighboring tissues have been all labeled, we can not identify tissues by applying this rule.

Next, Rule 4 is applied. Because the adipose tissue and the spongy bone have similar grey levels, and they have not been identified, we can not recognize tissues by applying this rule.

Next, Rule 6 is applied. Because the cortical bone and the background have the similar grey levels and the background has been identified, the cortical bone can be recognized, the result is shown in Figure 3.21.

Figure 3.21 Identification of cortical bone.

Next, Rule 3 is applied. Because the spongy bone has not been labeled, and it has only one neighboring tissue, the cortical bone, which has been identified, the spongy bone can be recognized, the result is shown in Figure 3.22.
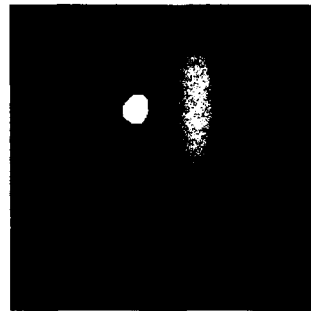
Figure 3.22 Identification of spongy bone.

Next, Rule 4 is applied. Because the cortical bone and the background have similar grey levels and they have been recognized, and because the adipose tissue and the spongy bone have similar grey levels, and the spongy bone has been identified, the premise of this rule is fulfilled. There

are only the muscle and the adipose tissue which have not been recognized, but we do not know the ranking order of their areas, so we can not recognize them by applying this rule.

Next, Rule 6 is applied. Because the adipose tissue and the spongy bone have the similar grey levels and the spongy bone has been identified, the adipose tissue can be recognized, the result is shown in Figure 3.23.

Figure 3.23 Identification of adipose tissue.

There is only one tissue which has not been recognized, the muscle, we can identify it easily, the result is shown in Figure 3.24.

Figure 3.24 Identification of muscle.

Because all the tissues have been identified, the classification system stops.

Having classified all tissues, we assign the following grey levels to these classes in order to generate a synthetic image to show the classification result.: background: 20; adipose tissue: 250; muscle: 60; cortical bone: 200; spongy bone: 150;

Figure 3.25 shows the synthetic image of classification. Figure 3.26 intuitively compares the classification reference and our classification. TABLE 3.5 gives the corresponding quantitative

comparison.

Figure 3.25 Synthetic image of classification.

(a)

(b)

(c)

(d)
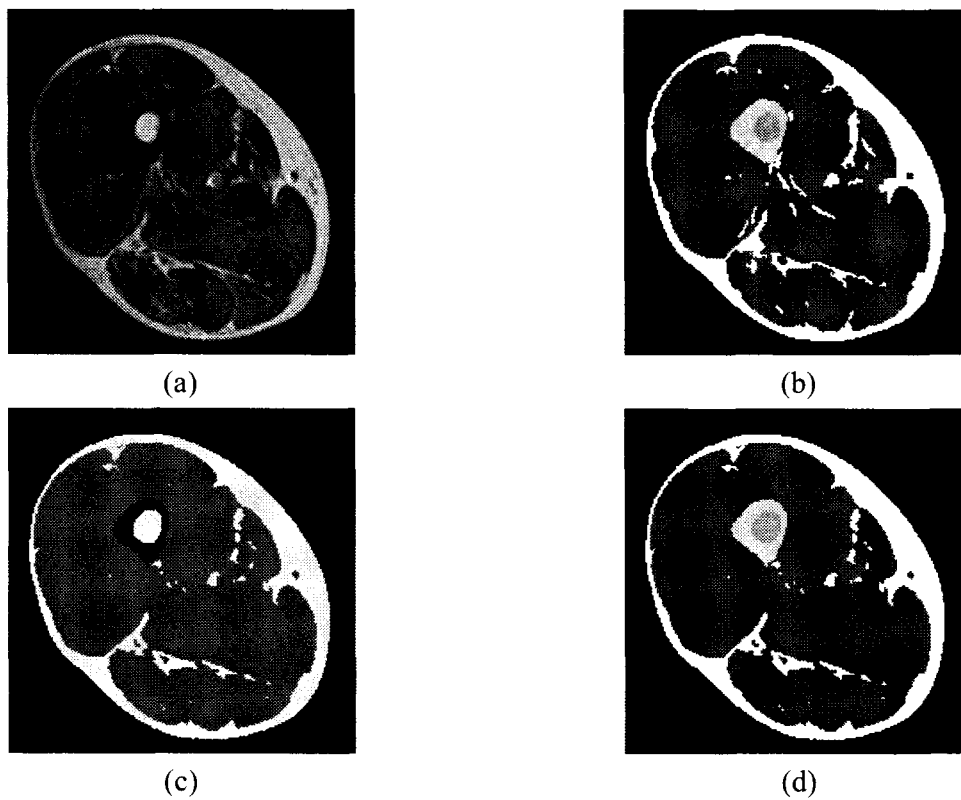
Figure 3.26 Classification for human thigh.

(a). original image. (b). classification reference. (c) segmentation result. (d) synthetic image for the classified results. (different grey levels are assigned to the classes: background: 20; adipose tissue: 250; muscle: 60; cortical bone: 200; spongy bone: 150;)

TABLE 3.5 Quantitative comparison of classification results for one image of thigh.

Adipose tissue	Cortical bone	Spongy bone	Muscle
82.58%	84.87%	83.98%	95.42%

Next, this proposed tissue classification system is validated on human crus, arm, forearm, and brain respectively. Figure 3.27 - 3.30 shows the corresponding results. TABLE 3.6 - TABLE 3.9 gives the corresponding quantitative comparison. We can see that all the classification results are very satisfying.

(a)   (b)

(c)   ·   (d)
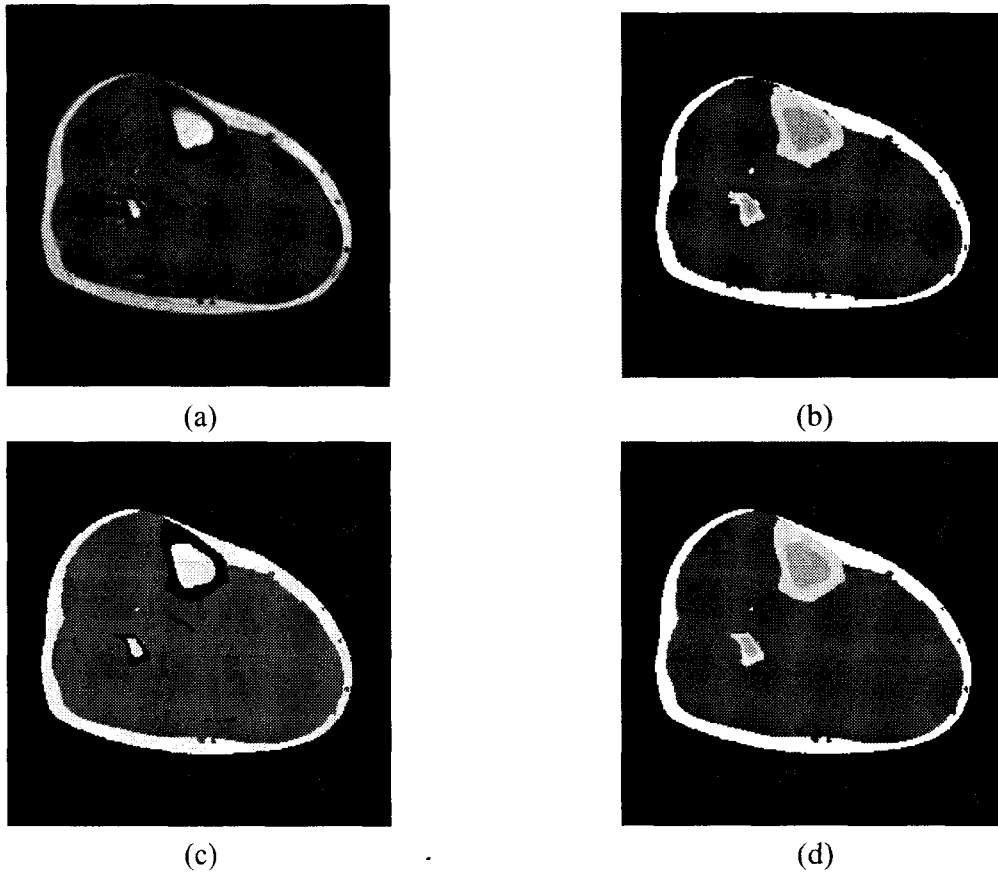
Figure 3.27 Classification for human crus.

(a). original image. (b). classification reference. (c) segmentation result. (d) synthetic image for the classified results. (different grey levels are assigned to the classes: background: 20; adipose tissue: 250; muscle: 60; cortical bone: 200; spongy bone: 150;)

TABLE 3.6 Quantitative comparison of classification results for one image of crus.

Adipose tissue	Cortical bone	Spongy bone	Muscle
93.18%	81.96%	88.07%	98.05%

(a)

(b)

(c)

(d)
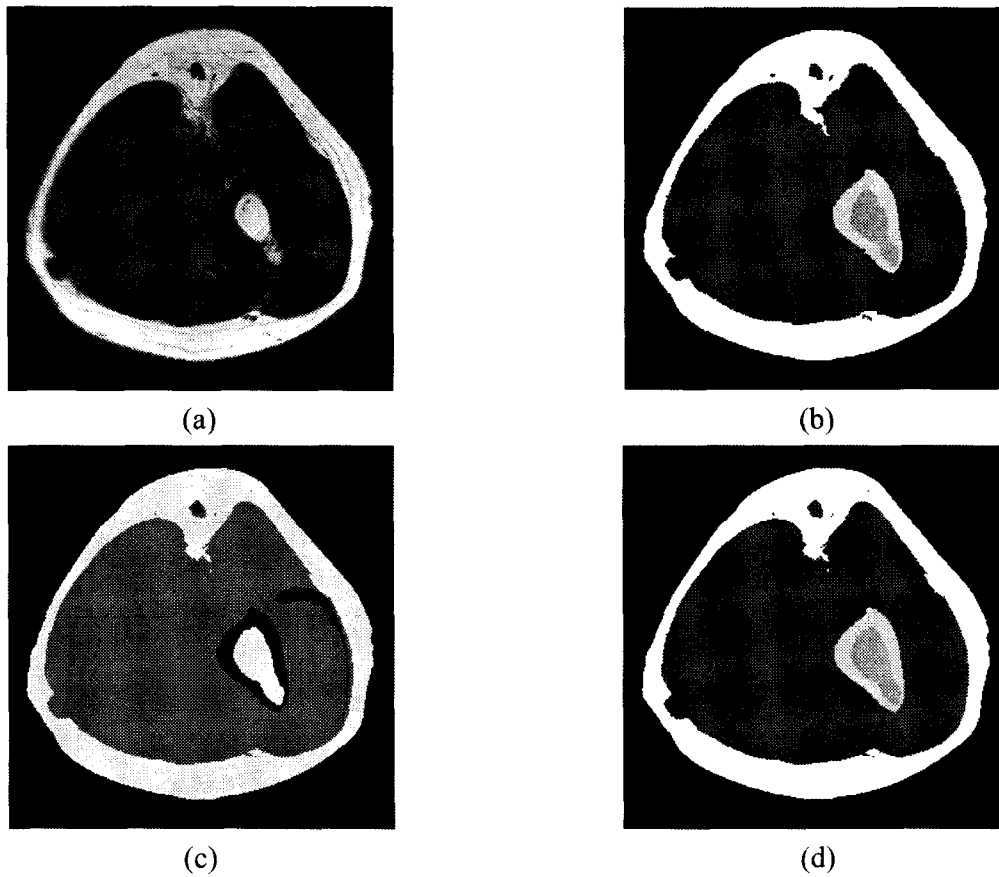
Figure 3.28 Classification for human arm.

(a). original image. (b). classification reference. (c) segmentation result. (d) synthetic image for the classified results. (different grey levels are assigned to the classes: background: 20; adipose tissue: 250; muscle: 60; cortical bone: 200; spongy bone: 150;)

TABLE 3.7 Quantitative comparison of classification results for one image of arm.

Adipose tissue	Cortical bone	Spongy bone	Muscle
96.54%	78.45%	91.2%	98.41%

(a)

(b)

(c)

(d)
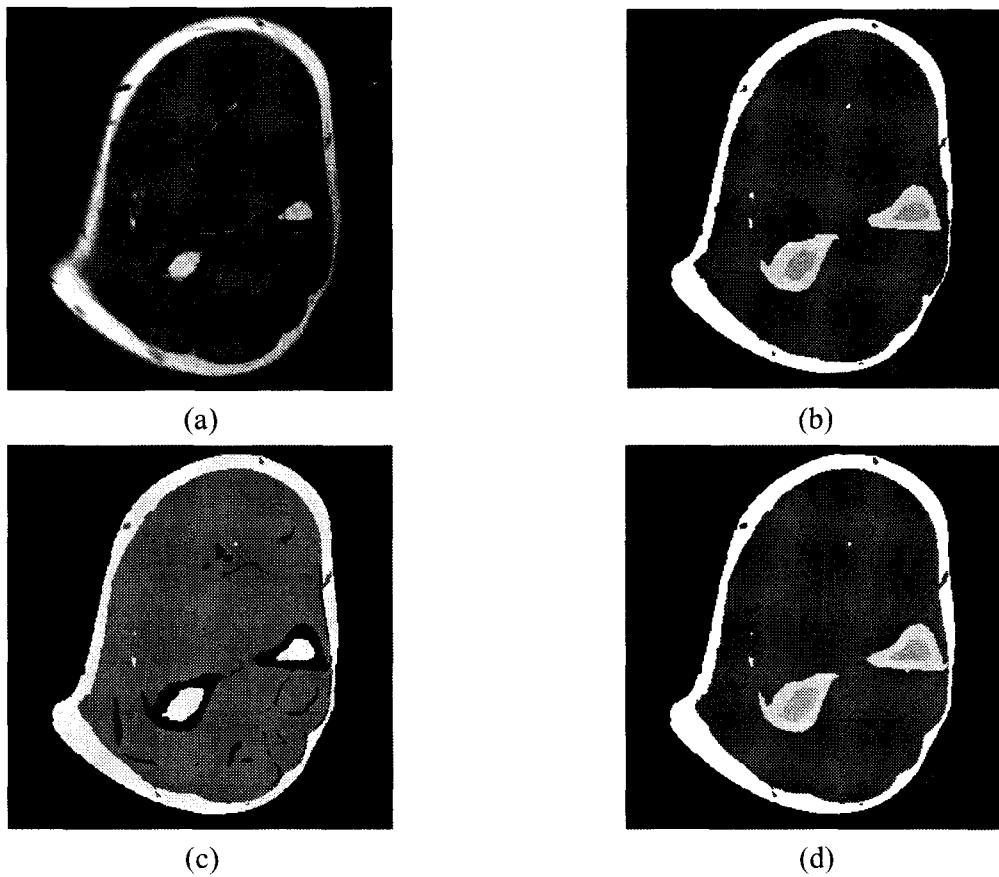
Figure 3.29 Classification for human forearm.

(a). original image. (b). classification reference. (c) segmentation result. (d) synthetic image for the classified results. (different grey levels are assigned to the classes: background: 20; adipose tissue: 250; muscle: 60; cortical bone: 200; spongy bone: 150;)

TABLE 3.8 Quantitative comparison of classification results for one image of forearm.

Adipose tissue	Cortical bone	Spongy bone	Muscle
89.48%	85.5%	83.73%	97.25%

(a)   (b)

(c)   (d)
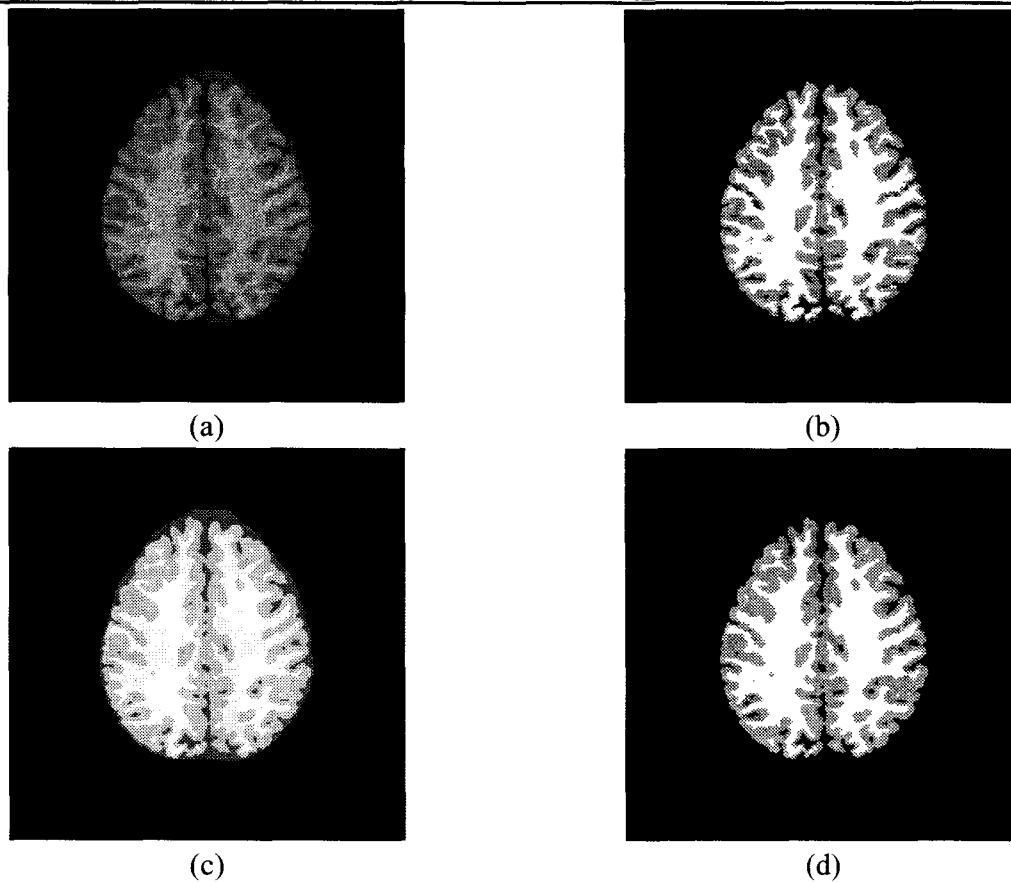
Figure 3.30 Classification for human brain.

(a). original image. (b). classification reference. (c) result of segmentation. (d) synthetic image of classification. (with the grey levels assigned to each class: background: 20; grey material: 250; white material: 150;)

TABLE 3.9 Quantitative comparison of classification results for one image of brain.

Grey material	White material	Background
87%	83%	99%

3.3   Analysis and conclusion

In this chapter, we first present an intelligent specific system for tissue classification of thigh. In this system, a priori knowledge is integrated to guide and control the FCM-based segmentation procedure for tissue classification. The a priori knowledge used in this study concerns the tissue geometric structure, especially the relative positions and the neighboring relations between different tissues in the slice. We construct specific models for these relations. Based on these

models, we propose four steps each permitting to separate a new tissue from the thigh image. Compared to the other existing classification results, our results are satisfying.

The drawback of this specific system is that it depends too much on the specific knowledge of the thigh structure and background knowledge incorporation is a manual procedure. For segmenting images of other organs, we need to integrate new background knowledge and construct new models.

For this purpose, we successfully identify the common tissue features among different parts of human body and then construct the corresponding models for these features. In this way, we construct a more generalized system permitting to formalize all kinds of human knowledge on medical image observation and automatically incorporate them into the image analysis procedure. We validate this system on several different organs such as human thigh, crus, arm, forearm and brain. All the classification results are satisfying.

Figure 3.31 shows the methodology used in this study. From Figure 3.31, we can see the main advantage of our system over the other existing ones, such as the system for brain ([14-16]), the system for bone ([17]), and the system for chest ([18]). As each of these existing systems is constructed for a specific application, and is not normalized and structured, thus lacks of certainty and precision in other applications. However, in the proposed system, we carry out the abstraction to extract the common tissue features from different parts of human body and then construct the generalized models for these features. In this way, our system is not limited to a specific application but suitable for various applications. We validate this generalized system on human thigh, crus, arm, forearm, and brain and we obtain satisfying results.

Moreover, another advantage of our system is that we add a user-friendly interface to facilitate the human machine interaction in order to obtain the a priori knowledge. The interface is a online

questionnaire. This questionnaire can be filled either by invited experts according to their professional knowledge or by operators of the system according to answers found in anatomical text books. Anyway, the knowledge is expressed by linguistic description.

```
┌─────────────────────────┐
│   Specific knowledge    │
└─────────────────────────┘
             │
             ▼
┌─────────────────────────┐
│     Specific model      │
└─────────────────────────┘
             │
             ▼
┌─────────────────────────┐
│      Abstraction        │
└─────────────────────────┘
             │
             ▼
┌─────────────────────────┐
│    Generalized model    │
└─────────────────────────┘
             │
             ▼
┌─────────────────────────┐
│    Different specific   │
│      applications       │
└─────────────────────────┘
```
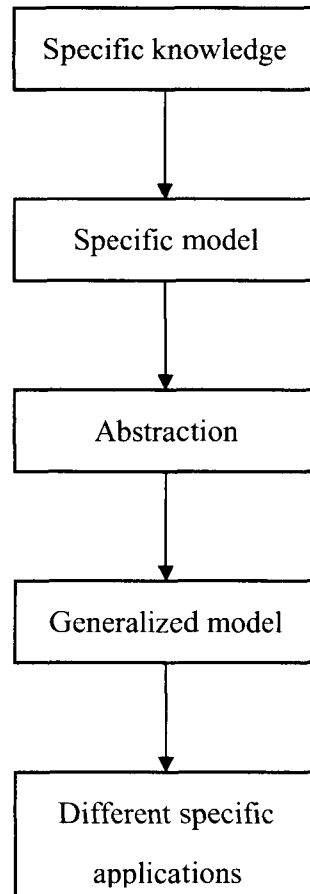
Figure 3.31 Methodology used in this study.

In addition, we propose two principles to define the priorities for these rules in order to optimize their application. The rules with higher priorities will be applied before those with lower priorities.

Conclusion and future work

My PhD work has two main objectives: robust image segmentation and tissue classification by integrating expert's knowledge. The robust image segmentation method we developed shows good and stable performance on both synthetic images and MRI. Although image segmentation has been successfully applied to medical image analysis, it is difficult for the existing grey level-based methods to identify tissues having similar values of features. In practice, key geometric features greatly vary from tissue to tissue and the extraction of common generalized features is then too complex. In this context, we focus on constructing a generalized intelligent system for tissue classification which integrates a priori knowledge on tissues.

The medical image segmentation performed in the first part of my PhD work is based on the Fuzzy C-Means clustering methods (FCM). Related to the classical FCM methods applied to medical image segmentation, some modifications have been carried out to solve the drawbacks existing in these methods. The main improvements include:

(1). We use the standard FCM objective function without adding any penalty term. This can effectively reduce the difficulties related to the determination of the coefficient of the penalty term and complex derivations.

(2). We use a ten-dimensional feature vector to describe each pixel. This vector includes both local and global spatial information on neighboring pixels. An improvement on this vector is made to reduce the algorithm complexity of FCM and more effectively extract the spatial information of objects on the image.

(3). We propose an algorithm to define the window size in a dynamical way for extracting appropriate global spatial information from images. The proposed FCM based method has shown robust and stable performance in the segmentation of both synthetic and MRI images.

Even if medical image segmentation is perfectly done, most of the tissue classification results are

unsatisfactory because of the limitations of grey level-based segmentation methods and the lack of physical interpretation on segmented classes.

In this context, the second part of my PhD work is to develop an intelligent system for tissue classification based on the segmented classes. First, a specific tissue classification system of thigh has been developed. In this system, a priori knowledge concerning the tissue geometric structure of thigh is used to control the application of the FCM algorithm during the segmentation procedure for tissue classification of thigh.

Although the proposed system has shown good performance on classification of thigh, it relies too much on the specific knowledge of the thigh structure. For segmenting images of other organs, we need to construct new models for extracting new knowledge on tissues. Thus, it is necessary to develop a more generalized system permitting to formalize various human knowledge on medical image and automatically incorporate them into the image segmentation procedure.

Next, we developed a more generalized system for tissue classification. An abstraction procedure has been performed to find the common tissue features among different parts of human body and construct the corresponding models for these features. In this way, we construct a more generalized system which is not limited to a specific application but permits to formalize all kinds of human knowledge on medical image observation and automatically incorporate them into the image segmentation procedure. We successfully validate this system on human thigh, crus, arm, forearm and brain. The classification results are very satisfying.

The principle of our developments in the second part of my PhD work is: "specific knowledge" → "specific model" → "abstraction" → "generalized model" → "different specific applications".

Further improvements can be done according to the two following orientations. In the medical

image segmentation step, we wish to integrate new relevant geometric features into the FCM algorithm and replace the Euclidean distance by the kernel-based distance in the standard FCM objective function. In the tissue classification step, we will work on the quantification of the muscle/fat ratio, assessment of the muscle/fat temporal variation, and measurement of the volume of muscle, fat and bone in human legs. We will also validate our system on other parts of human body. Furthermore, we will make more efforts for exploring other common tissue features and add new rules to our system so that our system can be more generalized. We will also endeavor to apply new methods to formalize the tissue geometric feature, such as the Fuzzy Logic. In addition, we will try to propose new principles to define the priorities of rules in order to optimize their applications.

Appendix 1 Introduction to blackboard system

A **blackboard system** ([83,95]) is an artificial intelligence application based on the blackboard architectural model, where a common knowledge base, the "blackboard", is iteratively updated by a diverse group of specialist knowledge sources, starting with a problem specification and ending with a solution. Each knowledge source updates the blackboard with a partial solution when its internal constraints match the blackboard state. In this way, the specialists work together to solve the problem. The blackboard model was originally designed as a way to handle complex, ill-defined problems.

The following scenario provides a simple metaphor that gives some insight into how a blackboard system works.

A group of specialists are seated in a room with a large blackboard. They work as a team to brainstorm a solution to a problem, using the blackboard as the workplace for cooperatively developing the solution. The session begins when the problem specifications are written onto the blackboard. The specialists all watch the blackboard, looking for an opportunity to apply their expertise to the developing solution. When someone writes something on the blackboard that allows another specialist to apply their expertise, the second specialist records their contribution on the blackboard, hopefully enabling other specialists to then apply their expertise. This process of adding contributions to the blackboard continues until the problem has been solved.

A blackboard-system application consists of three major components:

– The software specialist modules, which are called knowledge sources (KSs). Like the human experts at a blackboard, each knowledge source provides specific expertise needed by the application. The ability to support interaction and cooperation among diverse KSs creates

enormous flexibility in designing and maintaining applications. As the pace of technology has intensified, it becomes ever more important to be able to replace software modules as they become outmoded or obsolete.

– The blackboard, a shared repository of problems, partial solutions, suggestions, and contributed information. The blackboard can be thought of as a dynamic "library" of contributions to the current problem that have been recently "published" by other knowledge sources.

– The control shell, which controls the flow of problem-solving activity in the system. Just as the eager human specialists need a moderator to prevent them from trampling in a mad dash to grab the chalk, KSs need a mechanism to organize their use in the most effective and coherent fashion. In a blackboard system, this is provided by the control shell.

Appendix 2 Introduction to MRI distribution

The original signal of MRI is measured through a quadrature detector which gives the real and the imaginary signals. The real and the imaginary signals are reconstructed from the acquired data by the complex Fourier transform. The magnitude images are formed by calculating the magnitude, pixel by pixel, from the real and the imaginary images ([97]). The distribution of the grey levels of pixels is the Rician distribution:

$$\rho_M(M) = \frac{M}{\sigma^2} e^{-(M^2+A^2)/2\sigma^2} I_0(\frac{A \cdot M}{\sigma^2}) \tag{4.1}$$

where:

A is the image pixel intensity in the absence of noise.

M is the measured pixel intensity.

I_0 is the modified zeroth order Bessel function of the first kind.

σ is the stardard deviation of the Gaussian noise in the real and the imaginary images.

When only noise is present, which signifies the air, it is approximately the Rayleigh distribution:

$$\rho_M(M) = \frac{M}{\sigma^2} e^{-M^2/2\sigma^2} \tag{4.2}$$

When the Signal to Noise Ratio (SNR) is large, which signifies the tissues, it is approximately the Gaussian distribution:

$$\rho_M(M) \approx \frac{1}{\sqrt{2\pi\sigma^2}} e^{-(M-\sqrt{A^2+\sigma^2})^2/2\sigma^2} \tag{4.3}$$

Figure 4.1 shows the Rician distribution of MRI signal for different values of SNR, the A/σ. We can see that Rician distribution is far from being Gaussian distribution for small SNR ($A/\sigma \leq 1$). For ratios as small as $A/\sigma = 3$, however, it starts to approximate the Gaussian distribution. Note that the mean of the distributions, $\bar{M}/\sigma$, which is shown by the vertical lines in Figure 4.1, is

not the same as A/σ. This bias is due to the nonlinear transform of the noisy data.
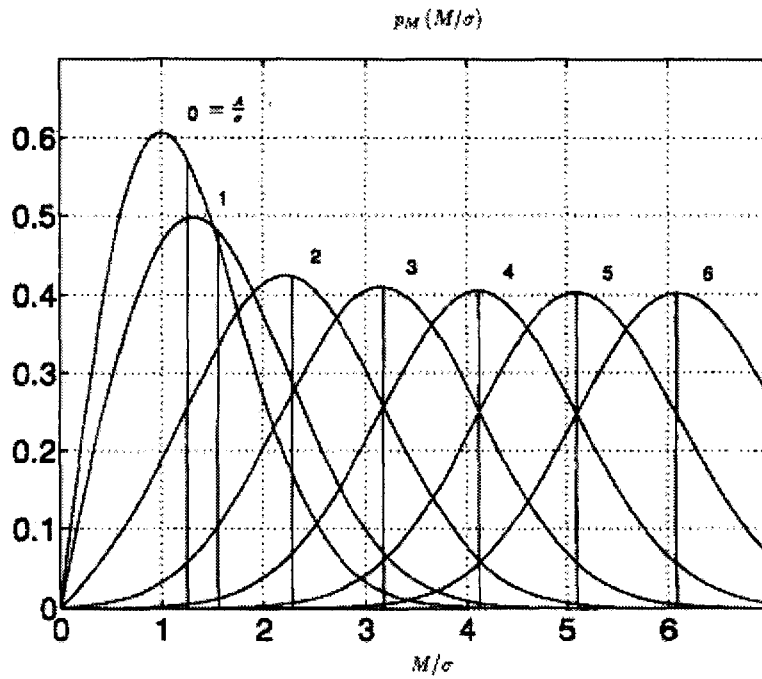
Figure 4.1 The Rician distribution of M, for several Signal to Noise Ratios, A/σ, and the corresponding means.

Appendix 3 A comparison on algorithm complexity among different image segmentation methods

In this part, we give a comparison on the algorithm complexity among different segmentation methods, FCM_S_2, KFCM_S_2, NGFCM, GMM_S_2, MFFCM, and IMFFCM_DS. Because they are with different forms. For example, there is the Euclidean distance in FCM_S_2, NGFCM, MFFCM, and IMFFCM_DS, but there is the kernel-induced distance in KFCM_S_2. Direct comparison of complexity on analytical level is quite difficult. So we do a comparison on computational time for the synthetic image with 5% "Gaussian" noise (see Figure 2.1 (a)) to compare the computational performance of each method. The experiments have been carried out on an ASUS computer with 1.5 GHz Intel Pentium processor and a RAM of 256M. TABLE 4.1 shows this comparison. We can see that IMFFCM_DS is the fastest. In addition, IMFFCM_DS also shows the best segmentation performance (see TABLE 2.1). GMM_S_2 is the slowest because of the slow speed of convergence of Expectation Maximisation method. MFFCM is slower than IMFFCM_DS because MFFCM uses a 5-dimension vector, but IMFFCM_DS uses a 10-dimension vector. KFCM_S_2 is slower than FCM_S_2 because KFCM_S_2 uses kernel-induced distance, but FCM_S_2 uses Euclidean distance.

TABLE 4.1 Computational time (on second) on the synthetic image with 5% "Gaussian" noise.

.IMFFCM_DS	FCM_S_2	KFCM_S_2	MFFCM	NGFCM	GMM_S_2
10 s	12 s	13 s	30 s	45 s	21 * 60 s

Appendix 4 An analysis on confidence interval for our classification results

In this part, we give an analysis of confidence intervals on our classification results to show the stability of these results. The confidence interval ([92]) is defined as follows.

Suppose $Z_1,...,Z_n$ are an independent sample from a normally distributed population with mean μ and variance σ^2. Let:

$$\overline{Z} = \frac{(Z_1 + \cdots + Z_n)}{n} \tag{5.1}$$

$$S^2 = \frac{1}{n-1} \sum_{i=1}^{n} (Z_i - \overline{Z})^2 \tag{5.2}$$

Then

$$T = \frac{\overline{Z} - \mu}{S / \sqrt{n}} \tag{5.3}$$

has a Student's t-distribution ([96]). If d is the 95th percentile of this distribution, then:

$$\Pr(-d < T < d) = 0.9 \tag{5.4}$$

(Note: '95th' and '0.9' are correct in the preceding expressions. There is a 5% chance that T will be less than $-d$ and a 5% chance that it will be larger than $+d$. Thus, the probability that T will be between $-d$ and $+d$ is 90%.)

Consequently:

$$\Pr(\overline{Z} - \frac{dS}{\sqrt{n}} < \mu < \overline{Z} + \frac{dS}{\sqrt{n}}) = 0.9 \tag{5.5}$$

and we have a theoretical 90% confidence interval for μ.

After observing the sample we find values $\bar{z}$ for $\bar{Z}$ and s for S, from which we compute the confidence interval:

$$\left[\bar{z} - \frac{ds}{\sqrt{n}}, \bar{z} + \frac{ds}{\sqrt{n}} \right] \tag{5.6}$$

an interval with fixed numbers as endpoints, of which we can no more say there is a certain probability it contains the parameter μ. Either μ is in this interval or isn't.

Next, we give an analysis on the confidence interval of classification result by IMFFCM_DS for adipose tissue in TABLE 3.1.

We run the algorithm IMFFCM_DS ten times, then we obtain a sample of ten classification results for adipose tissue:

Z= {0.8329, 0.8349, 0.8397, 0.8292, 0.8364, 0.8373, 0.8412, 0.8363, 0.8281, 0.8405}

Consequently we obtain $\bar{z}$ =0.8356, s=0.0045, so the **95%** confidence interval for classification results of adipose tissue is [0.8324, 0.8388]. We can see that this confidence interval is very close to the sample mean, this explains why the results are close in some tables. This also shows that our method is very robust and stable.

Publications of the author

International Journal (1)

K.Han, A.Pinti, A.Taleb-Ahmed, and Z.Xianyi, "Development of a new FCM-based method for medical image segmentation," submitted to *Journal of Mathematical Imaging and Vision* in September, 2008.

International Conference (4)

K.Han, A.Pinti, A.Taleb-Ahmed, Z.Xianyi, "An intelligent generalized system for tissue classification by incorporating qualitative medical knowledge," submitted to *7th IFAC Symposium on Modelling and Control in Biomedical Systems (including Biological Systems)*, August 12-14, 2009, Denmark.

K.Han, Z.Xianyi, A.Taleb-Ahmed, A.Pinti, "Integration of human knowledge for automatic tissue classification on medical images," *International FLINS Conference on Computational Intelligence in Decision and Control*, pp.447-452, September 21-24, 2008, Spain. *(indexed by ISI Proceedings, included in the book "Computational Intelligence in Decision and Control")*

K.Han, A.Pinti, L.Vermeiren, A.Taleb-Ahmed, Z.Xianyi, "Tissue classification for MRI of thigh using a modified FCM method," *International Conference of the IEEE Engineering in Medicine and Biology Society*, pp.5579-5584, August 23-26, 2007, France, ISBN 1-4244-0788-5. *(indexed by Medline/Pubmed)*

K.Han, A.Pinti, L.Vermeiren, A.Taleb-Ahmed, Z.Xianyi, "An automatic FCM-based method for tissue classification," *IEEE International Conference on Bioinformatics and Biomedical Engineering*, pp.520-524, July 6-8, 2007, China, ISBN 1-4244-1120-3. *(indexed by EI)*

A.Pinti, P.Hedoux, K.Han, A.Taleb-Ahmed, "An automated pixel classification method using surface expansion," *IEEE Conference on Computational Engineering in System Application*, pp.1-6, October 4-6, 2006, China, ISBN 7-900718-14-1. *(indexed by EI)*

Bibliography

[1] J.C.Seidell, C.J.C.Bakker, and V.D. K.Kooy, "Imaging techniques for measuring adipose-tissue distribution-a comparison between computed tomography and 1.5-T magnetic resonance," *American Journal of Clinical Nutrition*, Vol.51, pp.953-957, 1990.

[2] G.Z.Yang, S.Myerson, F.Chabat, D.J.Pennell, and D.N.Firmin, "Automatic MRI adipose tissue mapping using overlapping mosaics," *Magnetic Resonance Materials in Physics, Biology and Medicine*, Vol.14, pp.39–44, 2002.

[3] A.Colin, E.Erbland, C.Datin, J.Y.Boire, A.Veyre, and M.Zanca, "Automatic muscle/fat quantification on MR images," in *Proceedings of the IEEE Engineering in Medicine and Biology 17th International Conference*, Montreal, Vol.1, pp.479-480, 1995.

[4] V.Barra and J.V.Boire, "Segmentation of fat and muscle from MR images of the thigh by a possibilistic clustering algorithm," *Computer Methods and Programs in Biomedicine*, Vol.68, pp.185–193, 2002.

[5] A.W.C Liew and H.Yan, "An adaptive spatial fuzzy clustering algorithm for 3-D MR image segmentation," *IEEE Transactions on Medical Imaging*, Vol. 22, N° 9, pp.1063-1075, September 2003.

[6] D.Zhang and S.Chen, "A novel kernelized fuzzy C-means algorithm with application in medical image segmentation," *Artificial Intelligence in Medicine*, Vol.32, pp.37-50, 2004.

[7] A.K.Jain, Y.Zhong and M.P.Jolly, "Deformable template models: A review," *Signal Processing*, Vol. 71, pp. 109–129, 1998.

[8] A.Ghanei, H.Soltanian-Zadeh, and J.P.Windham, "A 3D deformable surface model for segmentation of objects from volumetric data in medical images," *Computers in Biology and Medicine*, Vol.28, pp.239-253, 1998.

[9] P.Marais, and J.M.Brady, "Detecting the brain surface in sparse MRI using boundary models," *Medical Image Analysis*, Vol.4, pp.283–302, 2000.

[10] A. Same, C. Ambroise, and G. Govaert, "A classification EM algorithm for binned data," *Computational Statistics & Data Analysis*, Vol.5, pp.466-480, 2006.

[11] K.V.Leemput, F.Maes, D.Vandermeulen, and P.Suetens, "Automated model-based tissue classification of MR images of the brain," *IEEE Transactions on Medical Imaging*, Vol.18, pp. 897–908, 1999.

[12] A.Tsai, William.M.Wells, S.K.Warfield, and A.S.Willsky, "An EM algorithm for shape classification based on level sets," *Medical Image Analysis*, Vol.9, pp.491–502, 2005.

[13] K.S.Chuang, H.L.Tzeng, S.Chen , J.Wu, and T.J.Chen, "Fuzzy c-means clustering with spatial information for image segmentation," *Computerized Medical Imaging and Graphics*, Vol.30, pp.9–15, 2006.

[14] C.Li, D.B.Goldgof, and L.O.Hall, "Knowledge-based classification and tissue labeling of MR images of human brain," *IEEE Transactions on Medical Imaging*, Vol.12, N° 4, pp.740-750, December 1993.

[15] H.Li, R.Deklerck, B.D.Cuyper, A.Hermanus, E.Nysser, and J.Cornelis, "Object recognition in brain CT-scans: knowledge-based fusion of data from multiple feature extractors," *IEEE Transactions on Medical Imaging*, Vol.14, N° 2, pp.212-229, June 1995.

[16] H.Li, R.Deklerck, and J.Cornelis, "Integration of multiple knowledge sources in a system for brain CT-scan interpretation based on the blackboard model," in *Proceedings of the 10th Conference on Artificial Intelligence for Applications*, San Antonio, TX, USA, pp.336- 343, 1994.

[17] Z.Q.Liu, H.L.Liew, J.G.Clement, and C.D.L.Thomas, "Bone image segmentation," *IEEE Transactions on Biomedical Engineering*, Vol.46, N° 5, pp.565-570, May 1999.

[18] M.S.Brown, M.F.McNitt-Gray, N.J.Mankovich, J.G.Goldin, J.Hiller, L.S.Wilson, and D.R.Aberle, "Method for segmenting chest CT image data using an anatomical model: Preliminary results," *IEEE Transactions on Medical Imaging*, Vol.16, N° 6, pp.828-839, December 1997.

[19] W.K.Pratt, *Digital Image Processing*, John Wiley & Sons, Inc, 2001.

[20] K.R.Castleman, *Digital Image Processing*, Prentice-Hall, Inc, 1996.

[21] D.Y.Kim and J.W.Park, "Connectivity-based local adaptive thresholding carotid artery segmentation using MRA images," *Image and Vision Computing*, Vol.23, pp.1277-1287, 2005.

[22] M. Kass, A. Witkin, and D. Terzopoulos, "Snakes, active contour model," *International Journal of Computer Vision*, N° 4, pp.321-331, 1988.

[23] T. McInerney and D. Terzopoulos, "Deformable models in medical image analysis: A survey," *Medical Image Analysis*, Vol.1, pp. 91-108, 1996.

[24] V. Caselles, F. Catte, T. Coll, and F. Dibos, "A geometric model for active contours," *Numerische Mathematik*, Vol.66, pp.1-31, 1993.

[25] E.Bardinet, L.D.Cohen, and N.Ayache, "Tracking and motion analysis of the left ventricle with deformable superquadrics," *Medical Image Analysis*, Vol.1, N° 2, pp.129-149, 1996.

[26] T.McInerney and D.Terzopoulos, "A dynamic finite element surface model for segmentation and tracking in multidimensional medical image with application to cardiac 4D image analysis," *Computerized Medical Imaging and Graphics*, Vol.19, pp.69-83, 1995.

[27] T.McInerney and D.Terzopoulos, "Topologically adapable snakes," in *Proceedings of Fifth International Conference on Computer Vision*, pp.840-845, Cambridge, MA, June, 1995.

[28] M.B.Cuadra, M.D.Craene, V.Duay, B.Macq, C.Pollo, and J.P.Thiran, and J.A.Noble, "Dense deformation field estimation for atlas-based segmentation of pathological MR brain images," *Computer Methods and Programs in Biomedicine*, Vol.84, pp.66-75, 2006.

[29] A.Pitiot, H.Delingette, P.M.Thompson, and N.Ayache, "Expert knowledge-guided segmentation system for brain MRI," *NeuroImage*, Vol.23, pp.S85–S96, 2004.

[30] J. Montagnat, H. Delingette, and N. Ayache, "A review of deformable surfaces: Topology, geometry and deformation," *Image and Vision Computing*, Vol.19, pp.1023-1040, 2001.

[31] J. Sethian, "Numerical algorithms for propagating interfaces: Hamilton-Jacobi equation and conservation laws," *Journal of Differential Geometry*, Vol.31, pp.131-161, 1990.

[32] J.A.Sethian, Level Set Methods and Fast Marching Methods: Evolving Interfaces in Computational Geometry, Fluid Mechanics, Computer Vision, and Materials Science. Cambridge, UK: Cambridge University Press, 1999.

[33] V. Caselles, R. Kimmel, and G. Sapiro, "Geodesic active contours," in *Proceedings of International Conference on Computer Vision*, pp. 694-699, Cambridge, MA, USA, 1995.

[34] F.Derraz, A.Taleb-Ahmed, A.Chikh, F. Berksi-Reguig, "MR images segmentation based on Coupled geometrical active contour model to anisotropic diffusion filtering," *IEEE International Conference on Bioinformatics and Biomedical Engineering*, pp.721-724, Wuhan, China, 2007.

[35] W.E.Snyder and H.Qi, *Machine Vision*, Cambridge University Press, 2004.

[36] A.R.Webb, *Statistical Pattern Recognition*, Second Edition, John Wiley & Sons, Inc, 2002.

[37] S.Theodoridis and K.Koutroumbas, *Pattern Recognition*, Second Edition, Elsevier Science (USA), 2003.

[38] B.Zhaoqi, and Z.Xuegong, *Pattern Recognition*, Second Edition, Tsinghua University Press, 2000.

[39] A.Dempster, N.Laird, and D.Rubin, "Maximum likelihood from incomplete data via the EM algorithm," *Journal of the Royal Statistical Society*, Vol.39, pp.1-38, 1977.

[40] R.Hogg, J.McKean and A.Craig. *Introduction to Mathematical Statistics*, Pearson Prentice Hall, 2005.

[41] B.Zhang, C.Zhang, andX.Yi, "Competitive EM algorithm for finite mixture models," *Pattern Recognition*, Vol.37, pp.131-144, 2004.

[42] T.M.Mitchell, *Machine Learning*, McGraw-Hill companies, Inc, 1997.

[43] C.Fraley and A.Raftery, "How many clusters? Which clustering method? Answers via model-based cluster analysis," *Technical report* 329, Seattle: Department of Statistics, University of Washington, 1998.

[44] G.McLachlan and D.Peel, "Robust cluster analysis via mixtures of multi-variate t-distributions," *Lecture Notes in Computer Science*, pp.658-667, 1998.

[45] H.H.Bauschke, D.Noll, A.Celler, and J.M.Borwein, "An EM algorithm for dynamic SPECT tomography," *IEEE Transactions on Medical Imaging*, Vol.18, pp.252-261, March 1999.

[46] S.Gupta, L.Kaur, R.C.Chauhan, and S.C.Saxena, "A versatile technique for visual enhancement of medical ultrasound images," *Digital Signla Processing*, Vol.17, pp.542-560, 2007.

[47] P.P.Wyatt and J.A.Noble, "MAP MRF joint segmentation and registration of medical images," Medical Imaging Analysis, Vol.7, pp.539-552, 2003.

[48] W.Cheng, "Gaussian Mixture Model with Spatial Constrains for Noisy Image Segmentation," Submitted to *JISE*, 2007.

[49] S.Chen and D.Zhang, "Robust image segmentation using FCM with spatial constraints based on new kernel-induced distance measure," *IEEE Transactions on System, Man, and*

Cybernetics-Part B: Cybernetics, Vol.34, N° 4, pp.1907-1916, August 2004.

[50] M.N.Ahmed, S.M.Yamany, N.Mohamed, A.A.Farag, and T.Moriarty, "A modified fuzzy c-means algorithm for bias field estimation and segmentation of MRI data," *IEEE Transactions on Medical Imaging*, Vol.21, N° 3, pp.193-200, March 2002.

[51] D.L.Pham and J.L.Prince, "An adaptive fuzzy C-means algorithm for image segmentation in the presence of intensity inhomogeneity," *Pattern Recognition Letters*, Vol.20, pp.57-68, 1999.

[52] Y.A.Tolias and S.M.Panas, "Image segmentation by a fuzzy clustering algorithm using adaptive spatially constrained membership functions," *IEEE Transactions on System, Man, and Cybernetics*, Vol.28, pp.359-369, May 1998.

[53] Y.A.Tolias and S.M.Panas, "On applying spatial constraints in fuzzy image clustering using a fuzzy rule-based system," *IEEE Signal Processing Letter*, Vol.5, pp.245-247, October 1998.

[54] D.L.Pham and J.L.Prince, "Adaptive fuzzy segmentation of magnetic resonance images," *IEEE Transactions on Medical Imaging*, Vol.18, N° 9, pp.737-752, September 1999.

[55] D.L.Pham, "Spatial models for fuzzy clustering," *Computer Vision and Image Understanding*, Vol.84, pp.285-297, 2001.

[56] X.Li, T.Zhang, and Z.Qu, "Image segmentation using fuzzy clustering with spatial constraints based on markov random field via bayesian theory," special section on *Signal Processing for Audio and Visual Systems and its Implementations, IEICE Transactions Fundamentals*, Vol.E91-A, N° 3, pp.723-728, march, 2008.

[57] J.Bezdek, "A convergence theorem for the fuzzy data clustering algorithms," *IEEE Transactions Pattern Analysis and Machine Intelligence*, Vol.2, pp.1–8, 1980.

[58] R.O.Duda, P.E.Hart, and D.G.Stork, *Pattern Classification*, John Wiley & Sons, Inc, 2001.

[59] T.J.Ross, *Fuzzy Logic with Engineering Applications*, McGraw-Hill companies, Inc, 1995.

[60] K.R.Muller, S.Mika, G.Ratsch, K.Tsuda, and B.Scholkopf, "An introduction to kernel-based learning algorithms," *IEEE Transactions on Neural Networks*, Vol.12, N° 2, pp.181–201, March 2001.

[61] B.Scholkopf, A.J.Smola, and K.R.Muller, "Nonlinear component analysis as a kernel eigenvalue problem," *Neural Computation*, Vol.10, pp.1299–1319, 1998.

[62] J.H.Chen and C.S.Chen, "Fuzzy kernel perception," *IEEE Transactions on Neural Networks*, Vol.13, pp.1364–1373, November 2002.

[63] M.Girolami, "Mercer kernel-based clustering in feature space," *IEEE Transactions on Neural Networks*, Vol.13, pp.780–784, May 2002.

[64] V.N.Vapnik, *Statistical Learning Theory*, New York: Wiley, 1998.

[65] S.Z.Li, *Markov Random Field Modeling in Image Analysis*, Springer-Verlag, New York, 2001.

[66] S.German and D.Geman, "Stochastic relaxation, Gibbs distributions, and the Bayesian restoration of images," *IEEE Transaction Pattern Analysis and Machine Intelligence*, Vol.6, pp.721-741, June, 1984.

[67] Y.Q.Feng and W.F.Chen, "Brain MR image segmentation using fuzzy clustering with spatial constraints based on Markov random field theory," *Lecture Notes Computer Science*, Vol.3150, pp.188-195, 2004.

[68] S.Y.Liu, X.F.Li and Z.M.Li, "A new image segmentation algorithm based the fusion of Markov random field and fuzzy c-means clustering," in *Proceedings of IEEE International Symposium on Communications and Information Technology*, pp.144-147, 2005.

[69] K.Blekas, A.Likas,N.Galatsanos, and I.Lagaris, "A spatially constrained mixture model for image segmentation," *IEEE Transactions on Neural Networks*, Vol.16, N° 2, pp.494–498, March 2005.

[70] A.L.W.Bokde, S.J.Teipel, R.Schwarz, G.Leinsinger, K.Buerger, T.Moeller, H.J.Moller, H.Hampel, "Reliable manual segmentation of the frontal, parietal, temporal, and occipital lobes on magnetic resonance images of healthy subjects," *Brain Research Protocols*, Vol.14, pp.135–145, 2005.

[71] E.Jolivet, W.Skalli, and J.D.Laredo, "Biomechanical modeling of hip and its soft tissue," *Computer Methods in Biomechanics and Biomedical Engineering*, Vol.11, N° S1, pp.125-126, 2008.

[72] A.P.Zijdenbos, B.M.Dawant, R.A.Margolin, "Measurement reliability and reproducibility in manual and semi-automatic MRI segmentation," in *Proceedings of the 15th IEEE-Engineering in Medicine and Biology Society*, pp.162-163, 1993.

[73] S.Dellepiane, G.Venturi, G.Vernazza, "A fuzzy model for the processing and recognition of

MR pathologic images," in *Proceedings of the 12th International Conference on Information Processing in Medical Imaging*, pp.444-457, 1991.

[74] M.W.Vannier, T.K.Pilgram, C.M.Speidel, L.R.Neumann, D.L.Rickman, L.D.Schertz, "Validation of magnetic resonance imaging (MRI) multispectral tissue classification," *Computerized Medical Imaging and Graphics*, Vol.15, pp.217-223, 1991.

[75] R.L.Cannon, J.V.Dave, and J.C.Bezdek, "Efficient implementation of the fuzzy c-means clustering algorithms," *IEEE Transactions Pattern Analysis and Machine Intelligence*, Vol.8, N° 2, pp.248–255, 1986.

[76] L.O.Hall and A.M.Bensaid et al., "A comparison of neural network and fuzzy clustering techniques in segmenting magnetic resonance images of the brain," *IEEE Transactions on Neural Networks*, Vol.3, N° 5, pp.672–682, 1992.

[77] H.N.Schnitzlein and F.R.Murtagh, Imaging Anatomy of the Head and Spine: A Photographic Color Atlas of MRI, CT, gross, and Microscopic Anatomy in Axial, Coronal, and Sagittal Planes. *Baltimore: Urban & Schwarzenberg*, 2nd Edtion, 1990.

[78] E.Kerley, "The microscopic determination of age in human bone," *American Journal of Physical Anthropology*, Vol.23, pp.149–163, 1965.

[79] D.Thompson, "The core technique in the determination of age at death in skeletons," *Journal Forensic Science*, pp.902-914, 1979.

[780] Z.Q.Liu, T.Austin, C.D.L.Thomas, and J.G.Clement, "Bone features analysis using image processing techniques," *Computers in Biology and Medicine*, Vol.26, N° 1, pp.65-76, January 1996.

[81] M.Minsky, "A framework for representing knowledge," *The Psychology of Computer Vision*, P.H.Winston, Ed. New York: McGraw-Hill, 1975.

[82] L.A.Zadeh, "Fuzzy sets," *Information and Control*, Vol.8, N° 3, pp.338-353, 1965.

[83] H.P.Nii, "Blackboard systems: The blackboard model of problem solving and the evolution of blackboard architectures," *AI magazine*, Vol.7, N° 2, pp.38-53, 1986.

[84] J.M.S. Prewitt, "Object Enhancement and Extraction," in *Picture Processing and Psychopictorics*, B.S. Lipkin and A.Rosenfeld, Eds., Academic Press, New York, 1970.

[85] Mathworks, Natick, MA. Image Processing Toolbox. [Online] Available:

http://www.mathworks.com.

[86] J.Weir, P.H.Abrahams, *Imaging Atlas of Human Anatomy*, Times Mirror International Publishers Limited, 1997.

[87] P.Hédoux, "Détermination de paramèters biomécaniques personnalisés à partir d'imagerie médicale, application aux sujets hémiplégique," Ph.D Dissertation, Université de Valenciennes et du Hainaut—Cambrésis, France, 2004.

[88] F.Rambaud, A.Pinti and P.Hédoux, "Correlations between morphological change of the lower limbs and functional recovery of hemiplegic patients," *ITBM-RBM*, Vol.28, issue 1, pp.13-19, 2007.

[89] P.Hédoux and A.Pinti, "Measurement and analysis of volume evolution of soft tissues on the longor of the shank and the thigh in hemiplegic subjects with MRI," *Journal AMSE*, Vol.67, pp.116-126, 2006.

[90] R.J.Maughan, J.S.Watson and J.Weir, "Strength and cross-sectional area of human skeletal muscle," *Journal of Physiology*, Vol.338, pp.37-49, 1983.

[91] C.K.Cheng, H.H.Chen, C.S.Chen, C.L.Lee, and C.Y.Chen, "Segment properties of Chinese adults determined from magnetic resonance imaging," *Clinical Biomechanics*, Vol.15, pp.559-566, 2000.

[92] J.M.Bernardo, and S.Adrian, *Bayesian Theory*, New York: Wiley, 2000.

[93] T.S.Douglas, S.E.Solomonidis, V.S.P.Lee, W.D.Spence, W.A.Sandham, and D.M.Hadley, "Automatic segmentation of magnetic resonance images of the trans-femoral residual limb," *Medical Engineering & Physics*, Vol.20, pp.756-^63, 1998.

[94] G.P.Robinson, A.C.F.Colchester, and L.D.Gr:ifin, "Model-Based Recognition of Anatomical Objects from Medical Images," *Image and Vision Computing*, Vol.12, N° 8, pp.499-507, 1994.

[95] B.Hayes-Roth, "A blackboard architecture for control," *Artificial Intelligence*, Vol.26, pp.251-321, 1985.

[96] A.Gelman, J.B.Carlin, H.S.Stern, and D.B.Rubin, *Bayesian Data Analysis*, 2nd Edition, CRC/Chapman & Hall.

[97] H.Gudbjartsson and S.Patz, "The Rician distribution of noisy MRI data," *Magnetic Resonance in Medicine*, Vol.34, N° 6, pp.910-914, 1995.

Title : Contribution To Automatic Corporal Tissue Classification By Integrating Qualitative Medical Knowledge: Application To The Analysis Of Musculo Skeletal Diseases And Disabilities From MRI Sequences

Abstract : In the diagnosis using MRI images, image segmentation techniques play a key role. Nevertheless, segmentation with context independent features such as grey level and texture often leads to unsatisfactory results because these general features can not take into account the specialized background knowledge. Therefore, it is necessary to incorporate our a priori knowledge on medical image analysis for obtaining better results of tissue classification.

In this context, two main contributions have been proposed in order to improve FCM-based image segmentation quality. The first contribution is that we developed a new FCM-based algorithm for image segmentation. The second contribution is the development of an intelligent system for tissue classification. It consists of two steps. The first step is a specific tissue classification system of thigh. The second step is a generalized intelligent system for tissue classification.

Keywords : Fuzzy C-Means, Expectation Maximisation, MRI, Expert Knowledge, Tissue classification, Image segmentation.

Titre : Contribution à la classification automatique de tissus corporels par intégration des connaissances médicales qualitatives – Applications aux maladies et déficiences musculo squelettiques

Résumé : Dans le diagnostic médical utilisant des images IRM, les techniques de segmentation d'images jouent un rôle important. La segmentation avec les niveaux de gris et la texture conduit souvent à des résultats peu satisfaisants, parce que ces caractéristiques générales ne peuvent pas prendre en compte les connaissances spécialisées. Par conséquent, il est nécessaire d'intégrer des connaissances a priori sur l'analyse des images médicales pour obtenir de meilleurs résultats de la classification des tissus.

Dans ce contexte, deux principales contributions ont été proposées en vue d'améliorer la qualité de la segmentation par la méthode FCM. La première contribution est le développement d'un nouvel algorithme de FCM pour la segmentation d'images. La seconde contribution est le développement d'un système intelligent pour la classification des tissus. Il se compose de deux étapes. La première étape est un système de classification des tissus de la cuisse. La seconde étape est un système intelligent généralisé pour la classification des tissus d'autres zones corporelles.

Mots clés : C-Moyennes Floues, Espérance-Maximisation, IRM, Connaissance d'Expert, Classification de tissus, Segmentation d'images.